



THE UNIVERSITY
of ADELAIDE

Distribution and mineralogical association of Au at the Kanmantoo Cu-Au deposit

Thesis submitted in accordance with the requirements of the University of Adelaide for
an Honours Degree in Geology

Maddison Booth

October 2018

HILLGROVE
RESOURCES



TITLE

Distribution and mineralogical association of Au at the Kanmantoo Cu-Au deposit

RUNNING TITLE

Au at The Kanmantoo Cu-Au Deposit

ABSTRACT

South Australia's Kanmantoo Cu-Au deposit is currently operated by Hillgrove resources and has an extended history of exploration and production dating back to 1846. However, there is little consensus on the paragenesis and structural controls of the deposit.

Empirical work specifically on Au mineralogy and paragenesis has been completed.

To investigate the mineralogical and geochemical associations between Au and host mineralogy, drill core samples, grab samples and ore concentrates and tailings have been collected from the East Kavanagh, Central Kavanagh, West Kavanagh, Spitfire and Nugent ore lodes.

Petrographic analysis, *Mineral Insights Goldsniffer* analysis, secondary electron microscopy-mineral liberation analysis (SEM-MLA) and Laser Ablation (LA-ICP-MS) analysis observed and recorded evidence for four textural settings of Au. Two stages of Au development are proposed: early Au (associated with the main economic Cu-bearing hydrothermal fluids) and late Au (associated with retrograde Bi-rich hydrothermal fluids).

Variations observed in major and trace element composition reflect changing input from a thermally-anomalous hydrothermal fluid source. The stability field for Au nanoparticles and the RARITY of precipitated visible Au supports a late-peak to post-peak metamorphic origin.

This study has implications how Au can be recovered within the Kanmantoo Cu-Au deposit. The mineralogy and geochemical characteristics of Au at the Kanmantoo Cu-Au deposit can also be utilised as an exploration pathfinder within the greater Adelaide fold belt and the Delamarian affected terrains at other exploration provinces within the Adelaide fold belt.

KEYWORDS

Kanmantoo, Delamarian Orogeny, copper-gold, chalcopyrite, bismuth, free gold, invisible gold, nanoparticle gold, trace elements

Word count

7044

Table of Contents

TITLE.....	2
RUNNING TITLE	2
ABSTRACT.....	2
KEYWORDS	3
TABLE OF FIGURES	5
TABLE OF TABLES.....	5
INTRODUCTION.....	6
GEOLOGICAL SETTING	7
2.1 Regional geology.....	7
2.2 The Kanmantoo group.....	8
2.3 Kanmantoo Cu-Au deposit history.....	9
2.4 Host lithologies and mineralisation.....	10
2.5 Structural controls	11
2.6 Paragenetic models.....	12
2.7 Gold endowment	15
METHODS	16
3.1 Field work and sample collection.....	16
3.2 Petrography	16
3.3 <i>Mineral Insights Gold Sniffer</i>	17
3.4 SEM-MLA	17
3.5 LA-ICP-MS.....	18
OBSERVATIONS & RESULTS	19
4.1 Petrography	19
4.2 Mineral Insights Gold Sniffer.....	20
4.4 SEM and LA-ICP-MS investigations of visible Au.....	22
4.5 LA-ICP-MS investigation of ‘invisible’ Au.....	26
4.6 Zonation of Sulphides and other trace elements	33
4.7 Summary of Results	37
DISCUSSION	37
5.1 Review of Methodologies	37
5.2 Cu: Au and other Au associations	38
5.3 Sulphide-hosted Au	39
5.4 Bi-associated Au.....	40
5.5. ‘Invisible’ Au	41
5.6 Au paragenesis within the Kanmantoo Cu-Au deposit	42
5.7 Sources of Au mineralisation	43
5.8 Timing of mineralisation	44
CONCLUSIONS.....	45
FUTURE WORK.....	46
REFERENCES.....	47
APPENDIX.....	550

TABLE OF FIGURES

Figure 1: geological map and stratigraphic nomenclature of the Kanmantoo region

Figure 2: Cross section of Kavanagh ore lode mineralisation

Figure 3: Kanmantoo Cu-Au deposit with wt. % Cu and sample locations.

Figure 4: Sulphide textures observed within sample suite

Figure 5: sulphides and host rock imagery, using an Olympus BX51 optical microscope.

Figure 6: process of validating Gold sniffer results using the *Philips XL30 FESEM*.

Figure 7: SEM images of Sulphide hosted Au.

Figure 8: SEM image of ‘free’ Au grain

Figure 9: SEM images taken in BSE mode showing distribution of Bi

Figure 10: Bi LA-ICP-MS data showing variations in Cu, Au and Ag Ppm

Figure 11: Bi LA-ICP-MS data

Figure 12: LA-ICP-MS spot data displaying nanoparticle Au

Figure 13: Chalcopyrite, pyrrhotite and magnetite LA-ICP-MS data

Figure 14: Chalcopyrite LA-ICP-MS data for Cu, Au, Ag and Bi

Figure 15: LA-ICP-MS raster map for known Au grain location and surrounds

Figure 16: LA-ICP-MS assay data showing zonation within mineral grains.

TABLE OF TABLES

Table 1: LA-ICP-MS spots for analysed minerals containing Au

Table 2: LA-ICP-MS Au spot counts for chalcopyrite, with average ppm Au

INTRODUCTION

South Australia's Kanmantoo mine has a history of production and exploration dating back to 1846. However, despite this extended history, there is little consensus on the paragenesis and structural controls of the Kanmantoo Cu-Au deposit – particularly the timing of mineralisation relative to metamorphism.

Authors including Seccombe et al. (1985) and Pollock et al. (2018) suggest the Kanmantoo Cu-Au deposit is a meta-exhalative system formed by a syn-genetic sub-floor feeder system. Others, such as Oliver et al (1998), argue the deposit is epigenetic and formed during a period of complex tectonic and intrusive activity during the Delamarian Orogeny. The absence of a definitive geological model for mineralisation demonstrates that there are still deficiencies in our understanding of the Kanmantoo Cu-Au deposit.

The Kanmantoo Cu-Au deposit is described as 'weakly anomalous in Au' with a Cu:Au ratio of 100:1 (Rolley and Wright, 2017). There has been no empirical work looking specifically at Au mineralogy and paragenesis within the Kanmantoo Cu-Au deposit.

In order to better understand the relationship and pattern of Au with host minerals, this study responds to the following questions:

- What is the mineralogical association and distribution of Au at Kanmantoo Cu-Au deposit?
- How and why does this distribution vary between ore lodes?
- Is the Au paragenesis at Kanmantoo Cu-Au deposit a local phenomenon, and can the geochemical characteristics of Au at the Kanmantoo Cu-Au deposit can also be utilised as an exploration pathfinder within the greater Adelaide fold belt?

Drill core samples, grab samples and ore concentrate and tailing samples were collected from the East Kavanagh, Central Kavanagh, West Kavanagh, Spitfire and Nugent ore lodes. Optical methods including petrographic analysis, *Gold Sniffer* analysis and secondary electron microscopy-mineral liberation analysis (SEM-MLA) were used to observe Au grains. Laser Ablation (LA-ICP-MS) mineral analysis was also completed to establish if any geochemical relationships exist between Au-bearing minerals and country rock. Beyond assisting with Au recovery in the Kanmantoo Cu-Au deposit, the findings of this study may provide pathfinders for Au in the wider Adelaide hills region.

GEOLOGICAL SETTING

2.1 Regional geology

The Adelaide rift complex, known historically as the Adelaide Geosyncline, is a sedimentary basin province comprised of thick sediments deposited throughout the Neoproterozoic to the Mid-Cambrian on the Eastern Australian margin (Preiss, 2000). Its deposition was followed by a period of convergent deformation, uplift, and major metamorphism known as the Delamarian Orogeny (Foden et al., 2006). This event was triggered and maintained by competing subduction and collisional forces resulting in changing plate dynamics and heterogeneous stress transfer along the Eastern Gondwana margin (Flottman et al., 1994, Foden et al., 2002, Foden et al., 2006). The Delamarian is associated with low-pressure high-temperature metamorphism; ranging from greenschist (~350-400°C) to upper amphibolite facies (~650-700°C) (Foden et al., 2002, Pollock et al., 2018).

Foden et al. (2006) infer the onset of basin inversion and Delamarian contraction took place at 514 ± 4 Ma. This event persisted for a maximum of 24 ± 5 Ma, ceasing contraction at 499 ± 12 Ma. The Delamarian terminated abruptly at the end of the Cambrian period ($\sim 490 \pm 3$

Ma). The end of the Delamarian represents a geochemical shift from syn-tectonic forces to post-tectonic mantle-derived magmatism, and the generation and intrusion of A-type granites.

2.2 The Kanmantoo group

The youngest group within the Adelaide rift complex, the Kanmantoo group is a 7-8 km thick series of locally metamorphosed sedimentary rocks, with a maximum age of 522 ± 2 Ma (Jago et al., 2003). During the early Cambrian, a phase of renewed rifting and extension coinciding with movements along the Gawler craton formed the east to north-east-trending Kanmantoo trough, and thick clastic sediments filled the basin.

The Kanmantoo group is considered to represent a shift in depositional history within the Adelaide fold belt from a passive to active setting (Belperio et al., 1998, Flottman et al., 1994, Flottman et al., 1998, Foden et al., 2002, Gum, 1998, Haines et al., 2001, Jago et al., 2003, Parker, 1986, Preiss, 2000). The rocks seen within the Kanmantoo trough are the result of a build-up and subsequent failure of unstable slope deposits on a major delta complex (Foden et al., 2002, Foden et al., 2006, Jago et al., 2003, Preiss, 2000). There is some debate over the suggested turbidite sequence source— but as Haines et al. (2001) discuss, it is rare to observe a ‘classical’ turbidite in the field, and key indicators for turbidity currents are observed within the Kanmantoo group.

The Tapanappa formation within the Bollaparudda subgroup of the Kanmantoo group (Figure 1) contains several small-to-medium Cu-Pb-Zn (Ag, Au) base metal mineral deposits, focused in a single stratigraphic horizon. The Kanmantoo Cu-Au deposit is hosted within the Paringa Andalusite member, a quartz and Fe-rich metapelite (Rolley and Wright, 2017).

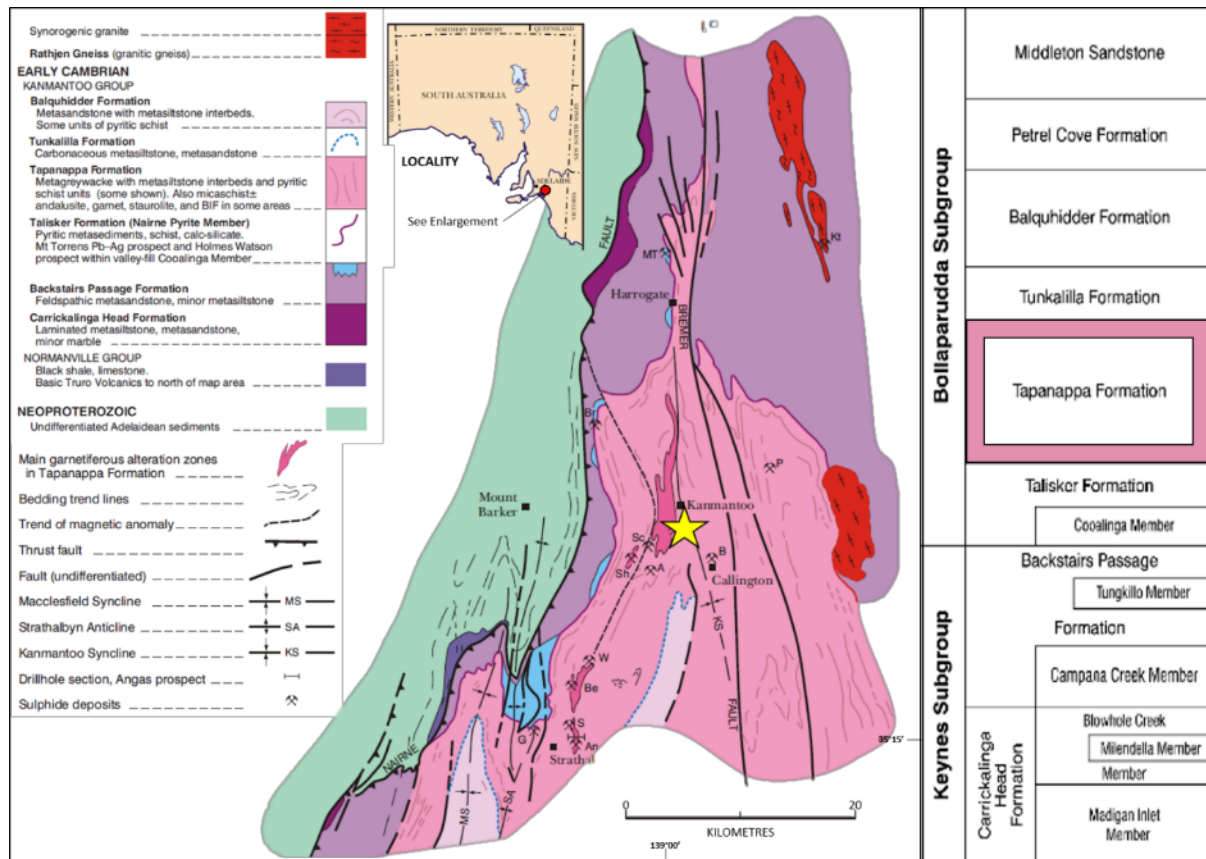


Figure 1: (Left) Geological map of the Kanmantoo region, highlighting the location of the Kanmantoo Cu-Au deposit (after Toteff, 1999). (Right) Stratigraphic nomenclature of the Kanmantoo group (after Jago et al., 2003).

2.3 Kanmantoo Cu-Au deposit history

Located 55 km from Adelaide, South Australia, the Kanmantoo Cu-Au deposit began operations as an underground mine from 1846 to 1874. The current main ore lode was discovered beneath a ferricrete cap in 1962 (Both, 2008, Schiller, 2000). From 1970, Kanmantoo Mines Limited (KML) worked the deposit as an open-cut operation, mining 4,050,000 tons of ore over six years at an average grade of 0.9% Cu, 0.07 g/t Au and 1.8 g/t Ag (Belperio et al., 1998). The operation was closed in 1976 following significant reduction in Cu prices. In April 2004, the mining lease was acquired by Hillgrove Resources, and open-pit production has run from November 2011 to the present day.

2.4 Host lithologies and mineralisation

There are 4 key units spatially associated with the Kanmantoo Cu-Au deposit:

- Garnet andalusite biotite schist (GABS)
- Garnet andalusite biotite staurolite schist (GABSS)
- Quartz mica schist (QMS)
- Biotite garnet chlorite schist (BGCS)

GABS, the dominant host lithology, appears in north-south orientated lenses, containing quartz with lesser staurolite, muscovite, chlorite, magnetite, ilmenite and sulphides. This metamorphosed and hydrothermally-altered unit has a net gain of Fe, Mg and Si, and a net loss of K, Ca and Na due to alteration processes. Fe enrichment and Ca and Na reduction occur closer to mineralisation (Oliver, 1998, Schiller, 2000). Schiller (2000) recognises variation within this GABS unit across the deposit, showing notable differences in schistosity, composition and spatial associations. A common variety of the host GABS rock is the Si-depleted GABSS, with a weak foliation defined by biotite and muscovite.

QMS contains fine grained quartz, biotite, muscovite and feldspars, with minor magnetite, garnet, chlorite, ilmenite and sulphides. Observed relic bedding is thought to represent a pelitic and psammitic source rock.

Enveloped by the GABS and GABSS units, BGCS is the host of most sulphide mineralisation within the Kanmantoo Cu-Au deposit. Cu mineralisation occurs mainly as chalcopyrite, in anastomosing veins intergrown with pyrrhotite (Schiller, 2000). Pyrite and magnetite are observed, with minor ilmenite, cubanite, covellite, pentlandite, cobaltite, molybdenite, sphalerite, wolframite, bismuthinite, native Bi, native Au and native Ag also observed within veins or as disseminated grains (Arbon, 2011, Pollock et al., 2018, Schiller, 2000).

Occurring mainly within BGCS, Cu mineralisation has been recorded as pipelike podiform lenses and stockwork veining usually discordant to bedding. Schiller (2000) observes that the highest-grade ore lodes contain relatively coarse-grained sulphide minerals, and are chlorite-rich with little to no andalusite. Increasing levels of metamorphism envelope the deposit (Oliver et al., 1998), which is a significant observation, as increasing metamorphism is known to promote the movement of ‘invisible Au’ to ‘visible Au’ through recrystallization of early Au-bearing minerals (Chang et al., 2008).

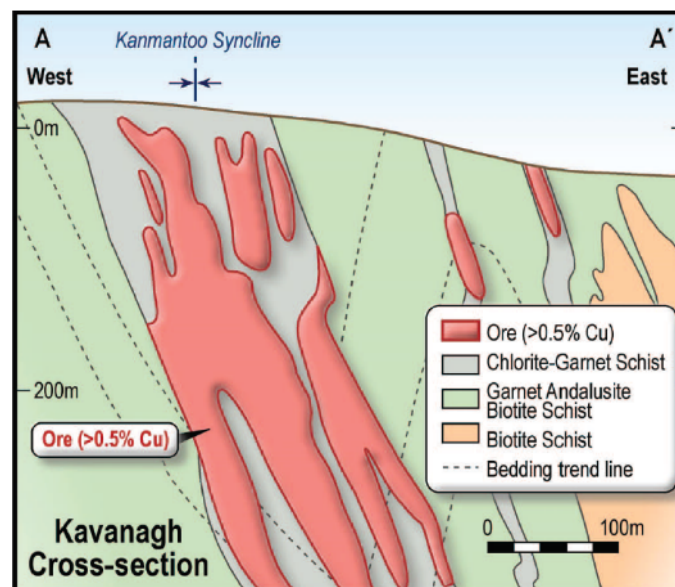


Figure 2: Cross section of Kavanagh mineralisation, highlighting anastomosing ore vein structure and relation to Kanmantoo syncline (after Rolley and Wright, 2017).

2.5 Structural controls

There is a widely-recognised three-stage tectonic evolution for the area, split into D1, D2 and D3 (Pollock, 2018, Preiss, 2000, Rolley and Wright, 2017, Schiller, 2000, Standing, 2005).

D1 denotes early bedding with a parallel schistosity, forming a slaty cleavage (S1) and major upright-to-inclined folds (F1). D2 denotes peak metamorphic conditions, producing a crenulation fabric (S2) overprinting D1, and tight-to-icoclinal weak folds (F2) preserved mainly in high-strain zones striking north-south. The third major deformation event, D3, features a series of regional open folds, faulting, and a weak crenulation (S3). However,

Rolley and Wright (2017) suggest these D3 events are not well-observed within the Kanmantoo Cu-Au deposit.

The deposit itself sits within a complex system of shear zones on the axial plane of the 'mine synform', a parasitic synform on the western limb of the Kanmantoo syncline (Oliver et al., 1998, Schiller, 2000, Seccombe et al., 1985, Standing, 2005). Schiller (2000) notes significant north-south-striking faults, with north north east-north east cross shears controlling deposit structure on a macro scale. Rolley and Wright (2017) highlight the association between the higher-grade Au zones and shear zones.

2.6 Paragenetic models

Two distinct prevailing theories dominate the Kanmantoo ore genesis debate. Authors including Seccombe et al. (1985) and Spry et al. (2017) propose a meta-exhalative, syn-sedimentary deposit model. Others, such as Oliver et al. (1998) and Rolley and Wright (2017), propose an epigenetic model related to metamorphism and igneous-intrusion-related fluids.

Supporters of a syn-sedimentary model suggest the Kanmantoo Cu-Au deposit formed within a stockwork feeder zone in a sub-seafloor hydrothermal exhalative system. Trace element studies of multiple indicator minerals (garnet, illmentite, biotite, staurolite, chlorite, muscovite, gahnite and magnetite) and stratigraphic equivalence within the Tapanappa formation have determined a proximal and genetic link between the Kanmantoo Cu-Au deposit and nearby Wheel Ellen and Angus Pb-Zn-Ag syn-sedimentary deposits (Belperio et al., 1998, Pollock et al., 2018). Sulphur isotope ratio results indicate sulphur extraction from a hydrous fluid source, in which the deposit formed in response to deep convective seawater circulation and near surface seawater discharge (Seccombe et al., 1985, Spry, 1976).

The majority of recent literature supports an epigenetic origin – proposing that the deposit formed in peak or post-peak metamorphic conditions, interacting with syn-orogenic intrusive igneous rocks during or immediately after D3 deformation, inducing major element metasomatism.

Oliver et al. (1998) suggests that higher sillimanite abundances provide evidence for local higher-grade metamorphism relative to other lithologies. High variance assemblages within the mine area suggest a post-peak metamorphic deposit, as assemblages are expected to break down to lower variance assemblages if an existing syn-sedimentary ore body is subsequently metamorphosed. Schiller (2000) supports this model, noting paragenetic variance and an association of peak metamorphic materials of a higher grade than surrounding lithologies, which cross-cut relict bedding.

Unlike the interpretations of Seccombe et al. (1985), sulphur isotope disequilibrium within the deposit is interpreted by Oliver et al. (1998) as the progression from peak to retrograde metamorphism. Research by Tedesco (2009) failed to identify any REE pattern anomalies indicative of an exhalative system.

Schiller (2000) concludes that a syn-sedimentary model is unreasonable unless a significant percentage of the evidence for the proposed seafloor feeder system has since been destroyed or ‘remobilised’. This continuing debate demonstrates that there are still significant gaps in our knowledge of the Kanmantoo Cu-Au deposit.

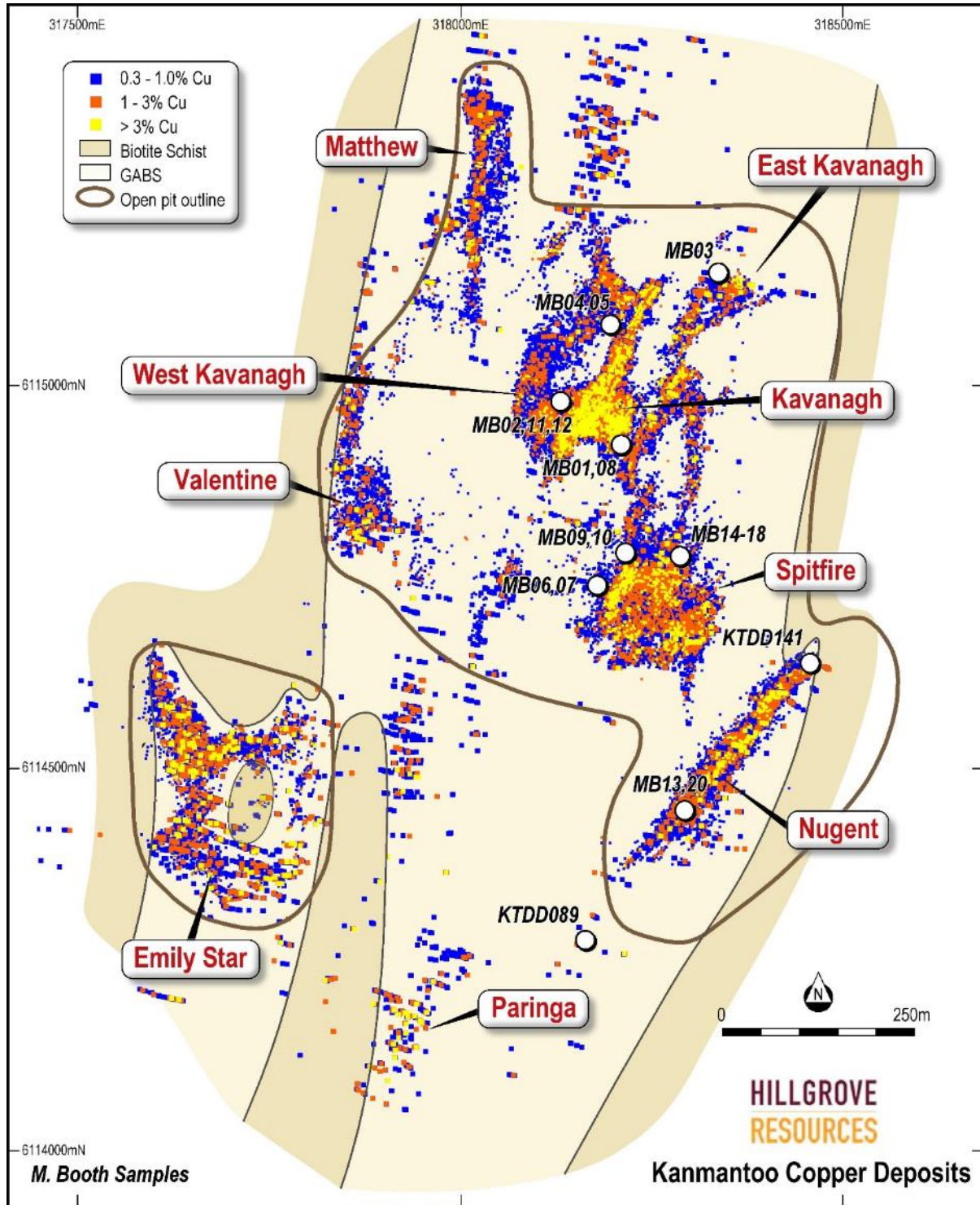


Figure 3: Kanmantoo Cu-Au deposit with wt. % Cu, displaying locations of grab samples and diamond drill hole samples collected for this study (Figure courtesy of Hillgrove Resources, adapted from Rolley and Wright, 2017).

2.7 Gold endowment

Although briefly mentioned by other authors (Arbon, 2011, Focke, 2010), Au distribution within the Kanmantoo Cu-Au deposit has not been the key focus of any previous investigation.

Within hydrothermal ore deposits, Au commonly occurs as ‘visible’ native Au hosted by sulphide minerals or as Au nanoparticles (‘invisible’ Au). Au nanoparticles are characterised by sub-microscopic Au (<1 µm) incorporated within the crystal structure of other minerals (Cook and Chryssoulis, 1990, Fleet et al., 1993).

Although chalcopyrite is the principle ore mineral of Cu at Kanmantoo, it is generally considered a poor trace element host (George et al. 2017). Within sulphide deposits, Au substitutes readily within arsenopyrite and arsenic-rich pyrite, and does not readily substitute within pyrrhotite or chalcopyrite. (Cook and Chryssoulis, 1990, Starling et al., 1989). Within the Kanmantoo deposit, metallurgical operating conditions are set to extract and recover 90-92% of Cu-bearing chalcopyrite, which is then refined and shipped as concentrate. As a by-product of this process, 50% of Au is recovered.

Mill data collected from the Kanmantoo Cu-Au deposit between December 2014 and July 2018 (Appendix F1) observes high Au:Cu ratios in the Spitfire and Nugent ore lodes.

Previous observations have suggested that the Au:Cu ratio increases towards the east, significantly in the Spitfire and Nugent ore lodes (Rolley and Wright, 2017).

METHODS

3.1 Field work and sample collection

Samples were collected with the aim of accurately representing Au distribution within the Kanmantoo Cu-Au deposit. Diamond drill core samples and open-pit grab samples were collected during January 2018, based on existing Au assay data and XRF field testing. 13 core samples from 10 different drill holes and 5 grab samples were collected from the East Kavanagh, Central Kavanagh, West Kavanagh, Spitfire and Nugent ore lodes.

in September 2017, mine geologists collected ore tailing concentrates from the Spitfire ore lode, with assay data indicating 3.94 g/t Au, which were produced into 30mm resin set blocks TT40a, TT40b. Gravity table ore concentrates with assays of 300 g/t Au were collected from Kanmantoo's Knelson concentrator, produced into 30mm resin set blocks TC3000a, TC300b and TC300c.

3.2 Petrography

In March 2018, 12 samples were sent to Ingham Petrographics in Queensland, producing 30-35 µm polished thin sections. A quartz-rich sample with sulphide veining, collected by Focke (2010) from the Nugent (formerly O'Neil) ore lode, was selected with assay data suggesting 10 g/t Au and 0.85% Cu for this interval, and produced 2 additional polished thin sections C58.1 and C58.2. A sulphide bearing felsic vein collected by Kimpton (2018) was selected to determine whether multiple sulphide phases were evident, and 2 additional polished thin sections (BK25A and BK25B) were produced. In total there were 16 polished thin section samples and 5 polished blocks. All samples were examined and imaged using an *Olympus BX51* optical microscope.

3.3 Mineral Insights Gold Sniffer

Gold Sniffer (manufactured by *Mineral Insights*) uses visible light and light reflectance algorithms to detect and estimate mineral concentrations $\geq 1.6 \mu\text{m}$. This instrument is an emerging industry tool for trace mineral and element detection but is yet to be referenced within peer-reviewed literature.

Gold Sniffer analysis was conducted in June 2018 at the South Australian Drill Core Reference Library on polished thin section sample MB15, and billets MB03, MB04, MB08, MB15, MB16, MB17, BK18, BK25A and C58-2.

Gold Sniffer was used to observe locations of Au within the sample suite by analysing its visible light reflection properties. Colour specifications for the reflection algorithm were based on an existing Kanmantoo Au setup and refined to inferred Au within the sample suite, as the visible reflection of Au varies with local composition. Contact margins between sulphides and other mineral phases produced positive results early in the session, and this was used as a guide for calibration on further sample traversing.

3.4 SEM-MLA

FEI Quanta 600 MLA SEM-MLA was conducted in May, July and August 2018 at Adelaide Microscopy on polished thin sections MB01, MB01.2, MB03, MB04, MB08, MB08.2, MB12.2, MB15, MB16, MB17, C58.1 and C58.2, and polished concentrates TT40A, TT40B, TC300A, TC300B and TC300C.

The SEM was equipped with a tungsten filament as an electron source for sample imaging, and set to back scatter electron (BSE) mode to produce high-quality greyscale imagery for visual observation of Au and other trace mineral grains. Considering Au and Au alloys (Au-Ag, Au-Bi) have a grey value of approximately 255, the greyscale detection limit was set to 240 to reduce the detection of non-Au trace elements and other host minerals.

MLA software generated colour-coded mineral maps for each sample. Au and other trace elements appeared as bright spots, given their greater atomic mass than the surrounding sulphides and host rock (Palenik et al., 2004). The map results and observed Au and trace element grains were cross-checked by energy dispersive spectral analysis (EDS) and visual observations, to avoid over-classification of Bi grains and other trace elements. Secondary electron detector mode (SE) was also used to confirm that the detections were trace elements and not sample surface issues, which appear as similar bright spots using BSE mode. High-resolution images of identified Au and other trace element grains were then captured with the SEM.

To confirm the *Gold Sniffer* results, the samples were cross-checked with the *Philips XL30 Field Emission Scanning Electron Microscope (FESEM)* (Figure 9). The areas of the sample billets where *Gold Sniffer* detected Au were compared with the corresponding thin sections (as well as the billet itself for MB15, MB16 and MB17). With greater magnification than the *Quanta 600*, the *XL30* was used to capture higher-resolution images of identified Au grains and other trace element grains, as well as observe microscopic grains (<2 μm).

3.5 LA-ICP-MS

LA-ICP-MS analysis was conducted in July and August 2018 at Adelaide Microscopy on polished thin sections MB01.1, MB04, MB08, MB12.2, MB15, MB16, BK25A, BK25B, C58.1 and C58.2, and polished concentrates TT40A, TC300B and TC300C.

The freeform holder was used due to the non-standard size of the polished thin sections. Laser energy varied day-to-day; July session fluence was 3 J/cm² with energy of 22 MJ and 100% attenuation, while August session fluence was 2.9 J/cm² with energy of 66 MJ and 50% attenuation.

Spot size varied between 29 μm , 43 μm or 51 μm depending on sample size, with a 30-second ablation time per spot. A greater acquisition time was set for significant elements and trace elements to ensure enough data was collected, with standards run every hour.

OBSERVATIONS & RESULTS

4.1 Petrography

The sulphide assemblage consists of chalcopyrite with lesser pyrrhotite, magnetite and pyrite as dominantly vein infill transgressing the existing metamorphic host rock. Host quartz, garnet and biotite are present in varying proportions (Figure 4, Figure 5). Samples vary slightly in their relative modal compositions of sulphides, mineral associations and schistosity (see Appendix A4 for full descriptions).

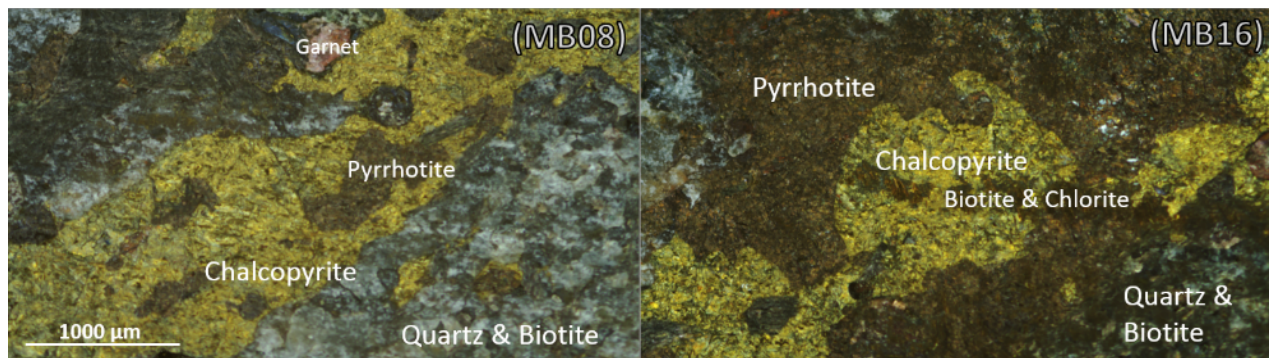


Figure 4: Sulphide textures observed within sample suite, displaying infill sulphide association with host GABS. Later-stage biotite and chlorite cross-cuts all existing units.

Rare pyrite within the sample suite is characterised by a well-formed cubic grain crystal shape. As noted by Taylor (2018), two stages of chlorite are observed – early chlorite (elongate well-formed with minor alteration of biotite) and late chlorite (including infill textures and the rimming of garnet grains). The sample suite appears paragenetically similar to those described by Schiller (2000) and others, and no 'visible' Au was observed petrographically.

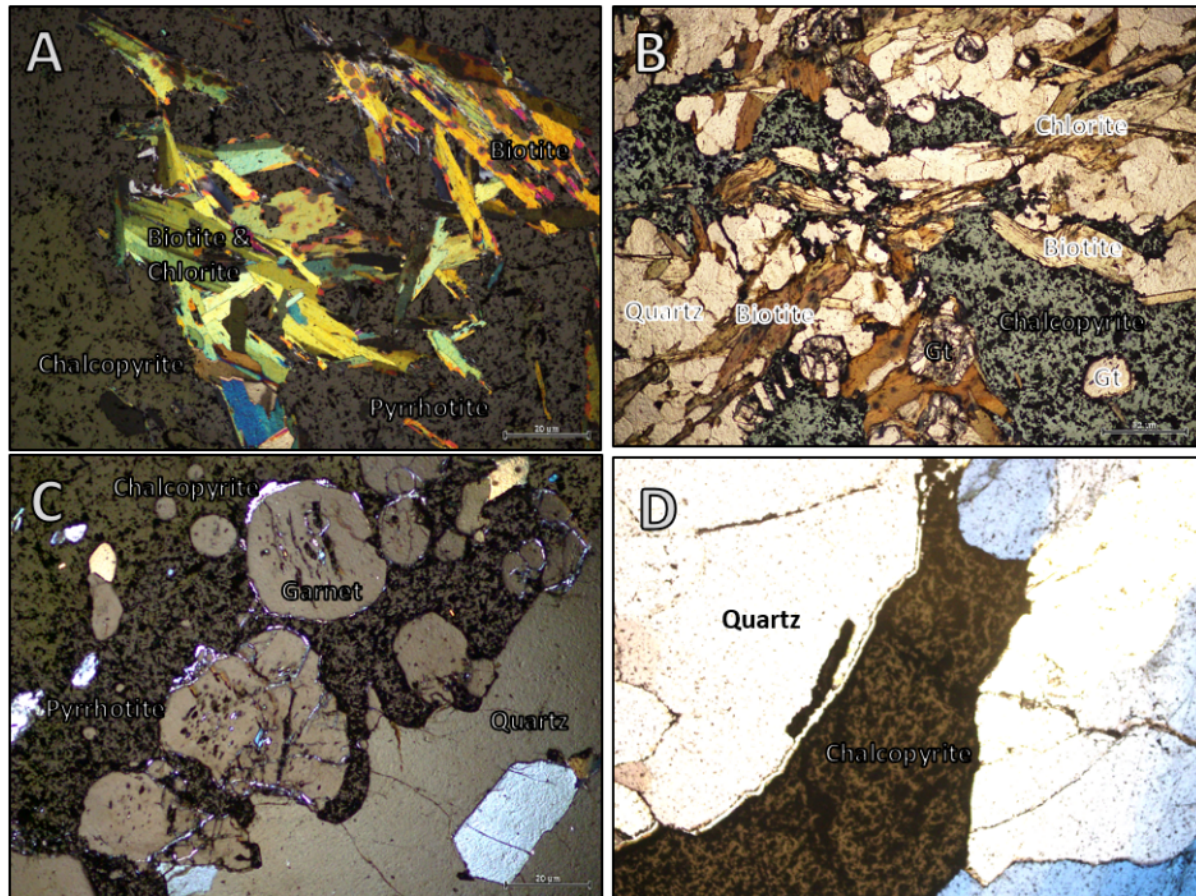


Figure 5: Interactions between sulphides and host rock, showing undeformed chalcopyrite and pyrrhotite infill texture with no major variation between ore lodes. Taken using an Olympus BX51 optical microscope. (A) MB01 (East Kavanagh ore lode), a schistose garnet biotite host rock with vein and vug infill and replacement sulphides, with alteration of biotite to chlorite and instances of chalcopyrite enveloping pyrrhotite. (B) MB03 (West Kavanagh ore lode), a biotite garnet quartz schist featuring loosely-connected vein infill sulphides parallel to schistosity, with alteration of biotite to chlorite. (C) MB16 (Spitfire ore lode), a biotite garnet quartz schist with irregular quartz and sulphide infill including magnetite, and 2 notable stages of chlorite (early elongate well formed with minor alteration of biotite – late infill and rimming garnet grains). (D) C58.1 (Nugent ore lode), quartz with chalcopyrite vein infill and significant limonite staining.

4.2 Mineral Insights Gold Sniffer

Gold Sniffer analysis identified multiple Au grains. However, subsequent visual investigations with the *Philips XL30 FESEM* (Figure 6) could not verify these results, and no Au grains were observed at the indicated Au localities.

The grains incorrectly identified as Au during *Gold Sniffer* analysis were subsequently determined by EDS spectral analysis and visual observations as:

- Other trace minerals with high reflectance, including native Bi/Bi-bearing sulphide minerals, molybdenum, galena, thorite and monazite.
- A false positive resulting from colour variation within a mineral (e.g. quartz)

Bi sulphides were the most commonly misidentified minerals during *Gold Sniffer* analysis.

Misidentified quartz-hosted Au was, in each case, a false positive – possibly as a result of impurities, weathering (iron staining) or refraction of micro-fractures.

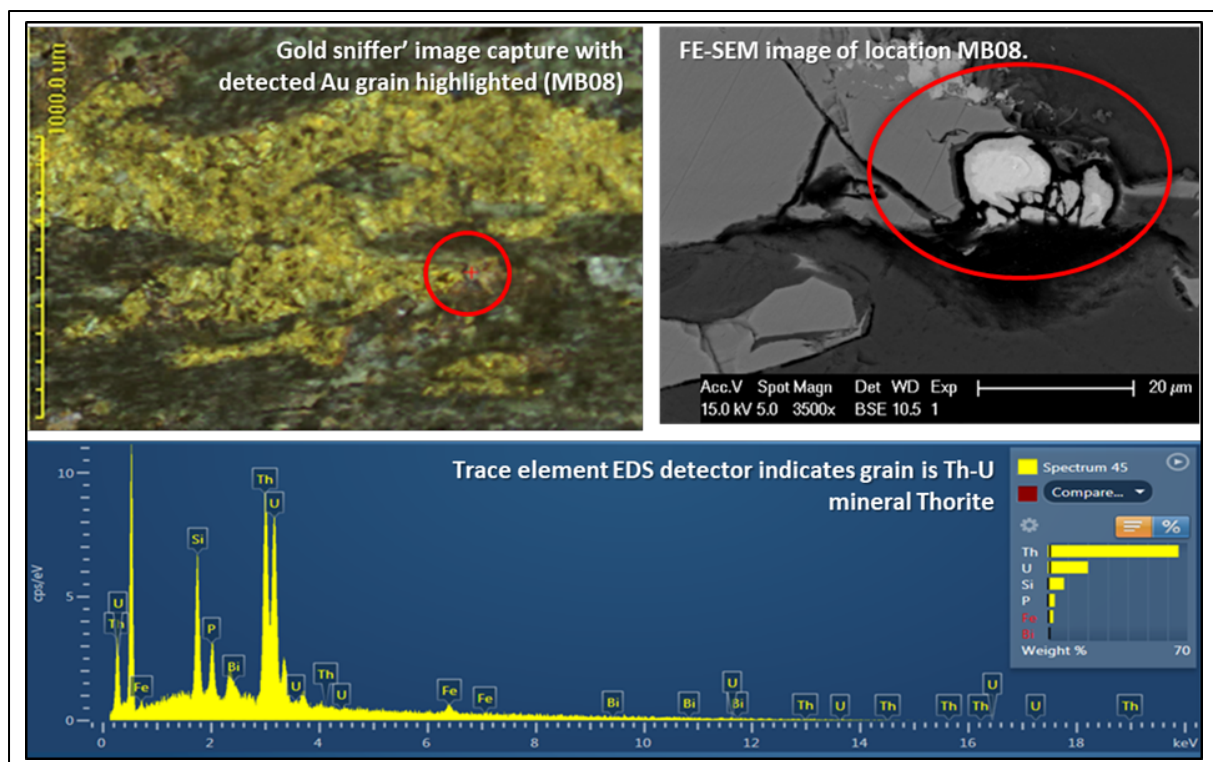


Figure 6: Process of validating *Gold Sniffer* results using the *Philips XL30 FESEM*. (Top left) Billet showing locations of image captures of MB08. (Top right) SEM image with detected ‘Au’ grain highlighted. (Bottom) Trace element EDS detector results for suggested Au grain indicates Th, U and Si; a response typical of the trace mineral thorite ((Th,U)SiO₄).

This short investigation cast doubt on the validity of previous *Gold Sniffer* studies of weathered core. Because of the unreliability of the *Gold Sniffer* results, they will not be discussed further. A full report on the *Gold Sniffer* investigation and corresponding SEM investigations can be found in Appendix B1.

4.4 SEM and LA-ICP-MS investigations of visible Au

SEM observations identified three textures of visible Au within the sample suite. These are:

- Sulphide-hosted Au
- Bi-associated Au
- 'Free' Au showing no host rock associations

Sulphide-hosted Au is characterised by 'visible' Au observed within chalcopyrite and magnetite (Figure 7). Although not a sulphide mineral, across the sample suite magnetite is observed within the same phase as the primary Cu bearing minerals: Chalcopyrite and pyrrhotite, and is grouped accordingly. Au observed within chalcopyrite is, in all cases, adjacent to quartz and situated along a chalcopyrite-quartz contact margin. Au grain shape preservation varies from a well-defined cubic crystal structure to rounded, poorly-defined grain edges with a clearer infill texture. Au was also observed as fracture infill within fractured magnetite (Figure 7).

Additional high reflectance grains of $<2 \mu\text{m}$ are also observed in samples MB15 and TC300C (Figure 7). Because of their small size, attempts to gain accurate EDS reference spectra for these 'bright' grains were inconclusive, as spectra were reflective of the surrounding host sulphides. However, given their close proximity to observed Au, these grains appear to represent Au 'micro-grains'.

Other trace elements identified within sulphides include native Bi or Bi-rich minerals, Pb-bearing minerals (e.g. galena), molybdenum, monazite, Th-bearing minerals (e.g. thorite), U-bearing minerals, or 'micro-grains' of minerals of unconstrained composition (since EDS spectral analysis reflects host composition) (Appendix C1). No visible Au was recognised within pyrrhotite or pyrite.

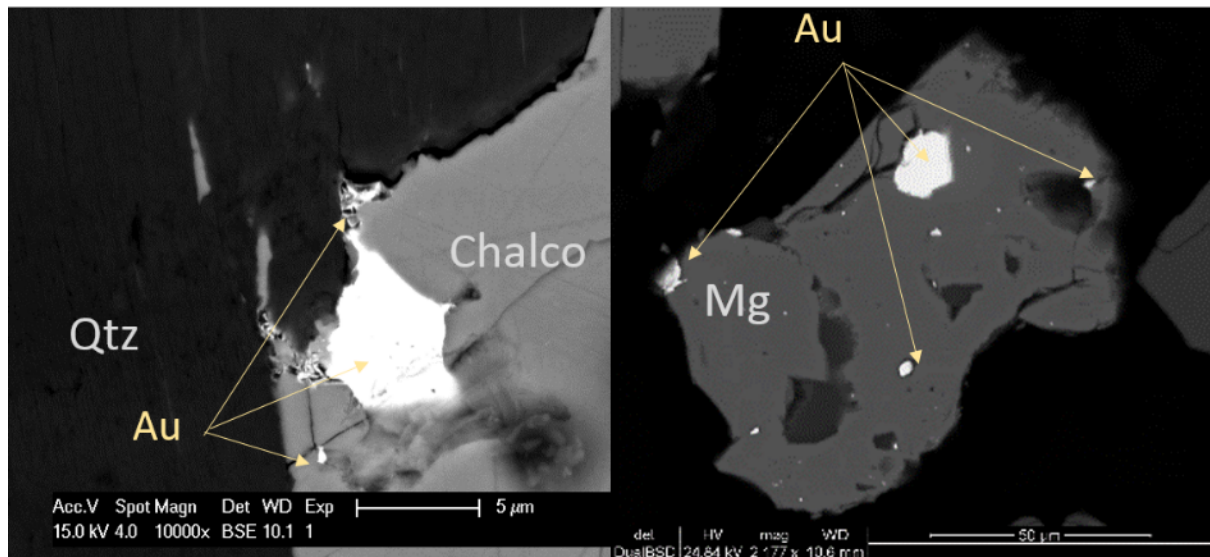


Figure 7: SEM images taken in BSE mode showing textural patterns and minerals associated with Au. (Left) Poorly formed Au grain (~4X4 μm) within chalcopyrite along contact boundary with quartz, with suggested Au ‘micro-grains’ (MB15). (Right) 12X12, 8x8 and 5x5 μm Au disseminated finely within magnetite. It is suggested Au 8X8 μm is a piece of a larger fractured Au grain (TC300C).

‘Free’ Au was observed within the sample suite as a single large (~200x500 μm) well-defined grain, with inclusions of magnetite and quartz observed (Figure 8). As ‘free’ Au is only observed in 300 g/t Au concentrate samples, the relationship between ‘free’ Au and host lithology is unconstrained at this time. However, the grain is interpreted to post-date the magnetite and quartz, providing evidence for an origin related to the main sulphide stage. LA-ICP-MS assay data of the ‘free’ Au grain indicates an Au:Ag association along with weaker Au:Cu and Au:Bi associations, signifying an origin related to the main sulphide stage. There is no recognisable association of ‘free’ Au with Au-compatible elements Pb, Zn, Co, Sb and As (Appendix E3). Assayed free Au contains low Mg, Al and Ti, and high-to-moderate Fe, Cu, Ag and Bi.

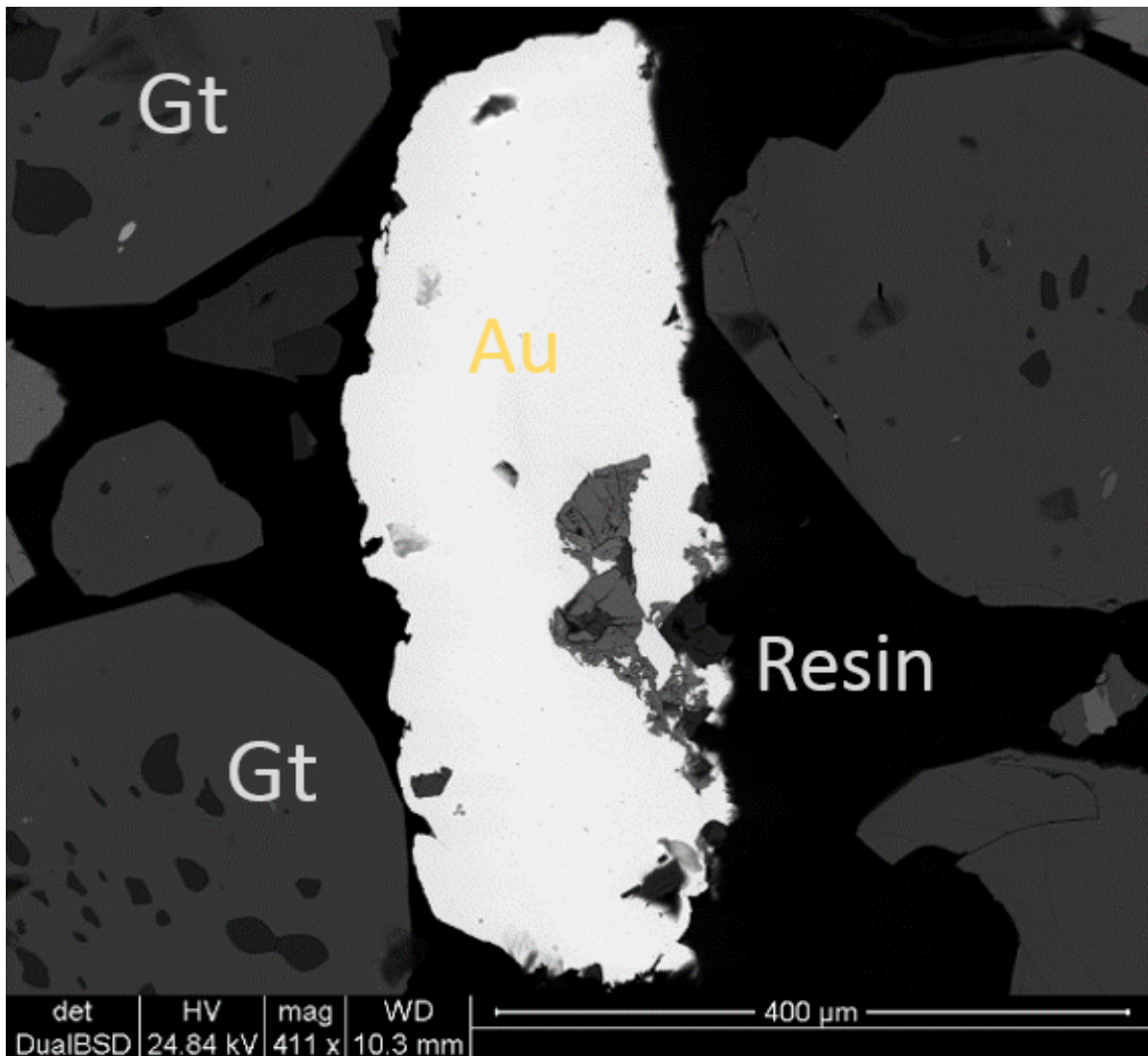


Figure 8: SEM image taken in BSE mode showing textural patterns and minerals associated with ‘free’ Au grain, ~200X500 μm with quartz and magnetite inclusions (TC300C).

Au:Bi intergrowth is observed within the sample suite (Figure 9). Bi-associated Au is characterised by Au with little-to-no defined grain shape inter-grown with native Bi, showing no association with any other minerals (Figure 9, Appendix C3). Although Au is rarely observed within the sample suite, Bi is observed in all named ore lodes except Nugent, with significant Bi observed in West Kavanagh. However, as mentioned this sample suite is considered unrepresentative, as mill data disputes this (Appendix F1).

Bi and Bi-rich veins are observed cross-cutting and surrounding existing mineral phases, and are often observed at or along contact boundaries between quartz and sulphides.

Within assayed Bi grains, East Kavanagh contains the highest Au (5.2 ppm) alongside the greatest Ag (150 ppm) (Figure 10, Figure 11). Bi varies within the named ore lodes, with the highest average Bi (8.6 ppm) observed in the East Kavanagh ore lode and the lowest average Bi (0.47) measured in the Nugent ore lode.

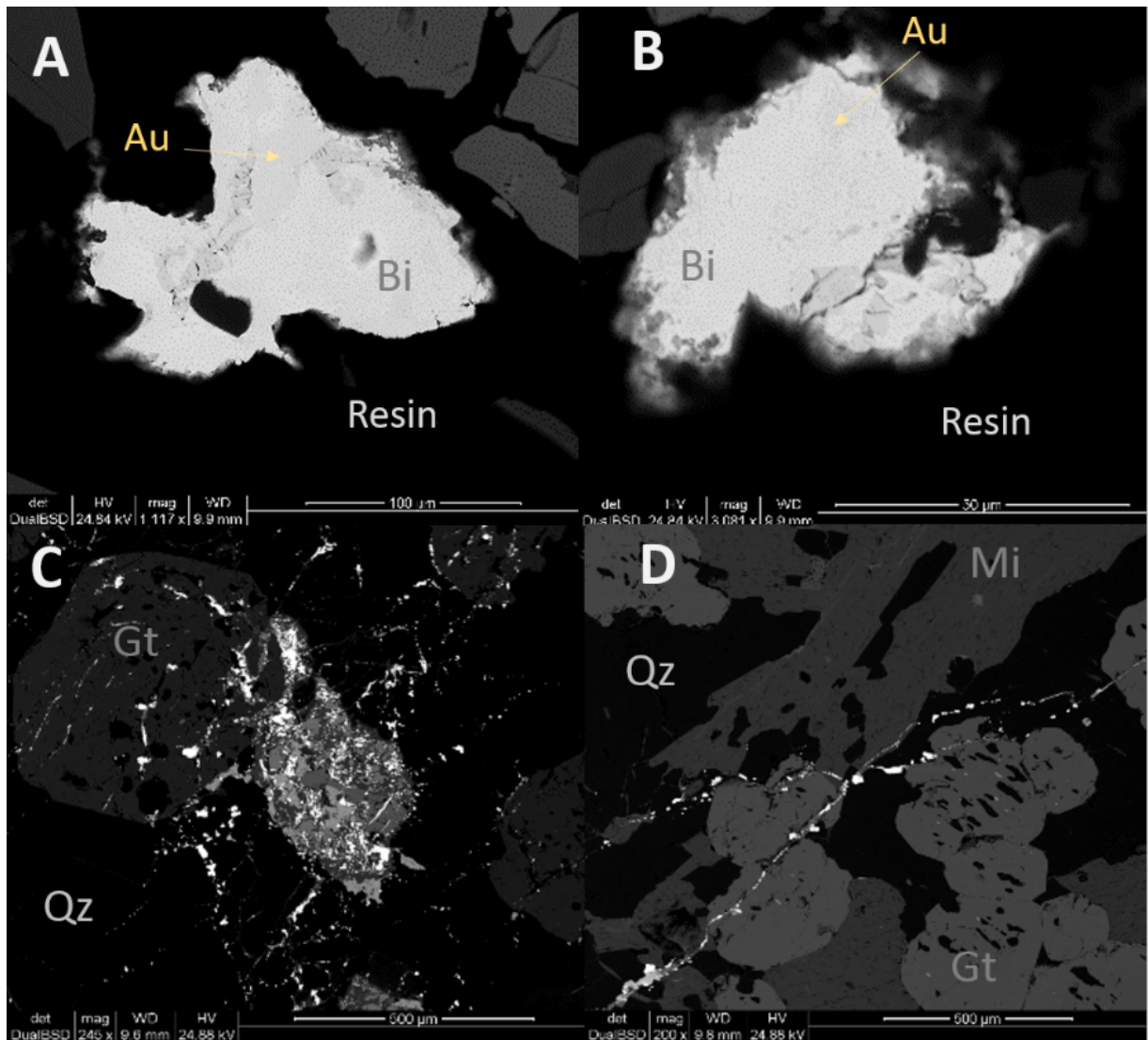


Figure 9: SEM images taken in BSE mode showing distribution of Bi within the sample suite. (A & B) Au intergrowth with Bi, where Bi is more dominant (TC300B). (C & D) Bi (bright grains) cross-cutting existing mineral phases, suggesting Bi-associated Au and Bi-rich fluids are late in the paragenetic sequence.

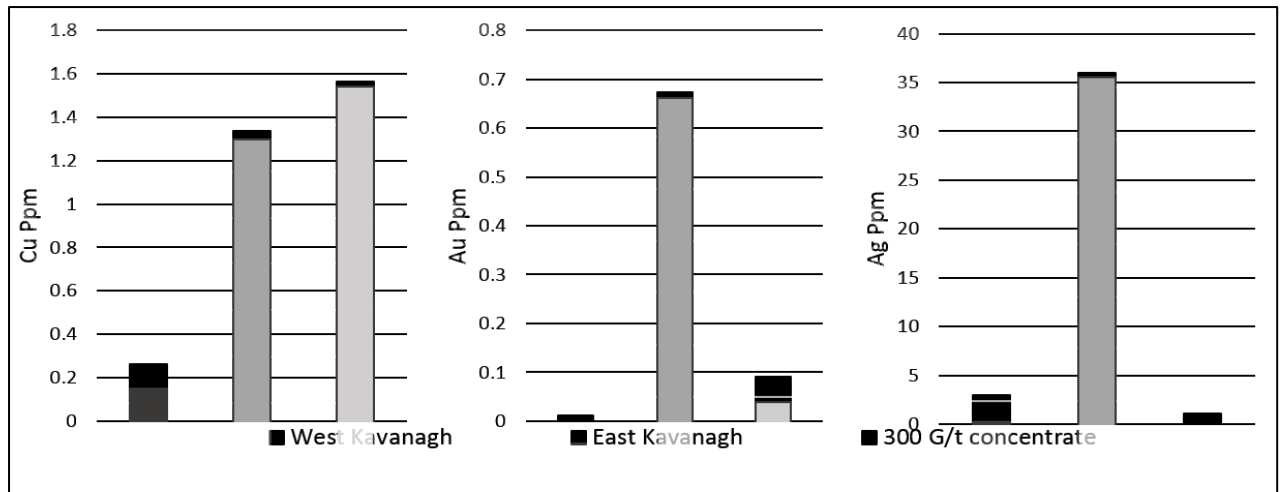


Figure 10: Bi LA-ICP-MS data showing variations in Cu, Au and Ag ppm across different ore-lodes within the Kanmantoo Cu-Au deposit. Wt% Bi of 98% used for calculations. Full element suite available in appendix E1, including Fe, Mg, Al, Si, S, Ti, V, Cr, Mn, Co, Ni, Cu, Zn, As, Se, Mo, Ag, Cd, Sn, Sb, Te, Hf, Ta, W, Au, Hg, Tl, Pb, Bi and Th.

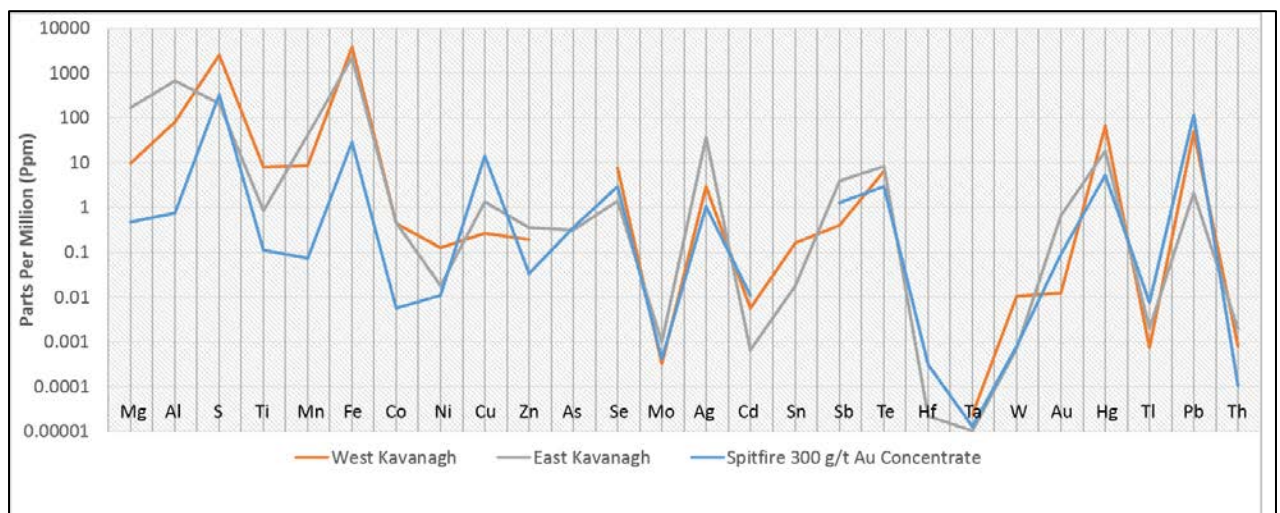


Figure 11: Bi assay data from the West Kavanagh and East Kavanagh ore lodes and Spitfire 300 g/t mill concentrate, with values for quantifiable elements in ppm. Wt% Bi of 98% used for calculations n=79.

4.5 LA-ICP-MS investigation of 'invisible' Au

In total, 1171 LA-ICP-MS spots were analysed. Quantitative geochemical data was collected for grains of chalcopyrite (106 locations), magnetite (14 locations), pyrite (4 locations), pyrrhotite (60 locations), Bi (23 locations) and Au (1 location). A fourth pattern – Au nanoparticles within host minerals – was identified through LA-ICP-MS analysis.

LA-ICP-MS analysis confirmed the existence of Au nanoparticles ($>1 \mu\text{m}$) within main- ore stage sulphides and the paragenetically-later Bi-sulphide grains. Au nanoparticles were detected during LA-ICP-MS assaying, but not during petrographic or SEM observations (Ciobanu et al., 2011, Cook and Chryssoulis, 1990, Reich et al., 2006). Two forms of Au nanoparticles were identified: Au nano-inclusions and solid-solution Au (Figure 12).

Represented as counts per second over acquisition time (CPS), Au nano-inclusions appear as noticeable spikes in Au CPS, and are distributed heterogeneously within mineral grains. Solid-solution Au, also known as ‘lattice-bound’ Au, appears as stable CPS abundances across a mineral grain. Both Au nano-inclusions and solid-solution Au are present within chalcopyrite, pyrrhotite, pyrite, magnetite and Bi grains.

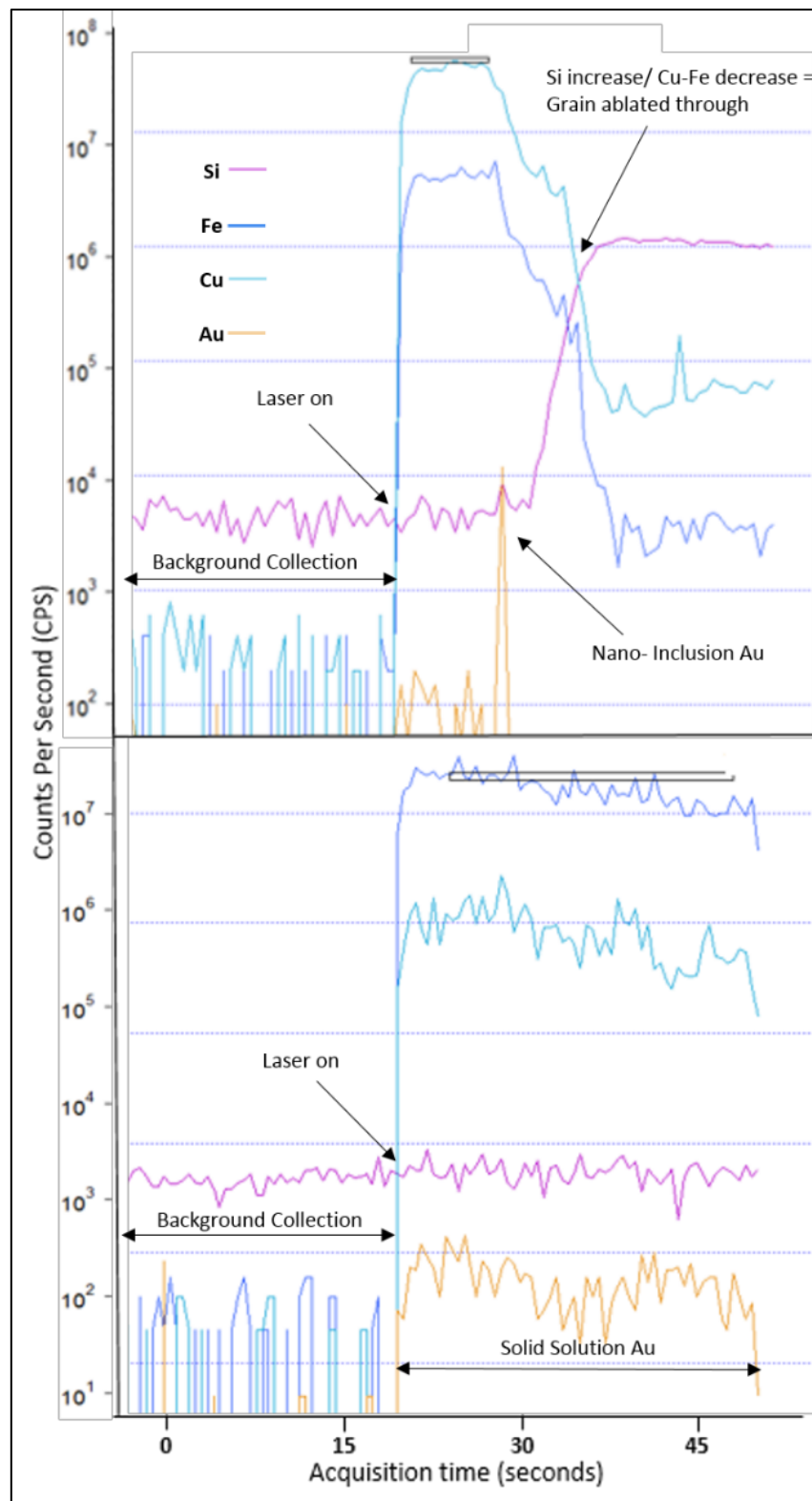


Figure 12: LA-ICP-MS spot data for 2 chalcopyrite grains. (Top) Au nano-inclusion, recognisable by distinct Au CPS spike (MB08.2). (Bottom) Solid-solution lattice-bound Au, recognisable by steady concentration across grain over acquisition time. The sharp increase in Fe and Cu CPS indicates the chalcopyrite grain is being ablated, and a signal is being collected. The visible decrease in Fe and Cu CPS, as well as the increase of Si, indicates the chalcopyrite grain has been fully ablated, and the signal is now reflective of underlying mineral or thin section glass. There is no visible Si decrease in the bottom chalcopyrite grain as this is a larger grain which has not yet been fully ablated. The grey bar indicates the section of ablated grain signal used for further processing.

Au was detected most frequently within chalcopyrite and Bi grains (Table 1). It is inferred that the Au detected within chalcopyrite is characteristic of sulphide-hosted Au and Au nanoparticles, while the Au detected within Bi is characteristic of Bi-associated Au and Au nanoparticles. Notably, the highest counts of Au nanoparticles are found within Spitfire concentrate tailings (Table 2). However, these counts are not systematically related to average Au ppm of assayed minerals within the named ore lodes.

Table 1: LA-ICP-MS spots for analysed minerals containing Au above detection limits, indicating greater Au nanoparticles within chalcopyrite and Bi.

Mineral	Number of spots containing Au	Percentage of Spots containing Au
Chalcopyrite	245/513	47.7%
Pyrrhotite	26/262	10.3%
Pyrite	3/22	12.6%
Magnetite	10/45	22.2%
Bi	37/79	46.8%

Table 2: LA-ICP-MS spots for chalcopyrite (separated by sample location) indicating greater counts for Au nanoparticles within East Kavanagh, BK25, Spitfire grab samples and Spitfire 3.94 g/t Au tailing concentrates, and no correlation between counts of Au and average ppm Au.

Ore Lode	Number of spots containing Au	Percentage of Spots containing Au	Average ppm Au
West Kavanagh	21/55	38.20%	0.076
East Kavanagh	28/45	62.20%	0.117
BK25	66/104	63.46%	0.061
Spitfire grab sample	27/42	64.28%	0.156
Spitfire tailings 3.94 g/t Au	46/60	76.67%	0.099
Spitfire concentrate 300 g/t Au	47/112	41.90%	0.127
Nugent	10/95	10.50%	0.039

As discussed below, the LA-ICP-MS results collected from the Nugent ore lode are not considered representative of the main Cu-bearing ore body.

The named ore lodes show variations in major and trace elements (Figure 13). Pyrrhotite and pyrite show high Co and Ni content, with high Cu observed within chalcopyrite. Au within

chalcopyrite shows very weak to no correlation between Cu, Co, Ni, Zn, Se, Sb and As.

However, a positive Au:Ag relationship ($R^2=0.984$) is observed in the Nugent ore lode. The named ore lodes show a weak negative Au:Co and Au:Ni relationship except for Spitfire, which shows a weak positive relationship for Co ($R^2=0.0753$) and Ni ($R^2=0.0722$). Within chalcopyrite, the Spitfire ore lode contains the highest average Au (0.15 ppm), while the West Kavanagh ore lode contains the highest average Cu (370803 ppm) and Ag (159 ppm) within chalcopyrite (Figure 14). Trace values of elements such as Mg, Al, Ti and Pb within sulphides vary across the named ore lodes, and no spatial distribution patterns are recognised (Figure 13).

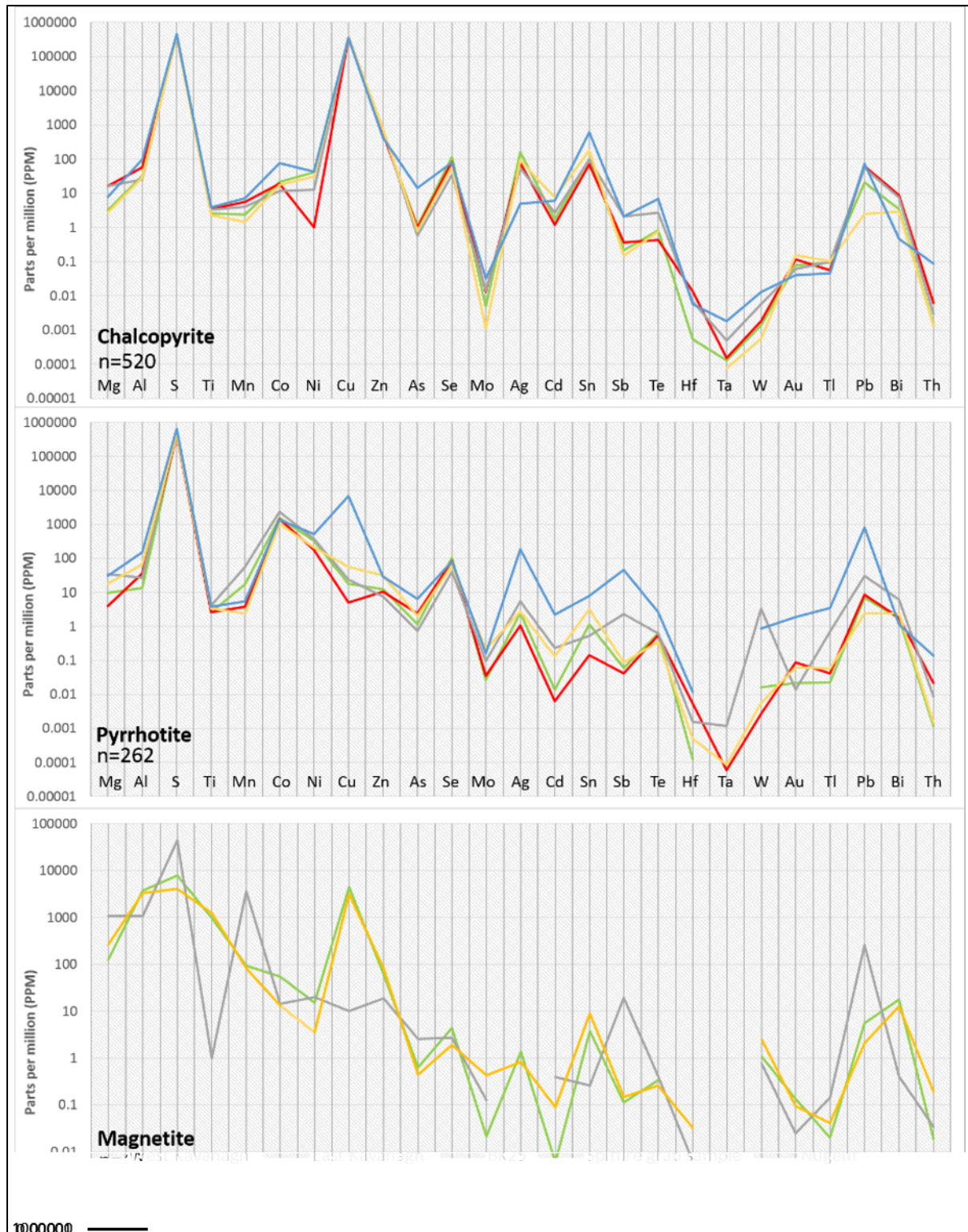


Figure 13: Sulphide geochemistry classified by different ore lodes. Cu and Au within chalcopyrite vary but not as a result of spatial location. Magnetite is not observed within the Nugent ore lode sample suite. Nugent shows the greatest variation, with higher As and lower Ag and Bi than other named ore lodes, while East Kavanagh contains lower Ni. Pyrrhotite and magnetite show greater variation between the named ore lodes; it is inferred that with a larger sample size these minerals would appear homogenous, similarly to chalcopyrite. Wt% Fe of 30.5% for chalcopyrite, 61% for pyrrhotite, 72% for magnetite and 56.5% for pyrite was used for calculations.

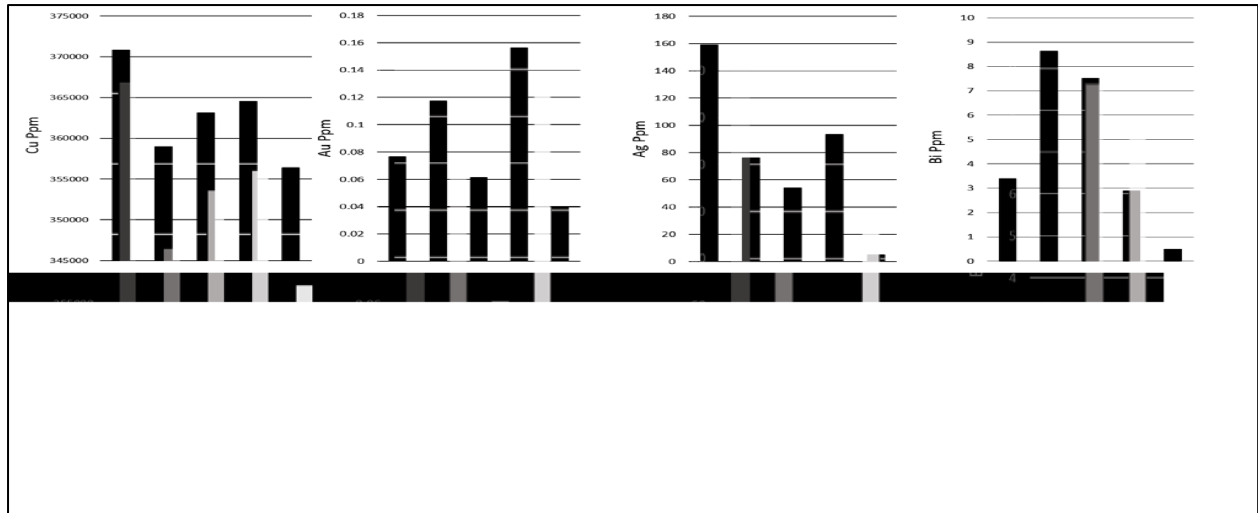


Figure 14: Chalcopyrite LA-ICP-MS data showing variations in Cu, Au, Ag and Bi ppm across different ore lodes within the Kanmantoo Cu-Au deposit. Wt% Fe of 30.5% for chalcopyrite was used during Iolite calculations. Full element suite includes Fe, Mg, Al, Si, S, Ti, V, Cr, Mn, Co, Ni, Cu, Zn, As, Se, Mo, Ag, Cd, Sn, Sb, Te, Hf, Ta, W, Au, Hg, Tl, Pb, Bi and Th.

LA-ICP-MS assay data for sulphides with visible Au varies from that of sulphides without visible Au. The chalcopyrite-hosted Au within sample MB15 contains higher Au (0.197 ppm) than the average for the Spitfire ore lode (0.1566 ppm). Chalcopyrite-hosted Au contains higher Cu, lower Ni, Co and Ag; and As is below detection limits.

Samples BK25A and BK25B, collected by Kimpton (2018), present a different trace element profile for magnetite, however maintain similarity with the primary sample suite within chalcopyrite and pyrrhotite (figure 13). There is no evidence at this stage to suggest these samples represent a paragenetically younger sulphide vein set, however at this scale regional variation may be obscured.

LA-ICP-MS assay data was collected from Spitfire grab samples, tailings from Kanmantoo's Knelson concentrator (3.94 g/t Au), and gravity table concentrates (300 g/t Au) to investigate the efficacy of current Au recovery at the Kanmantoo Cu-Au deposit (Appendix E2). As expected by density, within chalcopyrite the highest Cu ppm (379700 ppm) is found in the gravity table concentrates, with the lowest Cu ppm (279963 ppm) found in the concentrate

tailings. This trend is repeated for Au at 0.2166 ppm and 0.0993 ppm, but not for Ag. Gravity table concentrates contain the highest Mo, Co and Ni, and the lowest Zn.

4.6 Zonation of Sulphides and other trace elements

A semi-quantitative raster map of sulphide-hosted Au and surrounding minerals in MB15 was produced to determine host associations with Au. Variations in major elements, such as Al, Si and Fe, identify grain boundaries and variation between garnet, chalcopyrite and quartz (Figure 15).

Although the visible Au within this sample is hosted within chalcopyrite, an Au:Ag:Bi:Hg association is observed, suggesting these elements were introduced into the system within the same phase. This assemblage is typical for low-temperature retrograde hydrothermal fluids.

A Co:Ni association is observed, likely hosted within a Cu-Co-Ni sulphide, such as carrollite. Co and Ni rim host garnet and quartz grains, suggesting these transition metals postdate host GABS mineralisation (Groves and Baker, 1971, Hitzman et al., 2017). A Zn:Cd association is observed, likely hosted within sphalerite. The Cd:Zn ratio within sphalerite is dependent primarily on this ratio within ore-forming fluids (Schwartz, 2000). A Ta:W association is observed, likely hosted within an unidentified Ta-W mineral. The associations mentioned are typical of sulphide ores, given their physical and chemical similarities (Moats and Davenport, 2014).

As, Te, Hf and Th show no observable patterns (likely due to signal noise). Maps of Au, Ag, Hg and Bi in logarithmic scale alongside the raster location map can be seen in Appendix E4.

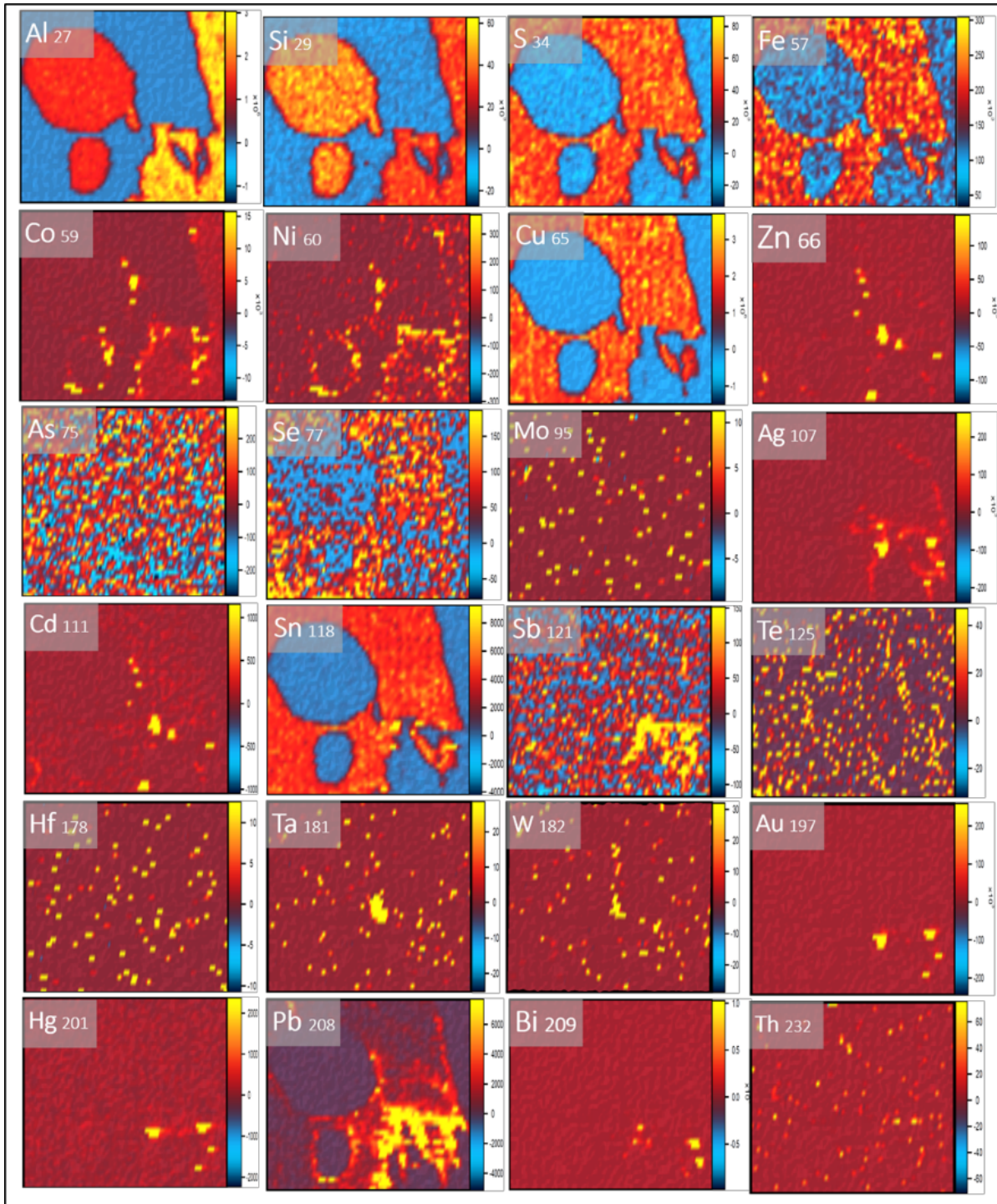


Figure 15: LA-ICP-MS raster map for known Au grain location and surrounds (sample MB15), ordered by atomic mass – where yellow indicates higher relative concentrations in counts per second.

Grains of chalcopyrite, pyrite, Bi and Au were assayed to determine any elemental zonation present within the mineral (Figure 11). Within chalcopyrite, it is inferred that spikes of Au, Ag, Bi, Co and Zn represent nano-inclusions rather than grain zonation.

Within chalcopyrite, Co:Zn and minor Au:Cu correlations are observed. Pyrite contains relative depletion of Zn and Bi in the core and rim, with only minor Au and no recognisable As. No strong zonation or relative enrichment of Co or Ni is recognised within pyrite. Bi grains show relative Co depletion in the core, relative enrichment of Te and Ag in the core, and relative depletion of Ni in the core and rim.

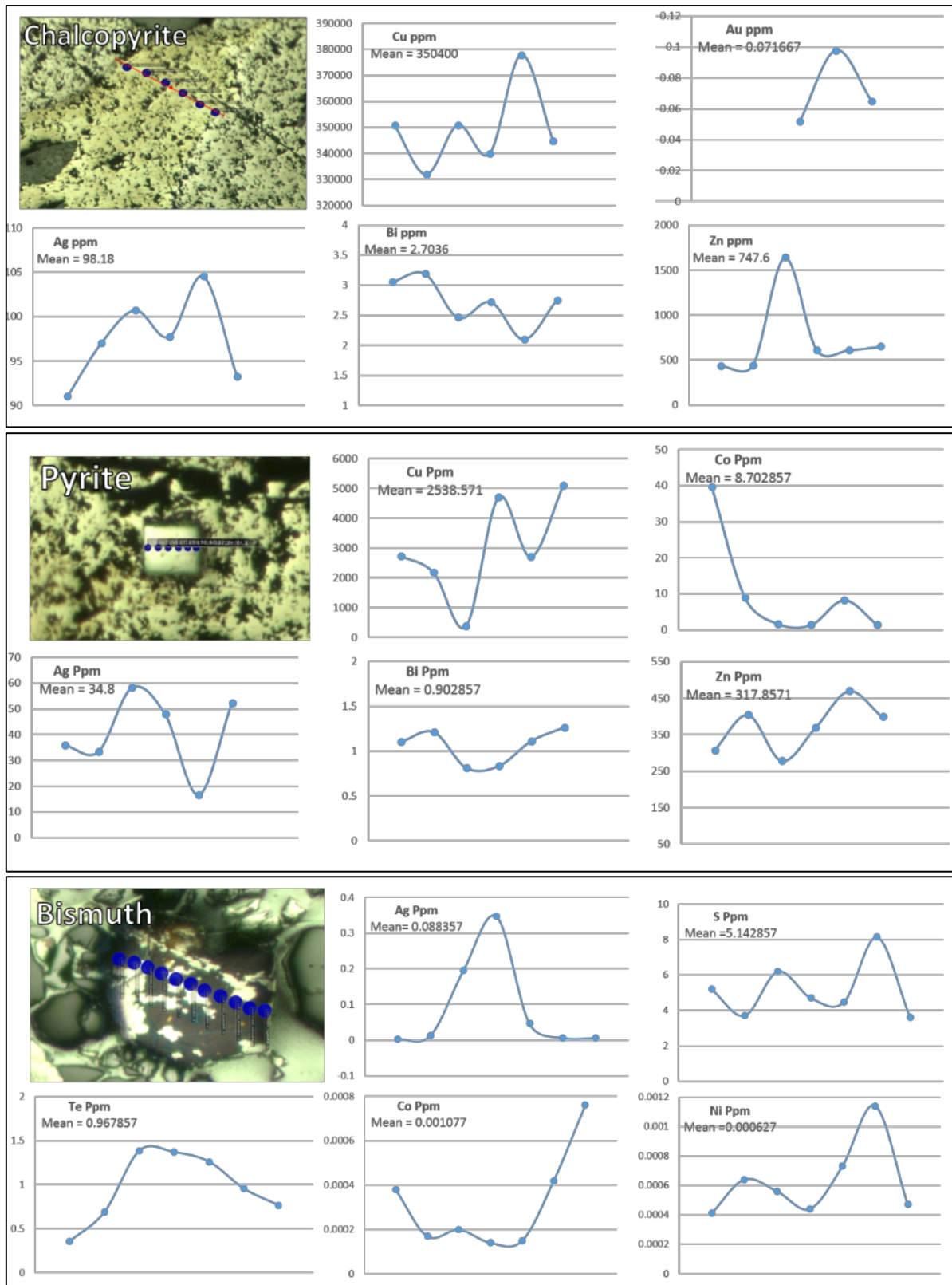


Figure 16: LA-ICP-MS assay data showing zonation within mineral grains. (Top) Spot data for chalcopyrite in the Spitfire ore lode, showing reflective behaviour of Cu and Bi within chalcopyrite, and a relationship between Cu, Au and Ag. (Centre) Spot data for pyrite in the West Kavanagh ore lode, showing zonation of Bi and Zn; this grain contains minor Au and no As. (Bottom) Spot data for Bi grain in 300 g/t Au concentrate, demonstrating zonation of Te, Co and Ag within Bi grains. This sample contained minimal Cu, Au and no As.

4.7 Summary of Results

Au grains were observed in 3 out of 17 samples, and trace Au was detected by LA-ICP-MS analysis of several minerals, resulting in 4 textural settings of Au:

- **Sulphide-hosted Au:** hosted within chalcopyrite and magnetite, along or near a contact boundary with quartz
- **Bi intergrowth Au:** intergrown with Bi, where Bi is the more dominant phase
- **‘Free’ Au:** loose Au grain with inclusions of magnetite and quartz
- **Au nanoparticles:** 'invisible' nanoparticles (<1 µm) within the matrix of host minerals as Au nano-inclusions or lattice-bound solid-solution Au

DISCUSSION

Having identified 4 key textural settings of Au within the Kanmantoo Cu-Au deposit, this study can now further constrain the paragenesis of Au within the deposit, and the impact of relative spatial location on variation in Au behaviour within the named ore lodes.

5.1 Review of Methodologies

Field sampling targeted identified Au in existing assay data. However, the sample suite contained less visible Au than anticipated, most likely because of ‘nuggetty’ (heterogeneous) Au distribution. Even though few visible Au grains were detected within the sample suite, reasonable confidence is maintained in the SEM results, since the *Philips XL30 FESEM* spectral matching recipe for Au classification maintains low variation (99.96% similarity across the sample suite) (Appendix C2).

5.2 Cu:Au and other Au associations

Mill data from the Kanmantoo Cu-Au deposit presents a Cu:Au association, with noted variation with relative spatial location (Appendix F1). Within this study, Au is noted within Cu-bearing sulphides across all named ore lodes, however data from this study indicates no clear systematic relationship between Au and Cu concentrations. Cu:Au associations maintain poor linearity and show no change with relative spatial location (Appendix E3). Given the minimal Cu:Au association observed within this sample suite, it is suggested the Cu:Au associations present within the Kanmantoo Cu-Au deposit is not the singular cause of varying Au distribution across the named ore lodes, and it is instead the result of multiple or varying processes.

As:Au associations (mainly within pyrite and arsenopyrite) are widely-observed within Au deposits globally (Cook et al., 2013, Cook and Chrysoulis, 1990, Fleet et al., 1993, Hewett, 2017, Reich et al., 2005). Compared to other Au-sulphide deposits, the Kanmantoo Cu-Au deposit features a relative depletion of As, and no systematic relationship between Au and As concentration is recorded. Although there are examples of As-poor Au deposits (Cook et al., 2009, Ciobanu et al., 2011, Mao et al., 2003), As is still regarded as a key facilitator for the substitution of Au within sulphide minerals. Within existing Au deposits, pyrite and arsenopyrite are the major sulphide hosts for nanoparticles of Au, with many highlighting the importance of an Au:As link for Au nanoparticle stability (Cook and Chrysoulis, 1990, Fleet et al., 1993, Reich et al., 2005). The scarcity of As and pyrite at Kanmantoo is consistent with the below-average nanoparticle Au observed within pyrite, and heterogenous distribution of visible Au within the deposit at large.

Other major elements (Mg, Al, S, Ti, Mn and Pb) and trace elements (Co, Ni, Zn, As, Se, Mo, Cd, Sn, Sb, Te, Hf, Ta, W, Tl and Th) have an unsystematic variation across the named ore lodes. The Nugent ore lode maintains highly variable major and trace element composition.

These results are difficult to reconcile with those measured within the other named ore lodes (Table 2, Figure 14). The Nugent samples in this sample suite were collected by Focke (2010) and are quartz-rich with sulphide veining. These samples contain only minor Cu and Au, exhibiting similarity to the sulphide-bearing quartz veins (SQV) described by Lyons (2012). While the Nugent results do not clearly represent the main Cu-bearing ore body, there is merit in their representation of post-peak SQV.

5.3 Sulphide-hosted Au

Observation of Au within sulphides in the Spitfire ore lode is a clear indicator of Au entering the system with the main ore event. Arbon (2011) suggests that Cu and ore-bearing fluids predate Au mineralisation. However, Focke (2010) suggests almost all sulphides within the Kanmantoo Cu-Au deposit and surrounds are Au-enriched. SEM and LA-ICP-MS results from this study indicate an association between Au and the primary Cu-bearing ore body.

A mechanism is proposed for ‘early’ Au, where Au enters the system with the main ore fluid (and/or Fe-Mg rich hydrothermal alteration fluid), and subsequently forms nano-inclusions and solid-solution Au within the primary Cu-bearing sulphides (Arbon 2011). Visible native Au grains form along phase boundaries between sulphides and country rock when the solubility limit of chalcopyrite is reached, or because a post-peak metamorphic event in the history of the deposit (such as the reactivation of East-dipping compressional faults) causes nanoparticle Au to destabilise (Palenik et al., 2004, Wilson, 2009). By association, chalcopyrite and other sulphides within the Spitfire ore lode appear to have a lower Au solubility threshold, as visible sulphide-hosted Au is observed only within this ore lode. If the Spitfire ore lode is further from the main ingress of mineralising fluids, Au most likely crystallised late in the mineralisation sequence, after the hydrothermal fluid had cooled.

5.4 Bi-associated Au

Au:Bi intergrowth is observed within the Spitfire ore lode, where mineralogy is dominantly Bi with minor accessory Au. The study of Au:Bi associations has focused mainly on deposits where this is a known key assemblage, such as the Maldon deposit in the Victorian goldfields (Ciobanu et al., 2010). It is widely-accepted that Bi melts can scavenge Au from hydrothermal fluids, and that these melts can contain higher Au than co-precipitating fluids (Martinez, 2013, Tooth et al., 2008, Tooth et al., 2011, Tooth, 2013).

Bi is well-observed cross-cutting sulphide hosted Cu, suggesting that Bi entered the Kanmantoo system after the main ore stage (Arbon, 2011). However, Bi is also observed as small inclusions within chalcopyrite and pyrrhotite (Appendix D1) LA-ICP-MS assay data also notes Bi nanoparticles within chalcopyrite, pyrrhotite, pyrite and magnetite, observed primarily as lattice-bound solid-solution Bi.

In contrast to Arbon (2011), who did not identify significant abundances of Au within a Bi-focused sample suite, the LA-ICP-MS data observed Au nanoparticles within 46.8% of assayed Bi, with the highest Au (5.2 ppm) observed within the East Kavanagh ore lode. It is proposed that minor Bi was associated with the primary ore fluid, while the majority of Bi entered the system with later Bi-rich hydrothermal fluids.

Bi grains from the Spitfire ore lode were analysed with the EDS spectral scanner on the *Philips XL30 FESEM* to assess the validity of the Bi:Au relationship, as well as the potential use of Bi as an ‘Au pathfinder’, as suggested by Ciobanu et al. (2005) and Tooth et al. (2008). However, visible Bi grains displayed no significant Au (Appendix C1).

Relative Bi ppm within assayed sulphides varied significantly between the named ore lodes. The findings of this study maintain an Au:Bi relationship as proposed by previous authors

noted above. Despite the presence of trace Bi in 97.6% of sampled sulphides, Bi is not a reliable pathfinder for the presence of Au.

5.5. 'Invisible' Au

Au nanoparticles (<1 µm) are observed within all sulphides across all named ore lodes – with 47.7% of assayed chalcopyrite containing Au nanoparticles (up to 0.89 ppm). Within the Kanmantoo Cu-Au deposit, nanoparticle Au is measured within chalcopyrite, pyrrhotite, pyrite, magnetite and Bi grains within the sample suite.

Simon et al. (2000) carried out experiments on Au-Cu-Fe-S systems to determine average Au accommodation within chalcopyrite. Their findings suggest chalcopyrite can accommodate a higher concentration of Au within its crystal structure at higher temperatures (2-4 ppm at 400°C, 5-16 ppm at 500°C, and 100-125 ppm at 600°C). Au within the Kanmantoo Cu-Au deposit is measured at the lower end of this system (an average of 0.09 Au ppm) within chalcopyrite. This suggests chalcopyrite is Au under-saturated. The low concentration of Au and the lack of precipitated visible Au inclusions suggest an Au-poor source rock (Ciobanu et al., 2011, Reich et al., 2005).

Increasing metamorphism is reported to promote movement of nanoparticle Au to visible Au inclusions, as nanoparticle Au stability limits are exceeded (Chang et al., 2008, Cook et al., 2013, Vikentyev and Vikentyeva, 2015). Although nanoparticle Au can remain stable at high metamorphic regimes, Au nanoparticles have a much lower melting point than bulk Au (~1064 °C), where thermal stability depends on particle size and host mineralogy (Cook et al., 2009). Reich (2006) found that Au nanoparticles begin destabilising at ~370°C. Sandiford et al. (1995) and Pollock (2018) give temperatures of 550-600°C and ~518-546°C for peak metamorphism, exceeding the stability field for Au nanoparticles. This evidence, combined

with the rarity of visible Au observations within the Kanmantoo Cu-Au deposit, suggests Au crystallised at late-peak to post-peak metamorphism.

Tedesco (2009) observed TitaniQ results of 355-395°C for quartz vein formation, at pressures of 2.6-3.4 kbar. Arbon (2011) conducted geothermometry on chlorite-associated veining and determined that hydrothermal alteration temperatures vary from 300-400°C within the Kanmantoo Cu-Au deposit. The stability field for Au nanoparticles, together with the lack of significant precipitated inclusions of Au, provide further support for a late-peak to post-peak metamorphic development for Cu-Au bearing sulphides.

The existence and distribution of nanoparticle Au is not recommended as a pathfinder for visible, economic Au within the Kanmantoo Cu-Au deposit, since the location of nanoparticle Au has no meaningful correlation with average Au ppm (Table 2). Further investigations should consider whether Au recovery can be improved to retain higher levels of nanoparticle Au.

5.6 Au paragenesis within the Kanmantoo Cu-Au deposit

The first stage of Au mineralisation is associated with the main ore-bearing hydrothermal fluids which precipitated chalcopyrite, pyrrhotite and pyrite. Sulphide-hosted Au is a combination of nano-inclusion Au and solid-solution lattice-bound Au.

The second stage of Au mineralisation is associated with Bi-rich hydrothermal fluids, within micro-vein networks cross-cutting the named ore lodes. Bi-associated Au is primarily lattice-bound, precipitating in solid-solution with Bi.

'Visible' Au for both Au stages developed within the Kanmantoo Cu-Au deposit as the solubility limits of host minerals were reached, or as Au nanoparticles were destabilised by later localised hydrothermal or metamorphic heating. 'Visible' Au was distributed

heterogeneously across the named ore lodes, showing systematic relationships with Ag, Bi and Hg.

5.7 Sources of Au mineralisation

Various sources of mineralisation have been proposed for the Kanmantoo Cu-Au deposit. Schiller (2000) suggests meta-dolerite dykes and sills as sources of heat and metals. Others (Arbon, 2011, Foden, 2006) suggest Co-enriched ore-bearing fluids released from a crystallising magma, overprinting existing lithologies – however this interpretation is limited in other research.

Oliver et al. (1998) observed an abundance of Fe-minerals transgressive to bedding, inferring an association between Cu mineralisation and Fe-rich metasomatism – which suggests the injection of high temperature Fe-rich fluids during D3 deformation. LA-ICP-MS data does not recognise such an association; it instead supports Lyons (2012), who observed no Cu:Fe relationship but noted high Fe in unaltered GABS – indicating Cu-rich fluid interaction with an Fe-rich sediment.

Many authors (Arbon, 2011, Fleming and White, 1984, Foden et al., 2006, Kimpton, 2018, Lyons, 2012, Oliver et al., 1998, Wilson, 2009) have suggested an igneous fluid source, supported by observations of Cu-bearing K-feldspar veins, whole rock geochemistry and geochemical similarities with known regional intrusives (i.e. the Monarto and Mannum granites).

Using field observations and anomalous $\delta^{18}\text{O}$ and $\delta^{34}\text{S}$ ratios, Oliver et al. (1998) infers metamorphism is higher-grade relative to surrounds. As no significant east-west major or trace element patterns are observed, a thermally-anomalous deep convective heat source (an intrusive granitic pluton) is suggested for the main ore-bearing hydrothermal fluids, mixing with regional metamorphic fluids (Sandiford et al., 1995, Schiller, 2000). Local reactivation

of east-dipping compressional faults, caused by extensional reactivation of D3 compressional shears, are a likely pathway for regional mineralising fluids, with D3 axial planes acting as conduits and traps (Wilson 2009, Lyons 2011). Variation observed in major and trace elements reflects changing input from this proposed hydrothermal fluid source.

A post-peak metamorphic event within the history of the Kanmantoo Cu-Au deposit – such as the introduction of retrograde Bi-rich hydrothermal fluids from post-Delamarian orogeny fault reactivation – may have promoted minor movement of nanoparticle Au to 'visible' Au, as observed in sample MB15. It is proposed that this retrograde and relatively low-temperature event is related to an external heat and fluid source – such as a magmatic pluton. This provided the energy to partly recrystallise some stage 1 Au nano-inclusions and solid-state Au contained in the Au-bearing sulphides, as well as the observed stage 2 Bi associated Au (Oliver et al., 1998).

5.8 Timing of mineralisation

Although still a topic of debate, a significant proportion of recent research supports a late-peak to post-peak metamorphic timing for mineralisation, associated with the cessation of the Delamarian Orogeny (Foden et al., 2006, Lyons, 2012, Kimpton, 2018, Wilson, 2009). The Delamarian Orogeny was relatively short-lived, with contractional onset estimated at 514 ± 4 Ma, terminating abruptly at $\sim 490 \pm 3$ Ma (Foden et al. 2006).

Using monazite U-Pb dating of felsic veins within the Kanmantoo Cu-Au deposit, Kimpton (2018) determined peak metamorphism at 495.11 ± 2.79 Ma, correlating with Wilson's (2009) suggested ages for peak metamorphism (492 ± 9 Ma). Although Au-hosted veins have not been specifically dated, the distribution of nanoparticle Au throughout the sample suite provides evidence that these ages are representative of 'stage 1' sulphide hosted Au.

Kimpton (2018) measures ages for post-peak metamorphism at 483.43 ± 2.52 Ma. Using U-Th-Pb dating, Focke (2010) gives ages of 469 ± 17 Ma for the Nugent/O'Neil ore lode. As mentioned in 5.2, these samples are representative of later felsic/SV veining and associated alteration. It is inferred that retrograde hydrothermal alteration fluid was introduced between 483.43 Ma and 469 Ma – resulting in stage 2 Bi-associated Au, with possible minor recrystallisation of stage 1 nano-inclusions or solid solution Au.

CONCLUSIONS

Four textural settings of Au are observed within the Kanmantoo Cu-Au deposit: sulphide-hosted Au, Au intergrown with Bi, 'free' Au, and nanoparticle Au. Two stages of Au development within the Kanmantoo Cu-Au deposit are proposed:

- Stage 1: sulphide-hosted Au within chalcopyrite, introduced with primary ore-bearing fluids
- Stage 2: Bi-associated Au, introduced with retrograde low temperature Bi-bearing fluids

There is no single cause for the pattern and distribution of Au within the Kanmantoo Cu-Au deposit. The variation in Au, Cu, Bi and other major and trace elements observed in the named ore lodes reflects input from a changing magmatic hydrothermal fluid source alongside multiple fluid veins and pathways.

The known characteristics of Au at the Kanmantoo Cu-Au deposit can be utilised as an exploration pathfinder in other exploration tenements within the Adelaide fold belt.

Because Au is observed primarily as Au nanoparticles with rare 'nuggetty' occurrences of 'visible' Au, changing current ore processing procedures to recover more Au could negatively

affect Cu recovery. As such, it is recommended that existing processing techniques continue to be employed.

FUTURE WORK

- Sulphur isotopes – comparison with Lyons (2012) and other regional deposits to further constrain deposit paragenesis.
- Further investigation of the identified Au:Bi link to determine the extent of this relationship and how it can be successfully applied to exploration techniques.
- ‘Invisible Au’ nano-inclusions (~5-10 nm) are observable using high-quality machinery (Palenik et al., 2004). Studies suggest temperature versus particle size stability diagrams are a reasonable proxy for estimating maximum host rock temperature (Reich et al., 2006). Future studies could aim to image the nano-inclusions to further constrain the geological conditions of Au formation.

ACKNOWLEDGMENTS

Many thanks to my supervisor Dr Richard Lilly and colleague Benjamin Kimpton, thank you for being a positive sounding board for both good and bad ideas, your assistance and personal support throughout the year.

Thanks to the University of Adelaide and Adelaide Microscopy for access to facilities, analytical equipment and essential training, particularly Dr Sarah Gilbrt for invaluable guidance during data processing and interpretation.

Funding, background knowledge and logistical support for this project has been provided by Hillgrove Resources Limited– significantly Peter Rolley and Hayden Arbon – many thanks for scientific insights, working alongside such a dedicated and passionate team has been

invaluable. Furthermore, a special thanks is extended to Hillgrove Resources for providing financial support in this Honours year.

REFERENCES

- ARBON, H. (2011). *Bismuth distribution in the Cu-Au mineralisation of the Kanmantoo deposit, South Australia*. (Honours thesis), The University of Adelaide
- BELPERIO A. P., P. W. V., FAIRCLOUGH M. C., GATEHOUSE C. G., GUM J., HOUGH J., BURTT A. (1998). Tectonic and metallogenic framework of the Cambrian Stansbury Basin – Kanmantoo Trough, South Australia. *AGSO Journal of Australian Geology & Geophysics*, 17, 183-200.
- BOTH, R. A. (2005). *The Kanmantoo-Strathalbyn mineral field, South Australia: the 'Cornwall of the Colony'* 1-20.
- CHANG, Z., LARGE, R. R., & MASLENNIKOV, V. (2008). Sulfur isotopes in sediment-hosted orogenic gold deposits: Evidence for an early timing and a seawater sulfur source. *Geology*, 36(12), 971-974.
- CIOBANU, C., COOK, N., Utsunomiya, S., Pring, A., & Green, L. (2011). Focussed ion beam–transmission electron microscopy applications in ore mineralogy: Bridging micro-and nanoscale observations. *Ore Geology Reviews*, 42(1), 6-31.
- COOK, N. J., & CHRYSOULIS, S. L. (1990). Concentrations of invisible gold in the common sulfides. *The Canadian Mineralogist*, 28(1), 1-16.
- COOK, N. J., CIOBANU, C. L., MERIA, D., SILCOCK, D., & WADE, B. (2013). Arsenopyrite-Pyrite Association in an Orogenic Gold Ore: Tracing Mineralization History from Textures and Trace Elements. *Economic Geology*, 108(6), 1273-1283. doi: 10.2113/econgeo.108.6.1273
- FOCKE, D (2010). *Geological mapping and the variation of mineralising conditions at the Kanmantoo Cu-Au deposit and its satellites, South Australia*. (Phd Thesis) Technische Universität Bergakademie Freiberg Institut für Mineralogie Bereich Lagerstättenforschung und Petrologie.
- FLEET, M. E., CHRYSOULIS, S. L., MACLEAN, P. J., DAVIDSON, R., & WEISNER, C. G. (1993). Arsenian pyrite from gold deposits; Au and As distribution investigated by SIMS and EMP, and color staining and surface oxidation by XPS and LIMS. *The Canadian Mineralogist*, 31(1), 1-17.
- FLEMING, P., & WHITE, A. (1984). Relationships between deformation and partial melting in the Palmer migmatites, South Australia. *Australian Journal of Earth Sciences*, 31(4), 351-360.
- FLÖTTMANN, T., HAINES, P., JAGO, J., JAMES, P., BELPERIO, A., & GUM, J. (1998). Formation and reactivation of the Cambrian Kanmantoo Trough, SE Australia: implications for early Palaeozoic tectonics at eastern Gondwana's plate margin. *Journal of the Geological Society*, 155(3), 525-539. doi: 10.1144/gsjgs.155.3.0525
- FLÖTTMANN, T., JAMES, P., ROGERS, J., & JOHNSON, T. (1994). Early Palaeozoic foreland thrusting and basin reactivation at the Palaeo-Pacific margin of the southeastern Australian Precambrian Craton: a reappraisal of the structural evolution of the Southern Adelaide Fold-Thrust Belt. *Tectonophysics*, 234(1-2), 95-116.
- FODEN, J., SONG, S. H., TURNER, S., ELBURG, M., SMITH, P. B., VAN DER STELDT, B., & VAN PENGLIS, D. (2002). Geochemical evolution of lithospheric mantle beneath S.E. South Australia. *Chemical Geology*, 182 (2-4), 663-695. doi: 10.1016/S0009-2541(01)00347-3
- FODEN, J., ELBURG, M. A., DOUGHERTY-PAGE, J., & BURTT, A. (2006). The timing and duration of the Delamerian Orogeny: correlation with the Ross Orogen and implications for Gondwana assembly. *The Journal of Geology*, 114(2), 189-210.
- FODEN, J., ELBURG, M. A., TURNER, S., SANDIFORD, M., O'CALLAGHAN, J., & MITCHELL, S. (2002). Granite production in the Delamerian orogen, South Australia. *Journal of the Geological Society*, 159(5), 557-575.
- GEORGE, L. L., COOK, N. J., CROWE, B. B., & CIOBANU, C. L. (2018). Trace elements in hydrothermal chalcopyrite. *Mineralogical Magazine*, 82(1), 59-88.
- GROVES, D., & BAKER, W. (1971). The cobalt and nickel content of some sulphides from ore deposits in eastern Tasmania: Tech. Rep. Dep. Mines Tasm. 14: 27-35.
- GROVES, D. I., & SANTOSH, M. (2015). Province-scale commonalities of some world-class gold deposits: implications for mineral exploration. *Geoscience frontiers*, 6(3), 389-399.
- GUM, J. (1998). *The sedimentology, sequence stratigraphy and mineralisation of the silverton subgroup, South Australia*. University of South Australia

- HAINES, P. W. J., J.B GUM, J.C. (2001). Turbidite deposition in the Cambrian Kanmantoo Group, South Australia. *Australian Journal of Earth Sciences*, 48(3), 465-478. doi: <https://doi.org/10.1046/j.1440-0952.2001.00872.x>
- HEWETT, J. (2017). *Gold distribution and the relationship to pyrite trace element geochemistry at the Ernest Henry deposit, Queensland* (Honours Thesis), The University of Adelaide
- HITZMAN, M. W., BOOKSTROM, A. A., SLACK, J. F., & ZIENTEK, M. L. (2017). Cobalt—Styles of Deposits and the Search for Primary Deposits: US Geological Survey.
- JAGO, J. B., GUM, J. C., BURTT, A. C., & HAINES, P. W. (2003). Stratigraphy of the Kanmantoo Group: A critical element of the Adelaide Fold Belt and the Palaeo-Pacific plate margin, Eastern Gondwana. *Australian Journal of Earth Sciences*, 50(3), 343-363. doi: 10.1046/j.1440-0952.2003.00997.x
- KIMPTON, B (2018) *The geological relationship between the Kanmantoo Cu-Au deposit mineralisation metasomatism and igneous intrusives* (Honours thesis), the University of Adelaide.
- LYONS, N. (2012). *Evidence for magmatic hydrothermal mineralisation at Kanmantoo Copper deposit, South Australia*. (Honours thesis), the University of Adelaide
- MAO, J., LI, Y., GOLDFARB, R., HE, Y., & ZAW, K. (2003). Fluid inclusion and noble gas studies of the Dongping gold deposit, Hebei Province, China: a mantle connection for mineralization? *Economic Geology*, 98(3), 517-534.
- MARTÍNEZ-ABAD, I., CEPEDAL, A., & FUERTES-FUENTE, M. (2013). Gold scavenged by Bi-melts indicated by the late low salinity aqueous fluid inclusions of the Castro de Rei skarn (Lugo, Spain).
- MOATS, M. S., & DAVENPORT, W. G. (2014). Chapter 2.2 - Nickel and Cobalt Production. In S. Seetharaman (Ed.), *Treatise on Process Metallurgy* (pp. 625-669). Boston: Elsevier.
- OLIVER, N., DIPPLE, G., CARTWRIGHT, I., & SCHILLER, J. (1998). Fluid flow and metasomatism in the genesis of the amphibolites-facies, pelite-hosted Kanmantoo copper deposit, South Australia. *American Journal of Science*, 298(3), 181-218.
- PALENIK, C. S., UTSUNOMIYA, S., REICH, M., KESLER, S. E., WANG, L., & EWING, R. C. (2004). “Invisible” gold revealed: Direct imaging of gold nanoparticles in a Carlin-type deposit. *American Mineralogist*, 89(10), 1359-1366. doi: 10.2138/am-2004-1002
- PARKER, A. (1986). Tectonic development and metallogeny of the Kanmantoo Trough in South Australia. *Ore Geology Reviews*, 1(2-4), 203-212.
- POLLOCK, M., G.SPRY, P., A.TOTT, K., KOENIG, A., A.BOTH, R., & OGIERMAND, J. (2018). The origin of the sediment-hosted Kanmantoo Cu-Au deposit, South Australia: Mineralogical considerations. *Ore Geology Reviews*, 95, 94-117.
- PREISS, W. V. (2000). The Adelaide Geosyncline of South Australia and its significance in Neoproterozoic continental reconstruction. *Precambrian Research*, 100(1-3), 21-63. doi: [https://doi.org/10.1016/S0301-9268\(99\)00068-6](https://doi.org/10.1016/S0301-9268(99)00068-6)
- ROLLEY, P & WRIGHT, M (2017). Kanmantoo copper deposits. Australian ore deposits: Monograph (32), 667-670.
- REICH, M., KESLER, S. E., UTSUNOMIYA, S., PALENIK, C. S., CHRYSOULIS, S. L., & EWING, R. C. (2005). Solubility of gold in arsenian pyrite. *Geochimica et Cosmochimica Acta*, 69(11), 2781-2796.
- REICH, M., UTSUNOMIYA, S., KESLER, S. E., WANG, L., EWING, R. C., & BECKER, U. (2006). Thermal behavior of metal nanoparticles in geologic materials. *Geology*, 34(12), 1033-1036. doi: 10.1130/G22829A.1
- SANDIFORD, M., ERASER, G., ARNOLD, J., FODEN, J., & FARROW, T. (1995). Some causes and consequences of high-temperature, low-pressure metamorphism in the eastern Mt Lofty Ranges, South Australia. *Australian Journal of Earth Sciences*, 42(3), 233-240.
- SCHILLER, J. C. (2000). *Structural geology, metamorphism and origin of the Kanmantoo Copper deposit, South Australia*/by Jeffrey Christopher Schiller.
- SCHWARTZ, M. (2000). *Cadmium in Zinc Deposits: Economic Geology of a Polluting Element* (Vol. 42).
- SECCOMBE, P., SPRY, P., BOTH, R., JONES, M., & SCHILLER, J. (1985). Base metal mineralization in the Kanmantoo Group, South Australia; a regional sulfur isotope study. *Economic Geology*, 80(7), 1824-1841.
- SIMON, G., KESLER, S. E., ESSENE, E. J., & CHRYSOULIS, S. L. (2000). Gold in Porphyry Copper Deposits: Experimental Determination of the Distribution of Gold in the Cu-Fe-S System at 400° to 700°C. *Economic Geology*, 95(2), 259-270. doi: 10.2113/gsecongeo.95.2.259
- STANDING, J (2005) Structural controls on copper mineralisation at the Kanmantoo project, S.A (independent technical report). Adelaide: Fluid Focus Pty. Ltd
- STANDING, J (2006) Structural controls on copper mineralisation at the Kanmantoo project, S.A (independent technical report). Adelaide: Jigsaw Geoscience Pty. Ltd.
- STARLING, A., GILLIGAN, J., CARTER, A., FOSTER, R., & SAUNDERS, R. (1989). High-temperature hydrothermal precipitation of precious metals on the surface of pyrite. *Nature*, 340(6231), 298.

- SPRY, P.G (1976) *Base Metal mineralisation in the Kanmantoo group*, S.A: South Hill, Bremer and Wheel Ellen areas (Honours thesis). University of Adelaide, Australia.
- TEDESCO, A. (2009). Late-stage orogenic model for Cu-Au mineralisation at Kanmantoo mine: New insights from titanium in quartz geothermometry, fluid inclusions and geochemical modelling(Honours thesis) University of Adelaide. Australia
- TOOTH, B. (2013). *The hydrothermal chemistry of Bismuth and the liquid Bismuth collector model*. (Phd Thesis)
- TOOTH, B., BRUGGER, J., CIOBANU, C., & LIU, W. (2008). Modeling of gold scavenging by bismuth melts coexisting with hydrothermal fluids. *Geology*, 36(10), 815-818.
- TOOTH, B., CIOBANU, C. L., GREEN, L., O'NEILL, B., & BRUGGER, J. (2011). Bi-melt formation and gold scavenging from hydrothermal fluids: An experimental study. *Geochimica et Cosmochimica Acta*, 75(19), 5423-5443.
- TOTTEFF, S. (1999). Cambrian sediment-hosted exhalative base metal mineralisation, Kanmantoo Trough, South Australia. *Geological Survey.*, 57.
- WILSON, G.L (2009) *Structural setting and timing of the Kanmantoo Cu-Au deposit, Callington, SA* (Honours thesis). University of Adelaide, Australia.
- VIKENTYEV, I., & VIKENTYEVA, O. (2015). *Precious metal minerals and “invisible” gold in sulfide ores of Urals*. Paper presented at the Proc. XII Int. sci. conf.«Advanced technologies, equipment and analytical systems for materials and nano-materials». Ust-Kamenogorsk: East-Kazakhstan State Tech. Uni.

APPENDIX

APPENDIX A1 – DIAMOND DRILL CORE SAMPLE LIST

APPENDIX A2- GRAB SAMPLES AND SECONDARY SAMPLES LIST

APPENDIX A3 – DRILL CORE IMAGES

APPENDIX A4 – THIN SECTION APPENDIX

APPENDIX B1 – GOLDSNIFFER REPORT

APPENDIX B2 – GOLDSNIFFER DETECTED AU LOCATIONS

APPENDIX C1 - 2 BI AND S SPECTRA (TOP) COMPARED TO BI, S, CU, FE AND AU SPECTRA (BOTTOM).

APPENDIX C2 - SPECTRAL MATCH ANALYSIS)

APPENDIX C3 - FEI QUANTA 600 MLA SCANNING ELECTRON MICROSCOPE RESULTS EXAMPLE

APPENDIX D1 – SEM IMAGERY – BI

APPENDIX D2 – SEM IMAGERY – OTHER TRACE ELEMENTS

APPENDIX E1 – LASER DATA SUMMARY

APPENDIX E2 – GRAB TO CON LA-ICP-MS DATA

APPENDIX E3 - LA-ICP-MS ASSAY RESULT TERNARY DIAGRAMS

APPENDIX E4- LA-ICP-MS ELEMENTAL PLOTS

APPENDIX E5 – AU RASTER MAP LOCATION

APPENDIX F1 - KANMANTOO ASSAY DATA DECEMBER 2014- JULY 2018

APPENDIX G1 – LA-ICP-MS AU














Appendix A1 – Diamond drill core sample list




sample number	sample length (cm)	hole number	tray number	tray interval	Au interval	zone	sample type	Au ppm	Cu %	other comments
MB01	11.9	KTDD 160	T60	328.77 - 334.32	330-331	Central Kavangah	diamond drill core sample	4.33	3.9336	chalcopyrite/ pyrrhotite vein
MB02	11.1	KTDD 173		123.6-129.6	124-125	West Kavangah	diamond drill core sample	0.53	0.8026	si chlorite altered relic gabs unit
MB03	16	KTDD 071	T47	477.70-483.68	479-480	West Kavangah	diamond drill core sample	1.31	4.6875	gabs unit with chalcopyrite veining
MB04	7	KTDD 118	T29	168-174.05	173-174	West Kavangah	diamond drill core sample	0.53	3.5727	quartz unit with associated sulphur veining
MB05	9	KTDD 118	T29	168-174.05	173-174	West Kavangah	diamond drill core sample	0.53	3.5727	sulphide with chalcopyrite, pyrrhotite veining
MB06	7	KTDD 043	T15	78.6-84.7	82-83	Spitfire	diamond drill core sample	1.09	0.6557	highly weathered sulphide
MB07	6	KTDD 043	T15	78.6-84.7	82-83	Spitfire	diamond drill core sample	1.09	0.6557	highly weathered sulphide
MB08	8	KTDD 160	T61	334.82 - 340.88	335-336	East Kavanagh	diamond drill core sample	4.33	3.9336	gabs boundary
MB09	12	KTDD 156	T36	176.45-182.19	176-177	Spitfire	diamond drill core sample	2.32	7.9897	xrf shows au and mo. massive sulphide with heavily mineralised veins
MB10	15	KTDD 156	T36	176.45-182.19	177-178	Spitfire	diamond drill core sample	2.04	10.6257	massive sulphide with heavily mineralised veins
MB11	12	KTDD 005	T15	no tray tag	139-140	West Kavangah	diamond drill core sample	0.74	0.1228	quartz/ sulphide contact
MB12	12	KTDD 007	T13	116.3-122.3	117-118	West Kavangah	diamond drill core sample	1.33	5.6012	weathered deformed gabs unit
MB13	6	KTDD 004	T09	137.4 - 143.3	138-139	Nugent	diamond drill core sample	3.55	0.0658	poor core quality. Sulphur weathered altered gabs

Appendix A2- Grab samples and secondary samples list


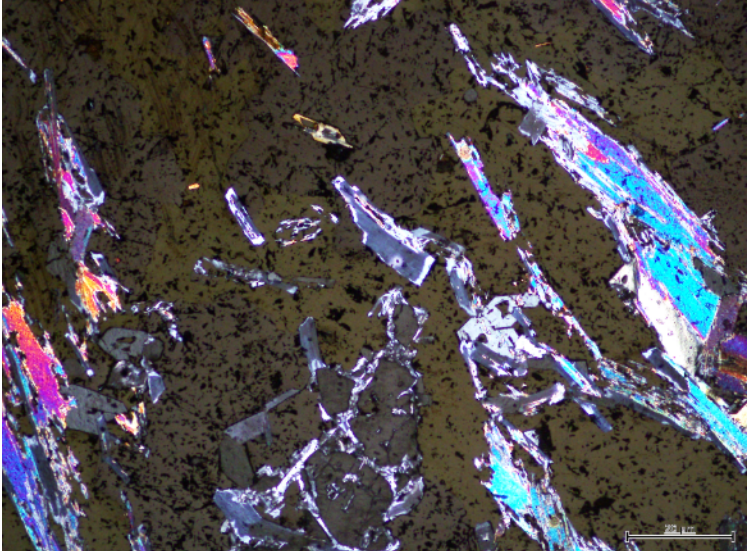
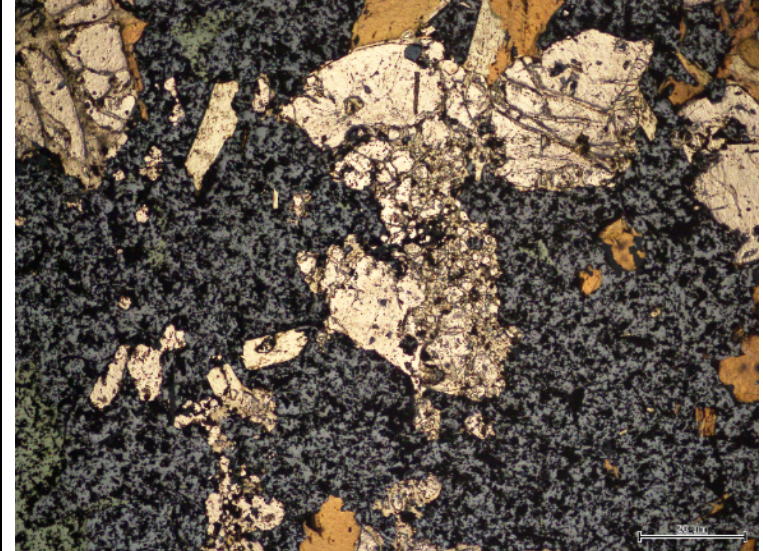
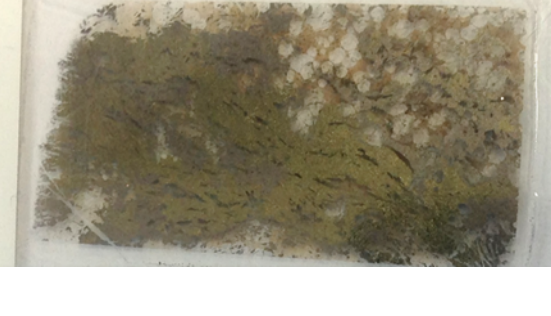
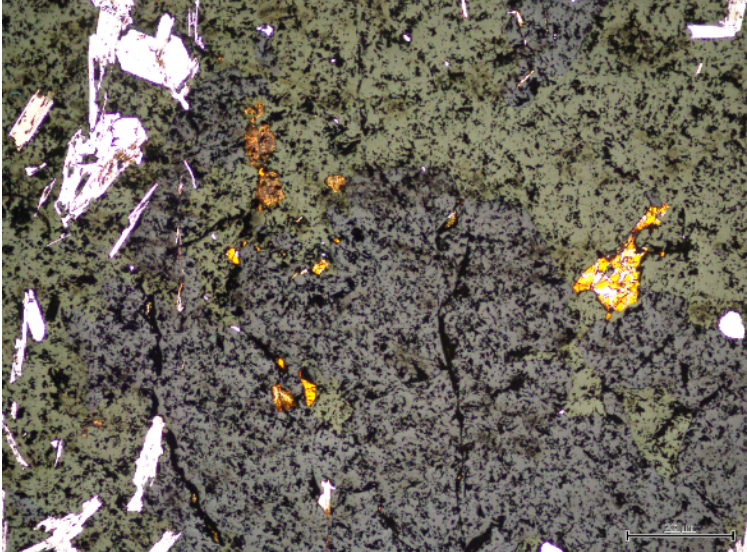

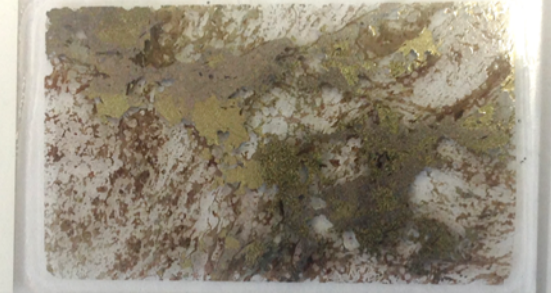
pit grab samples	sample location	zone	XRF field testing Au ppm	sample type	other comments
MB14 (sample 1)	S corner of shot 1028_037	Spitfire	9.4	blasted pit rock	au in chalcopyrite
MB15 (sample 2)	NE corner of shot 1028_037	Spitfire	29.29 in chalc 8.65 in pyrite	blasted pit rock	au in chalcopyrite and pyrite
MB16 (sample 3)	NE corner of shot 1028_037	Spitfire	3.21	blasted pit rock	au in silicacious foliated matrix
MB17 (sample 4)	NE corner of shot 1028_037	Spitfire	19.7 - 7.08	blasted pit rock	au in chalcopyrite with small garnet inclusions
MB18 (sample 5)	NE corner of shot 1028_037	Spitfire	15.08	blasted pit rock	au in chalcopyrite vein
mill samples	sample number	zone	Au ppm	sample type	other comments
TT40	TT40A	Spitfire	3.94 G/T	concentrate	tailings from Knelson concentrator
	TT40B	Spitfire	3.94 G/T	concentrate	tailings from Knelson concentrator
TC300	TC300A	Spitfire	300 G/T	concentrate	gold concentrate from gravity table
	TC300B	Spitfire	300 G/T	concentrate	gold concentrate from gravity table
	TC300C	Spitfire	300 G/T	concentrate	gold concentrate from gravity table
Focke Samples	Sample number	zone	Hole Number	Interval	other comments
c58 'sample 12'	c58.1	Nugent	KTDD141	75.5m	quartz-rich sample with sulphide veining
	c58.2	Nugent	KTDD141	75.5m	quartz-rich sample with sulphide veining
Late Sulphides	Sample number	Zone	Other comments		
BK25	BK25a	east haul road	J2 vein orientation		
	BK25b	east haul road	J2 vein orientation		

Appendix A3 - Drill Core images

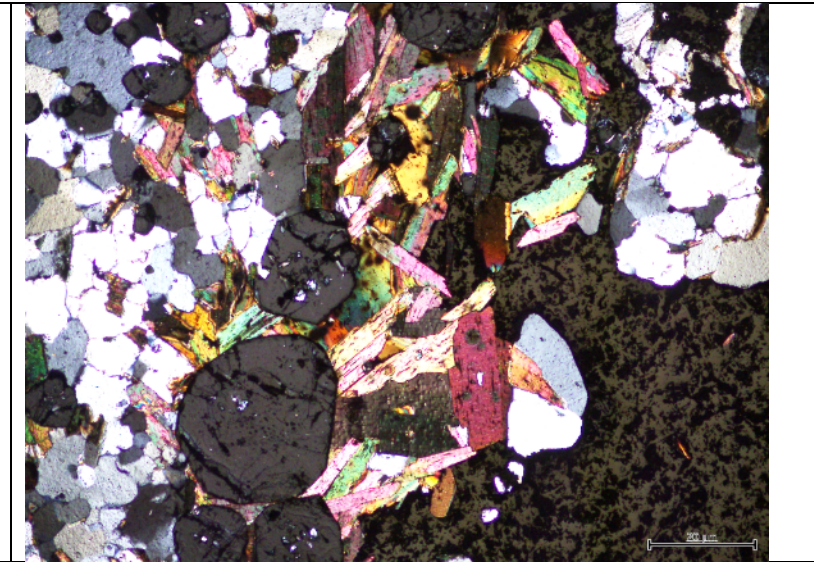
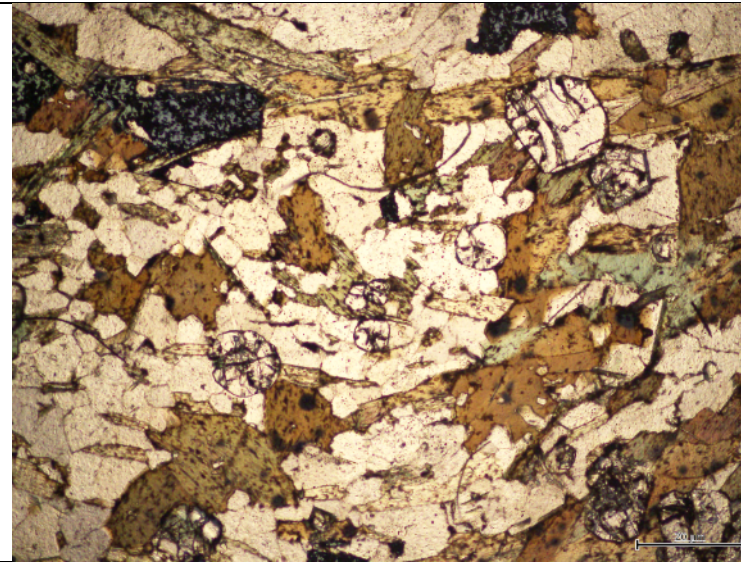
sample number	Reference image	
MB01		
MB03		
MB04		
MB05 MB06		
MB07		
MB08		
MB09		

<p>MB10</p>		
<p>MB11</p>		
<p>MB12</p>		
<p>MB13</p>		
<p>MB14 (sample 1) MB15 (sample 2)</p>		
<p>MB16 (sample 3) MB17 (Sample 4)</p>		
<p>MB18 (sample 5) C58</p>		

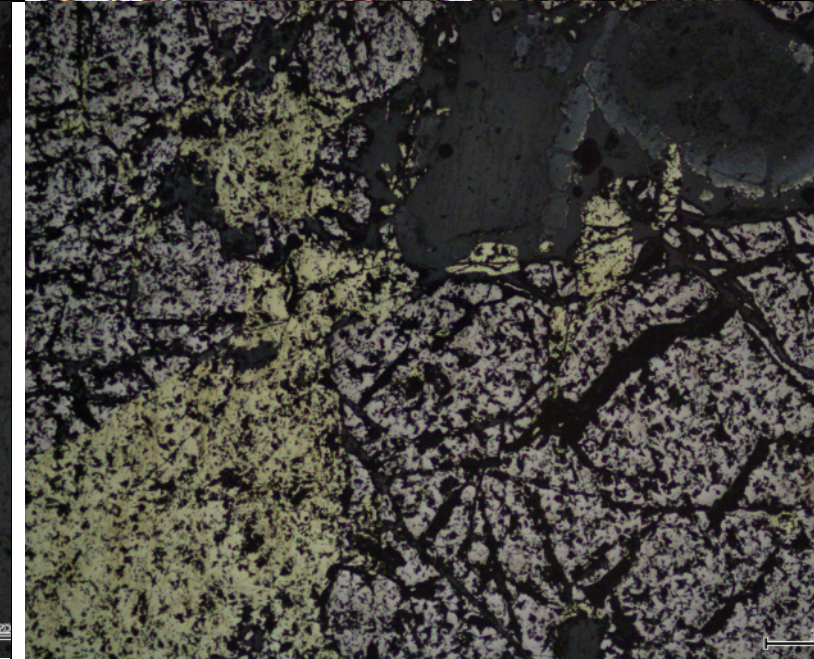
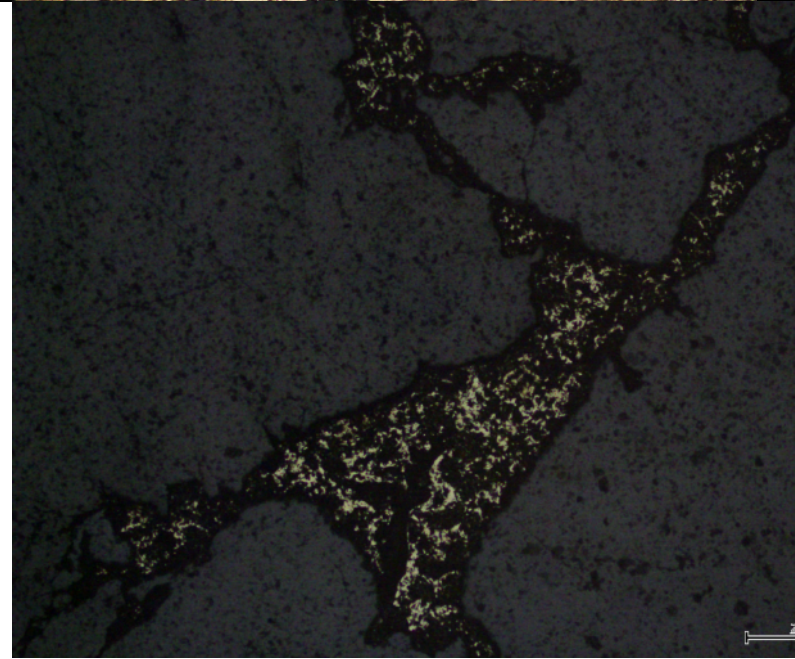
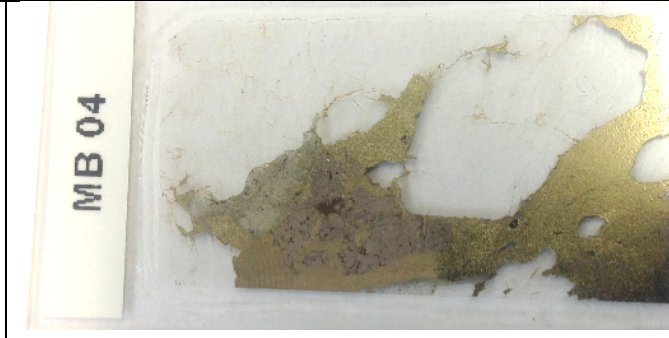
Appendix A4 – Thin section appendix

drill hole samples	prepared thin section	SEM mapping	condition	thin section	thin section image	
MB01 East K	MB01	Completed	unbroken			
				<p>Host garnet and fibrous micas (biotite/ chlorite) – some schistosity . well formed quartz grains in some places Garnets often rimmed by micas. Quite broken up. 2 stages of biotite – oriented vs unoriented ‘stringer’ grains. Infil Chalcopyrite veining with intergrowth of pyrotite (possible pyrite swaths within other sulphides) host rock inclusions within the sulphides. Chalcopyrite more dominant sulphide Glassy inclusions. Low relief low birefringence mineral within sulphides – golden under ppl – Ilmionite staining Relic quartz host –schistose – pale micas see 12.2 intrusive vein Minor sphalerite 40% sulphides 34% garnets 25% micas 1% quartz</p>		
	MB01.2	completed	Unbroken			
				<p>See MB01. Streaky texture along sulphides parallel to long edge of grain – thin section issue Garnets cracked and infilled Significant alteration halos within micas Quartz seen in mb01 and mb01.2 significantly different to other samples, sharp contacts well formed grains, not showing significant ‘patchwork’ extinction . very minor stage Chalc – pyrotite boundary sometimes well defined sometimes more mixed</p>		
MB02	Not chosen for thin section					
MB03 West K	MB03	completed	unbroken			

Garnet biotite quartz schist with sulphide infill veining
 Garnet- well defined but cracked grains, some show chlorite rimming some don't
 Fine quartz grains with clear undulose extinction. Makes up most of the matrix – more siliceous host rock ?
 Biotite w. chlorite. Elongate grains
 Sulphides – chalcopyrite and pyrotite overprinting host rock, loose vein network, unsure if following schistosity (subparallel?)
30% sulphides 15% GARNET 25% quartz 30% micas



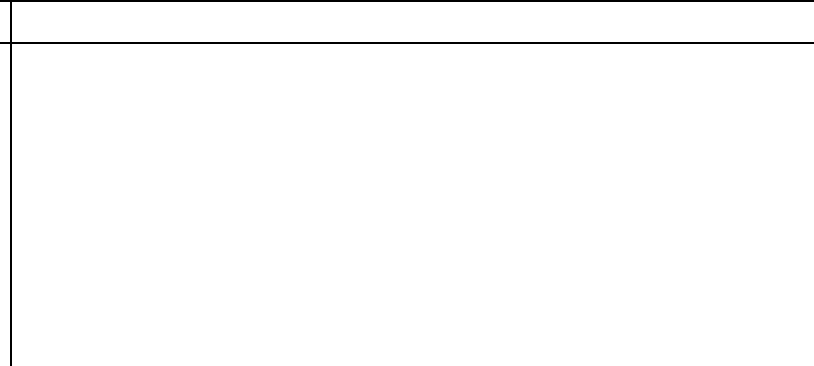
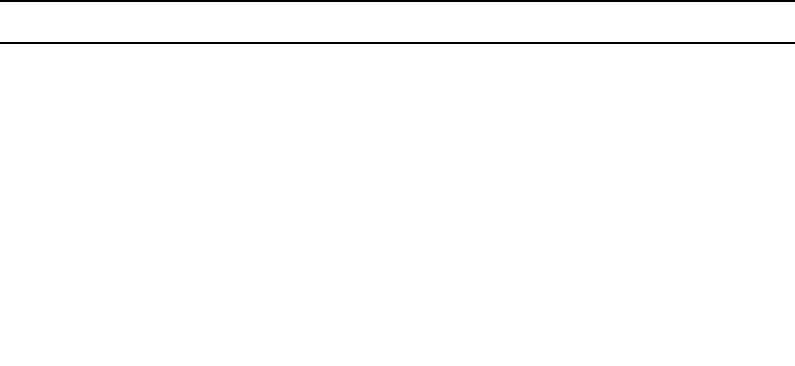
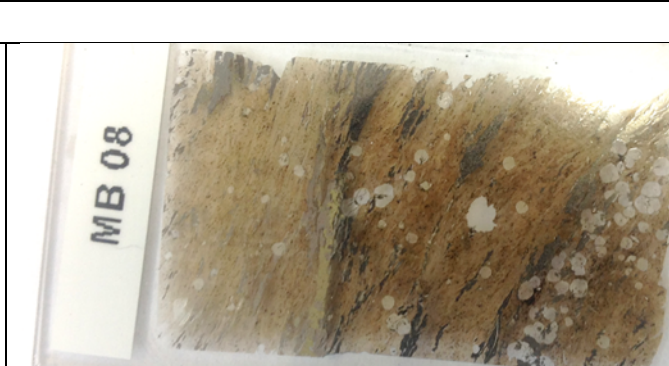
MB04 West K	MB04	complete d	unbroke n
----------------	------	---------------	--------------



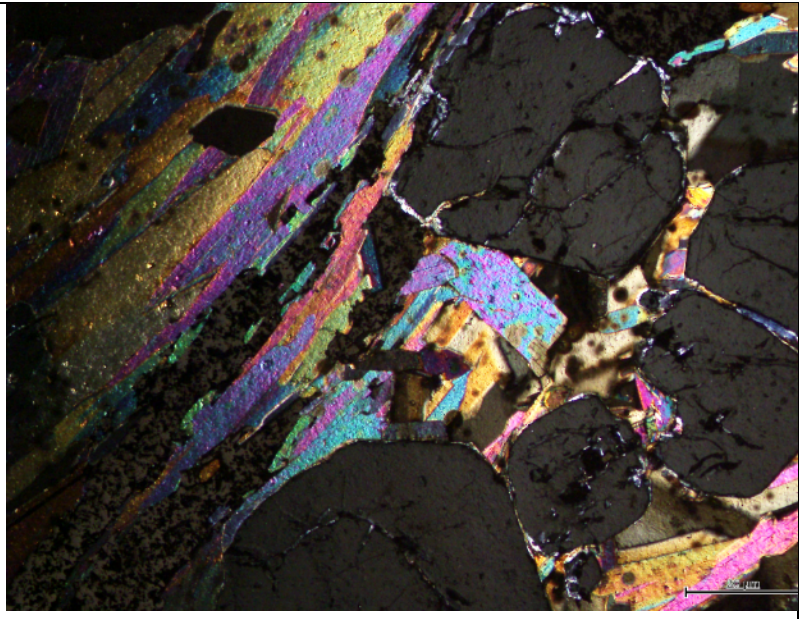
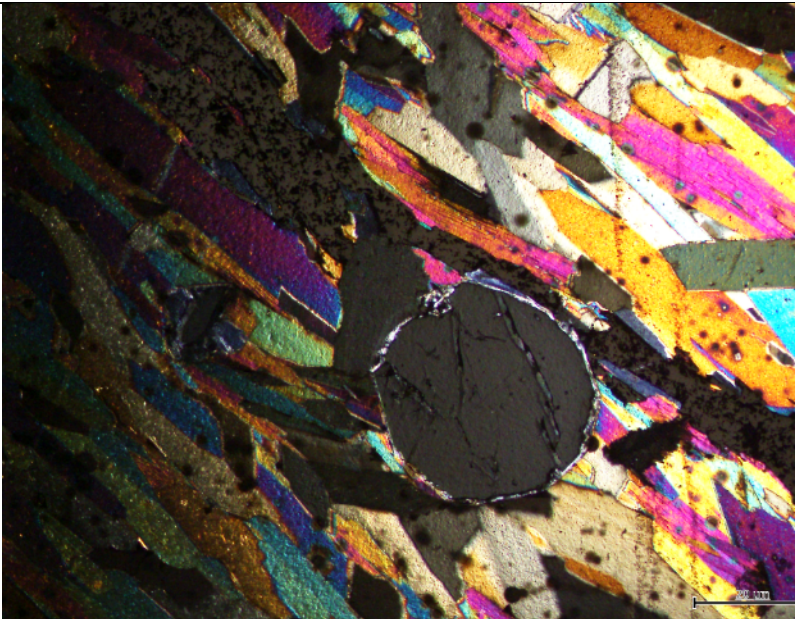
Course grained quartz dominated unit with sulfur veining
 Chalcopyrite more abundant than pyrrhotite. P inside c but not vice versa. Within fractures/ stringers cutting through host . Significant iron oxide weathering – limonite infill texture
 Quartz- not a lot of alteration or infill. Relatively clean contact . fluid inclusions
 Micaceous veining - late Chlorite alteration darker green than previous samples? Not traditional pale grassy green. Fibrous vein infill, filling space between sulphides and quartz, not birefringent – really pale chlorite? Immature fluid inclusion containing garnets and ghost staurolite and biotite – representing original but very altered host rock
57% quartz 25% chalco 15% pyrrhotite 2% chlorite 1% garnet biotite staurolite

MB05	Not chosen for thin section		
MB06	Not chosen for thin section		
MB07	Not chosen for thin section		

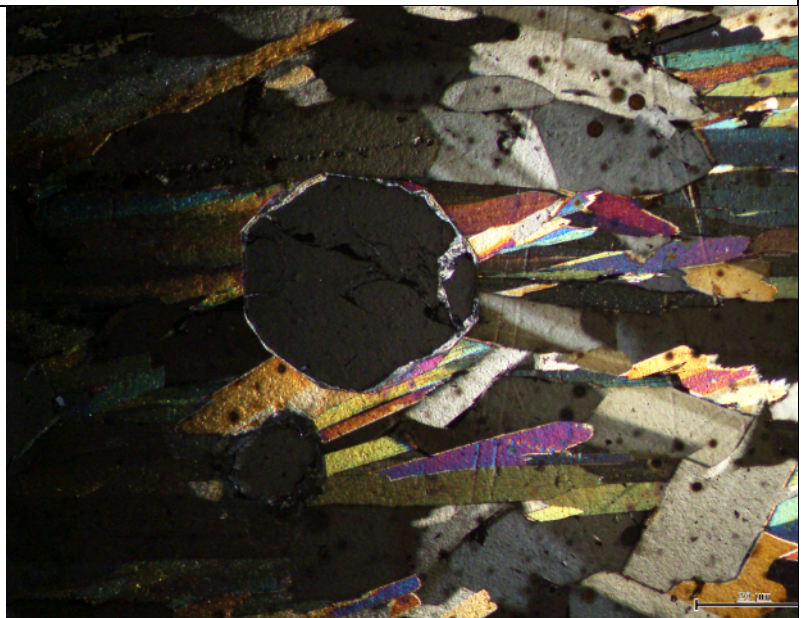
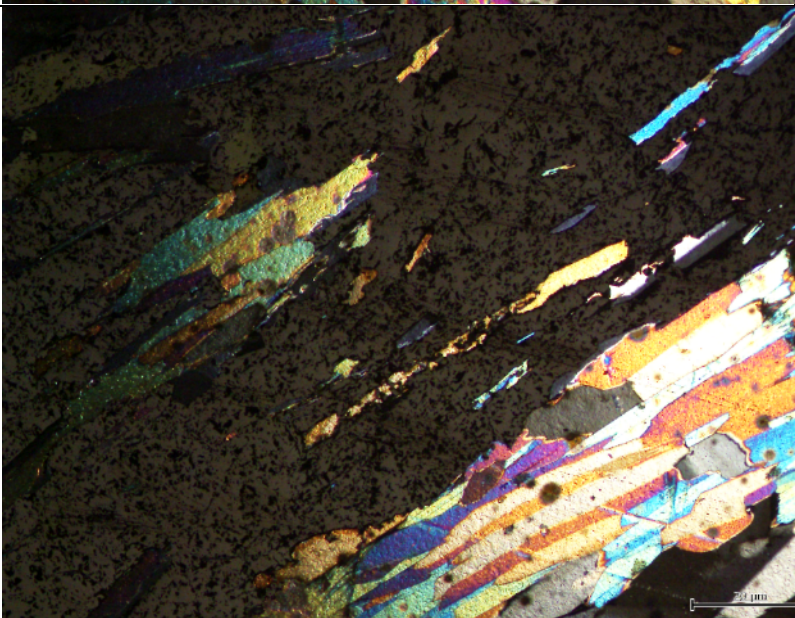
MB08 East K	MB08	complete d	unbroke n
----------------	------	---------------	--------------



Biotite chlorite schist (BGCS)
 What does varying relief within the same mineral indicate? Compositional variation?
 Easy to see variation within layers (can see in thin section)
 Garnet dominated vs bitote dominant layers. Boundaries between chalco and phytrotite less distinguishable. More pyrottite than chalco. Biotite defining foliation – significant radiation halos. Well formed elongate grains
 Garnet rimmed by late chlorite. Later stage infil micas not following foliation
 Glassy inclusions Magnetite everywhere?
 Order = Biotite and quartz 2. Garnet 3. Sulphidies 4. retrograde biotite and chlorite



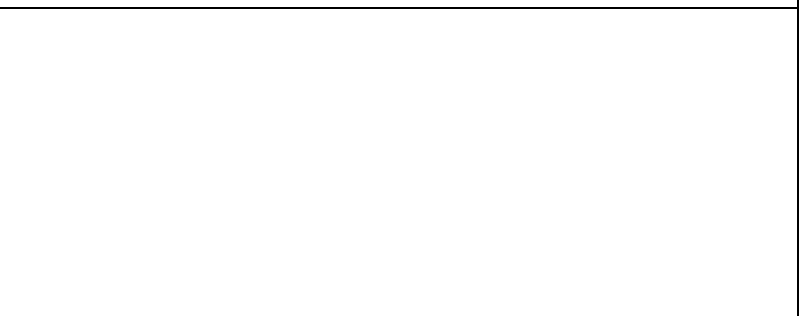
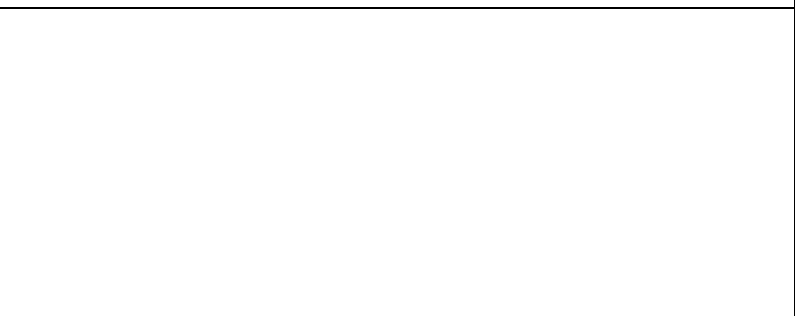
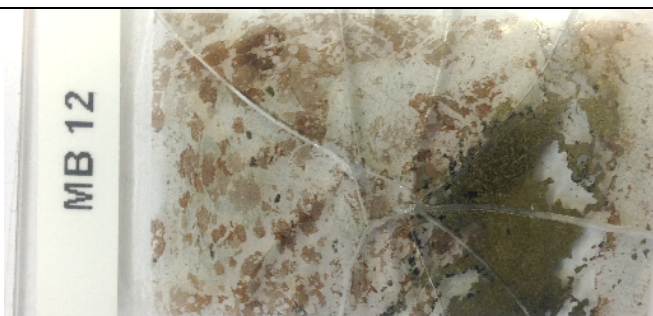
MB08.2	complete	unbroken
--------	----------	----------



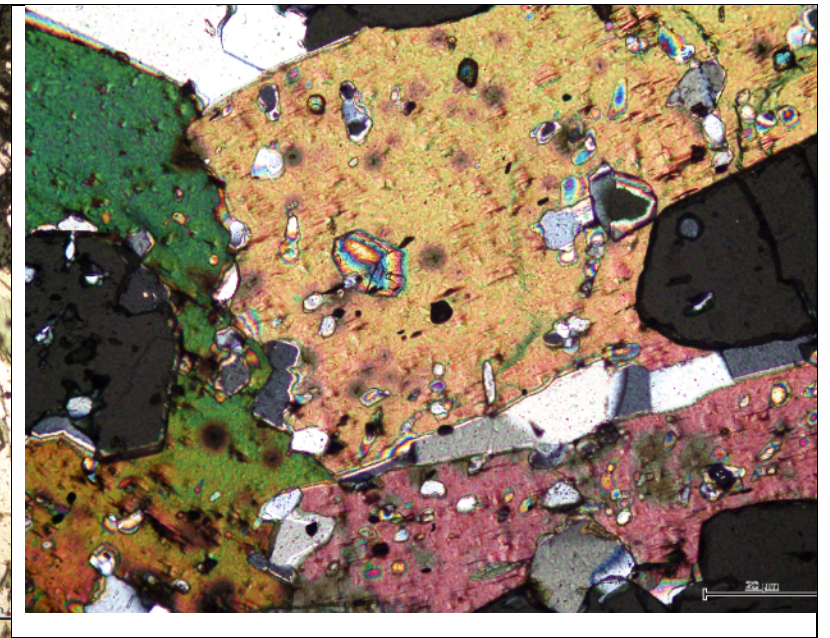
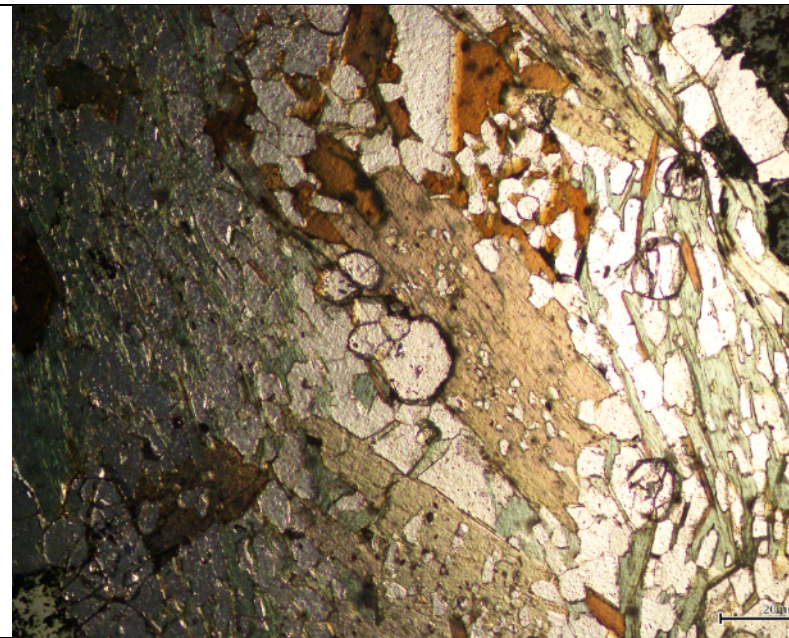
See MB08. Very scratched thin section. Garnet crystals might be late overgrowth? Not deformed and cross cut schistosity
50% micas 20% garnet 20% quartz 10% sulphides

MB09	Not chosen for thin section	
MB10	Not chosen for thin section	
MB11	Not chosen for thin section	

MB12 West K	MB12	broken
----------------	------	--------



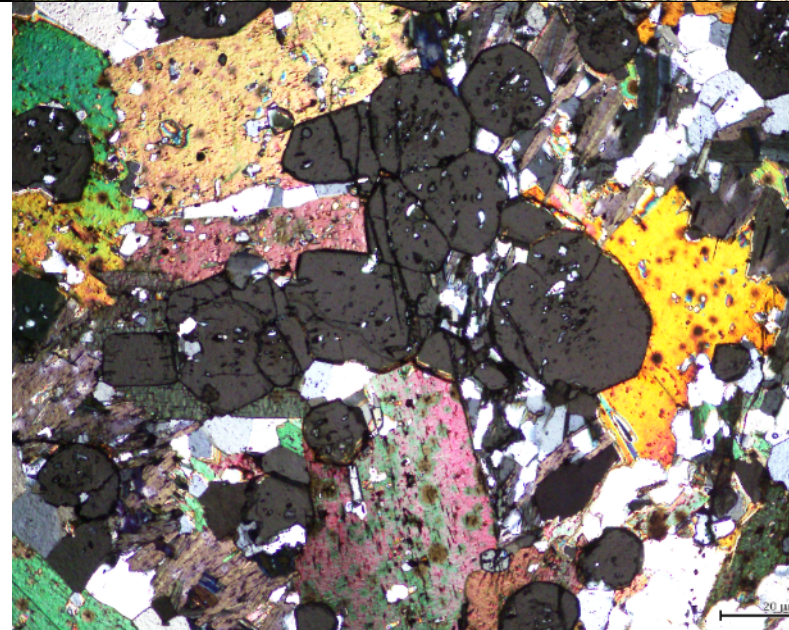
See MB12.2



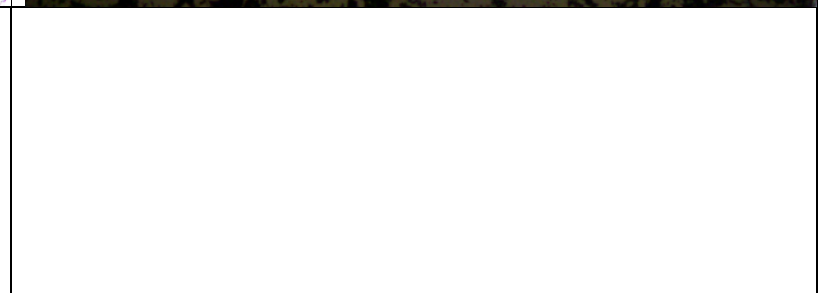
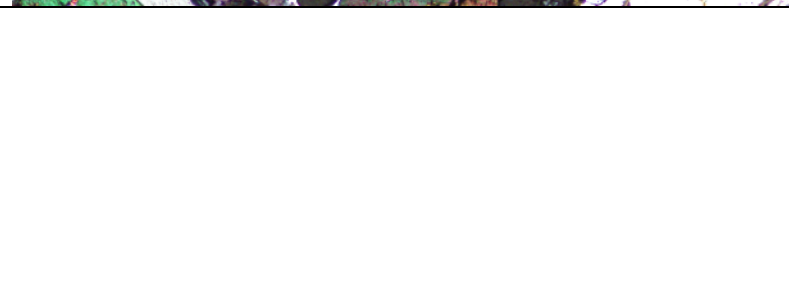
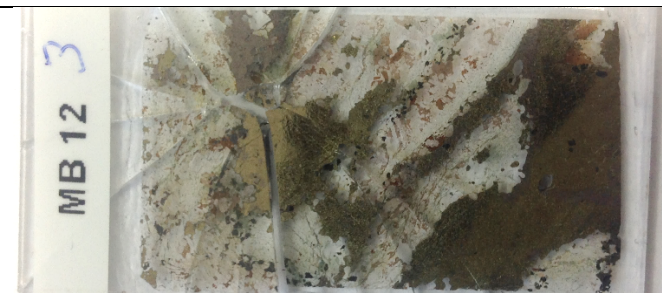
MB12.2	complete	unbroken
--------	----------	----------



(QMS) Weathered deformed Garnet Biotite Quartz host rock with irregular sulphide veining. Beautiful perfect square pyrite grain. Good candidate for laser ablation mapping. Significant chlorite and chlorite alteration. Radiation halos seen in micas and staurolite. Inclusions of something super birefringent in the biotite. Magnetite everywhere but not sure how it fits into the story. Complicated relationships. No clear pervasive foliation or schistosity. Quartz inclusions within other minerals – deformation of siliceous host rock?. Quartz quite fine grained- intergrowth with garnet?

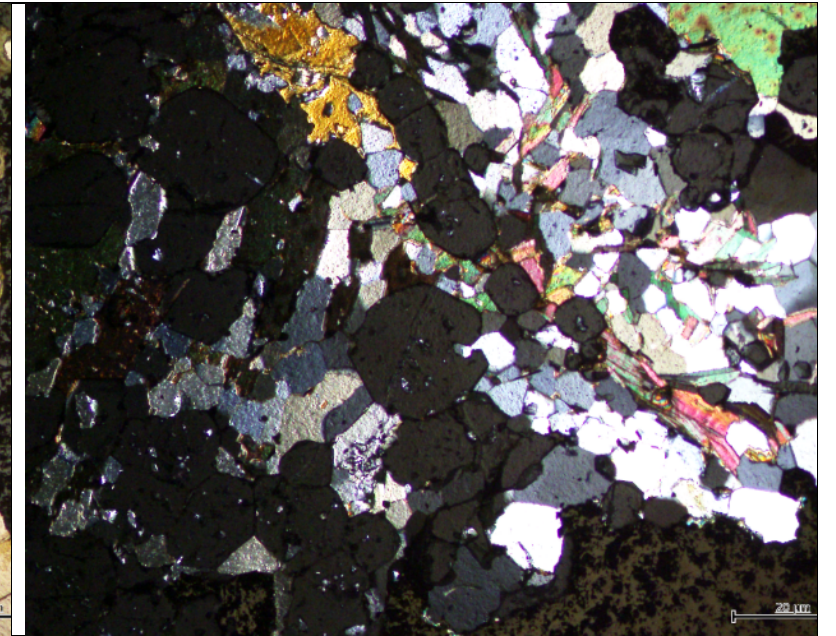
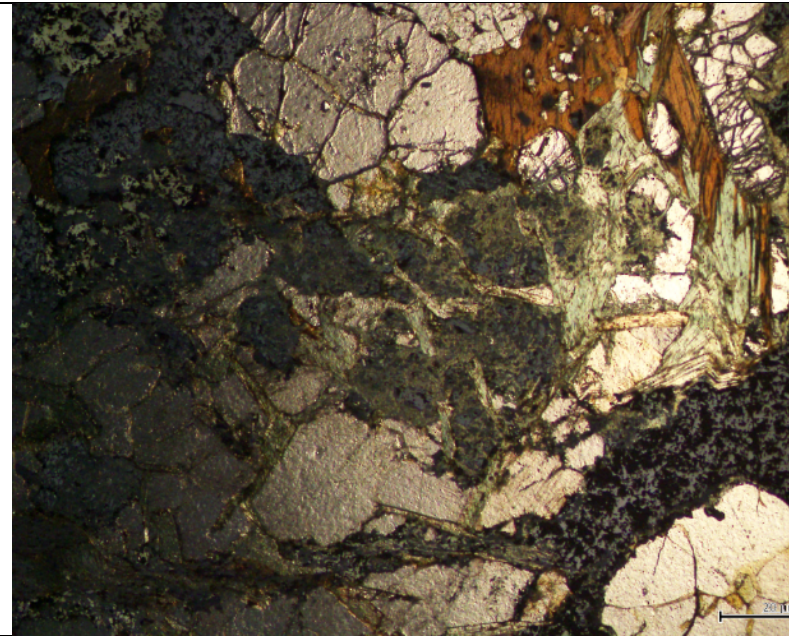


MB12.3		broken
--------	--	--------



See MB12.2 (QMS)
 Garnet higher relief than other samples
 Fine grained quartz (25 microns) with some larger grains (100 microns)
 Larger mica swaths – less fibrous – more well formed grains – more porous. Space available during formation?
 Fluid inclusions withn garnet

20% micas 25% quartz 25% garnet 30% sulphides

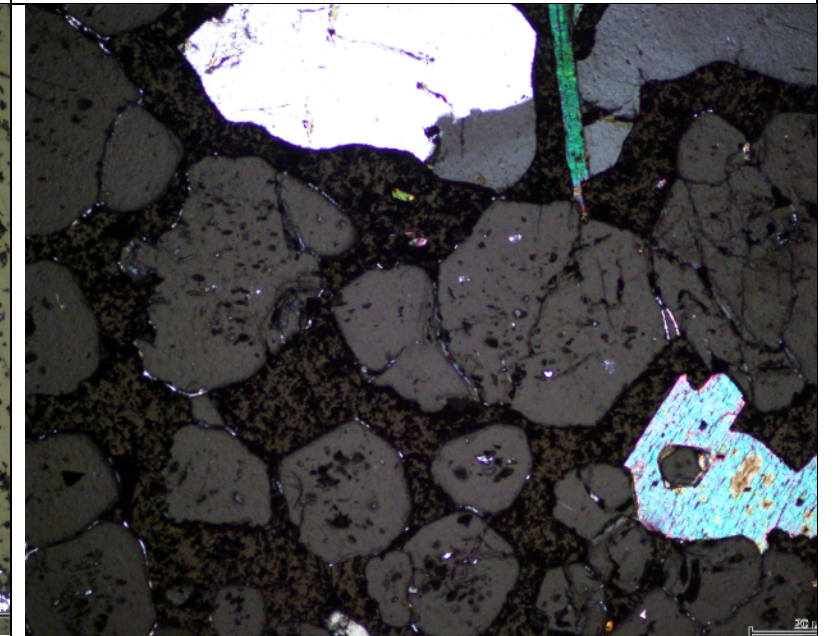
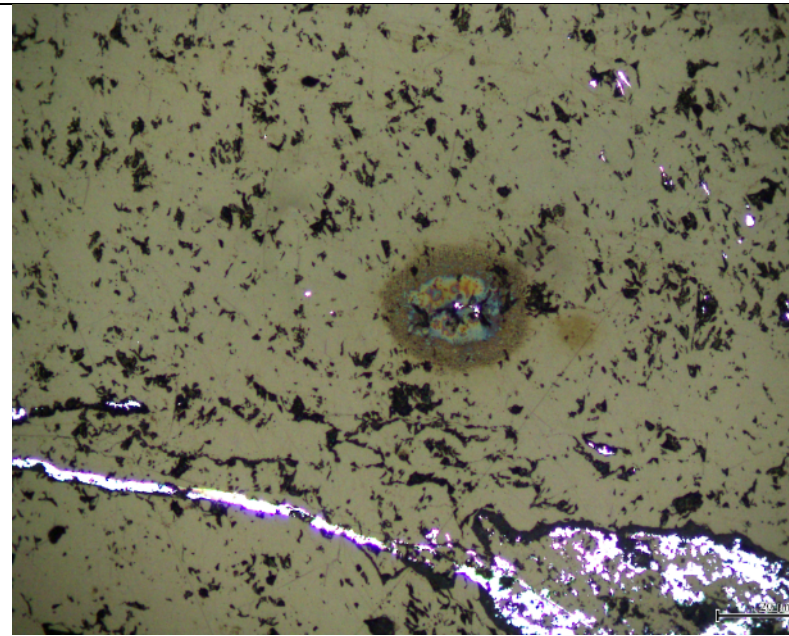
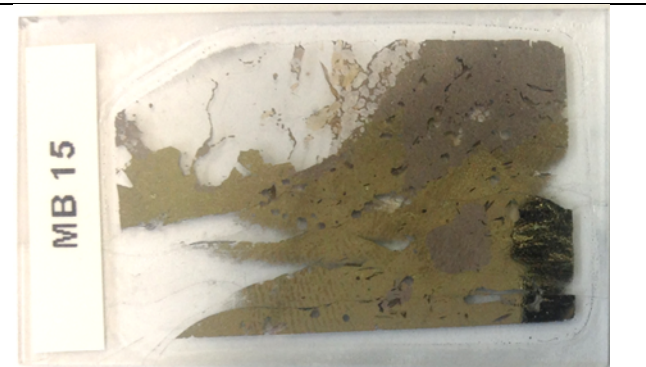


MB13 Not chosen for thin section

Grab-samples

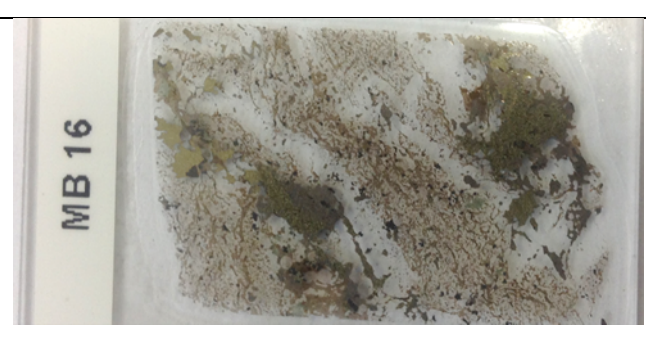
MB14 Not chosen for thin section

MB15 Spitty	MB15	complete d	unbroken
-------------	------	------------	----------

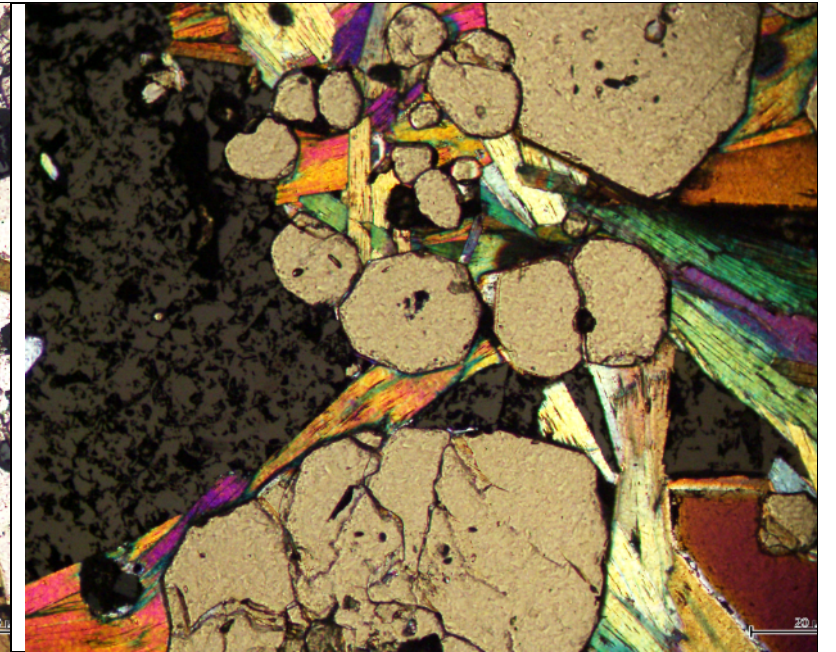
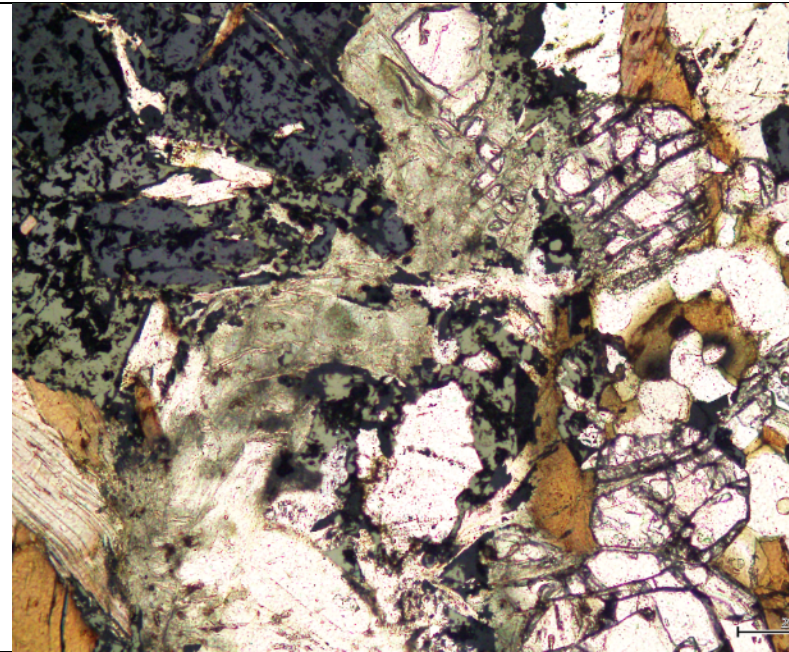


Massive Chalcopyrite with pyrotite with quartz and mica/ garnet matrix host
 Thin thin section, lots of very bright sections where the thin section is just blank
 Highly birefringent radiation halos
 Garnet with ample sulphide and mica inclusions, some chlorite rimming
 Biotite and chlorite unoriented – later stage? Chl alteration of bi
 Royal blue mineral inside quartz> clear ppl – fluid inclusions within quartz?
 Streaky sulphides – thin section issues. Minor staurolite
 Pyrotite rimming host rock with chalcopyrite surrounding – timing?

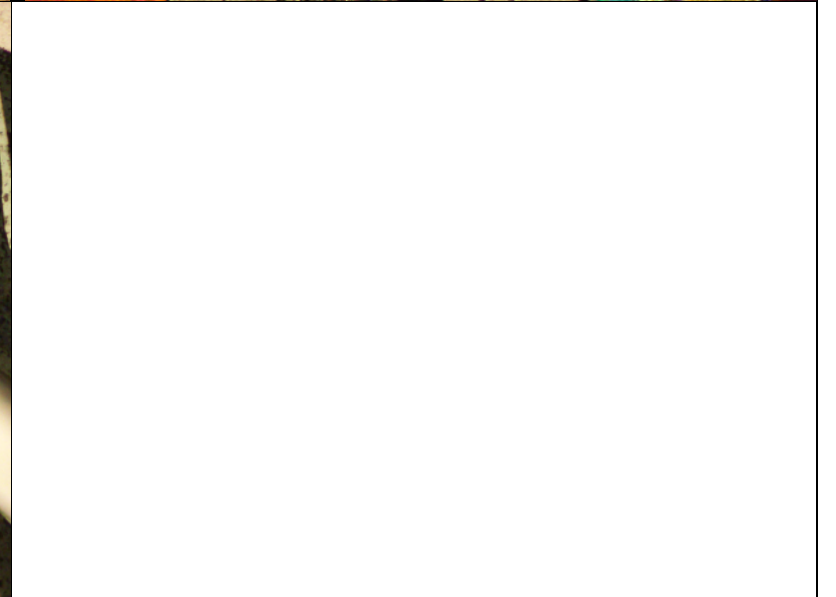
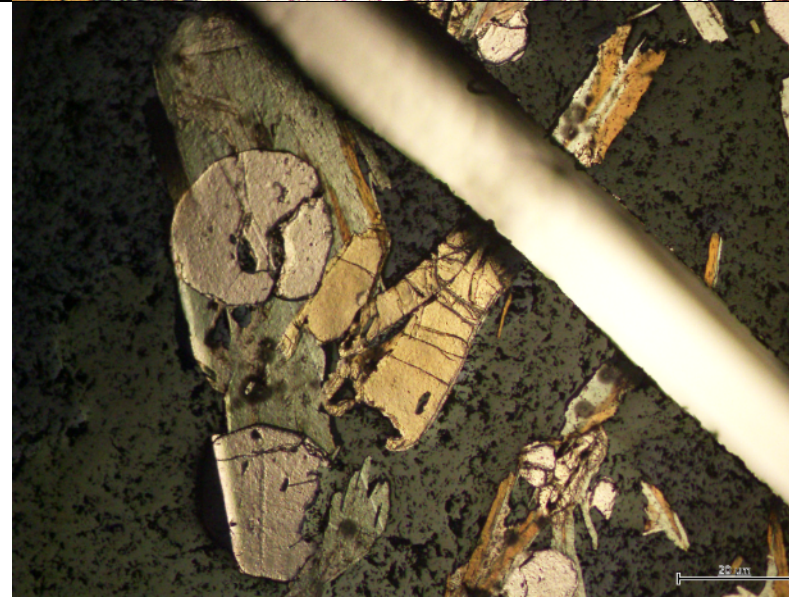
MB16 Spitty	MB16	complete d	unbroken
-------------	------	------------	----------



biotite garnet schist with quartz veining and irregular sulphides
 chalcopyrite – intergrowth with pyrotite - infill textures – massive – scattered magnetite. Minor stage
 biotite – elongate grains – not quite fibrous – intergrowth with chlorite, significant variations in grain size
 – seen as inclusions within garnets and sulphides – not as many radiation halos as seen in other samples –
 compositional variation?
 Chlorite 2 stages – elongate – some larger ‘massive swaths’ – inclusions within garnet and sulphides –
 chlorite alteration,, later fibrous infill stage
 Zonation of garnets – ie more pink in centre, well rounded inclusion rich grains, some chlorite rimming
 Quartz- 2 distinct grain sizes, larger swaths representing later quartz veining
 Slightly different to earlier samples = variation between lodes



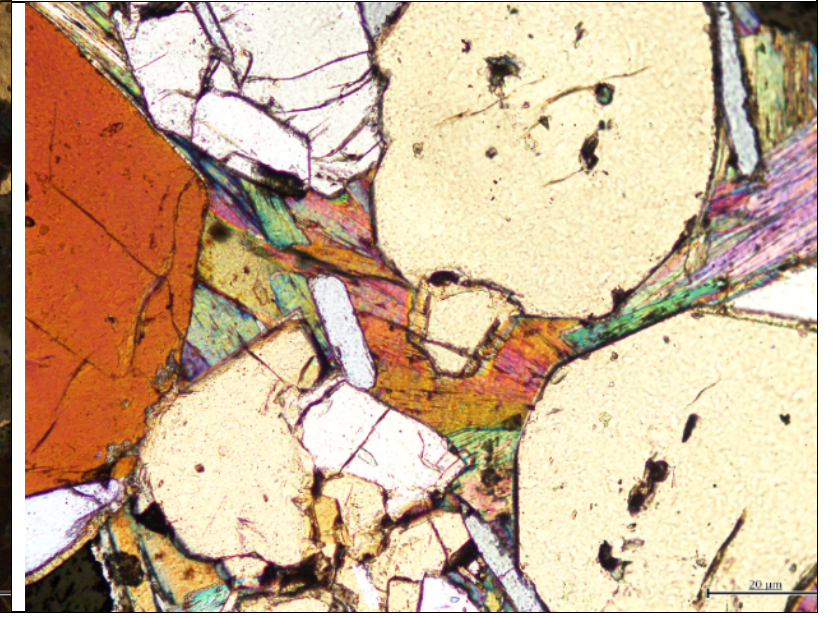
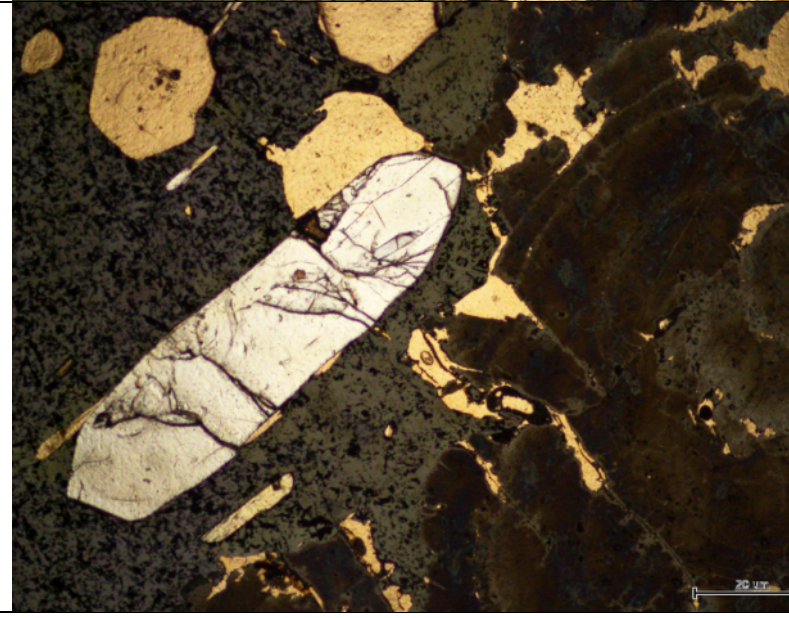
MB17	MB17		broken
------	------	--	--------





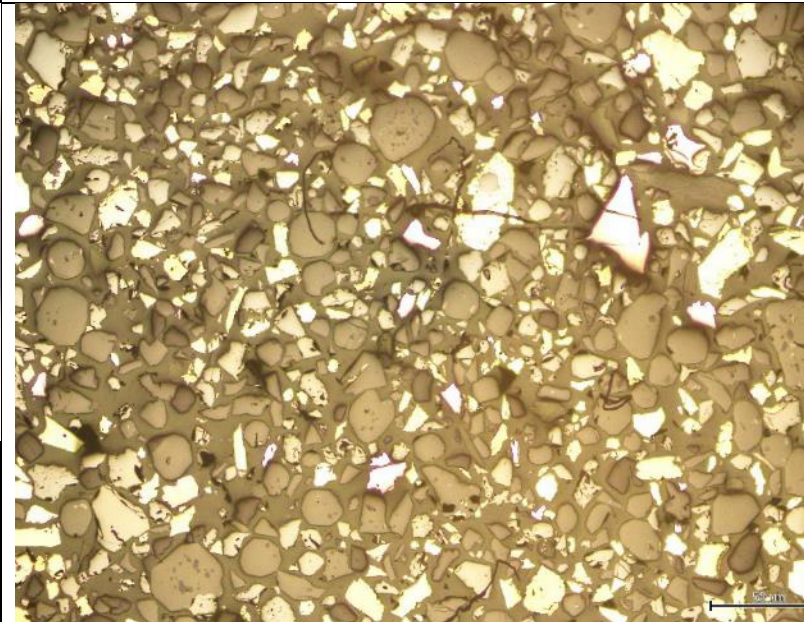

MB17	MB17	Not undertaken	Unbroken (remade)
------	------	----------------	-------------------

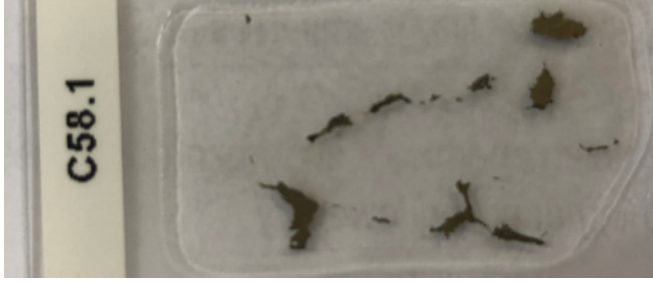
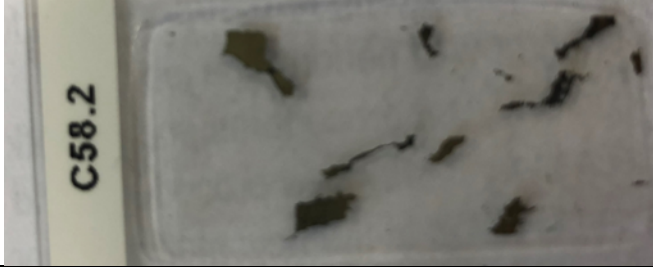


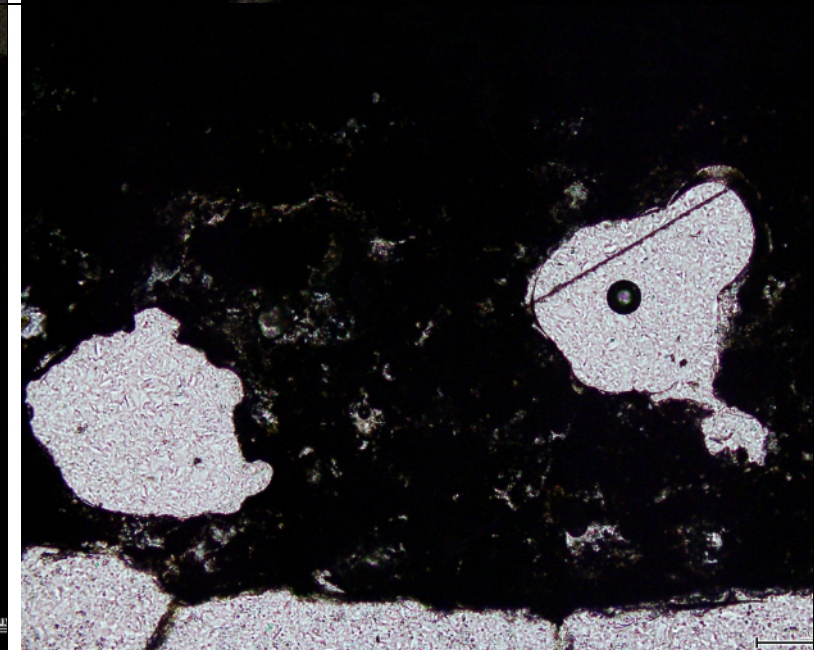
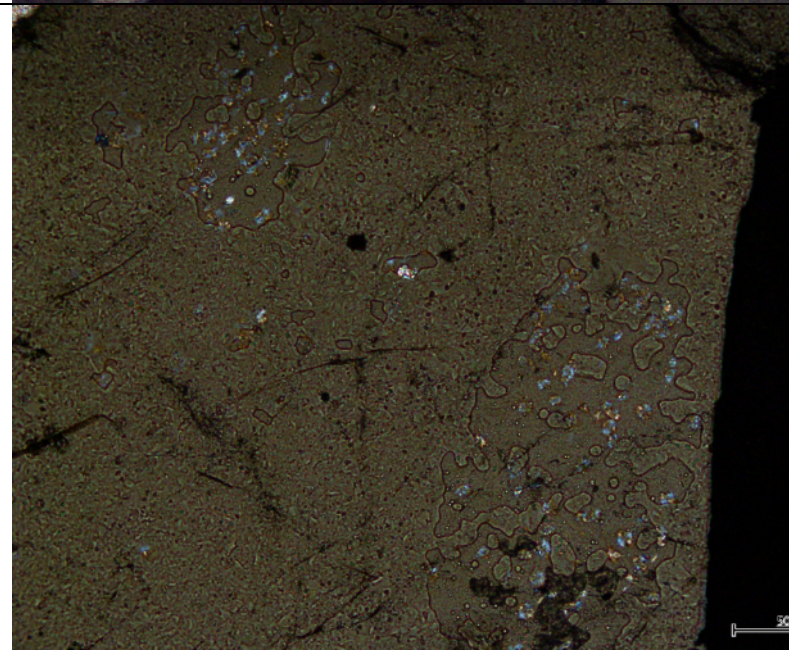
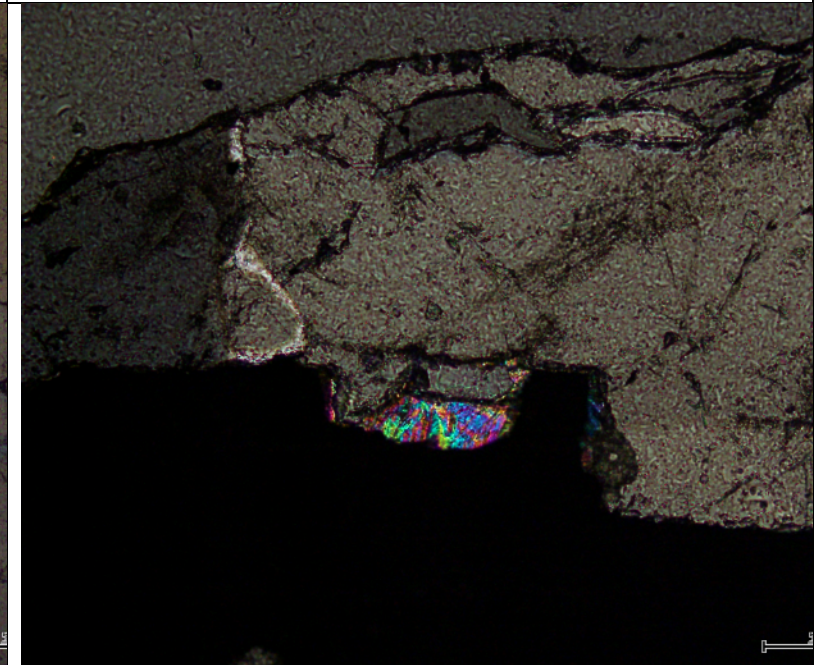
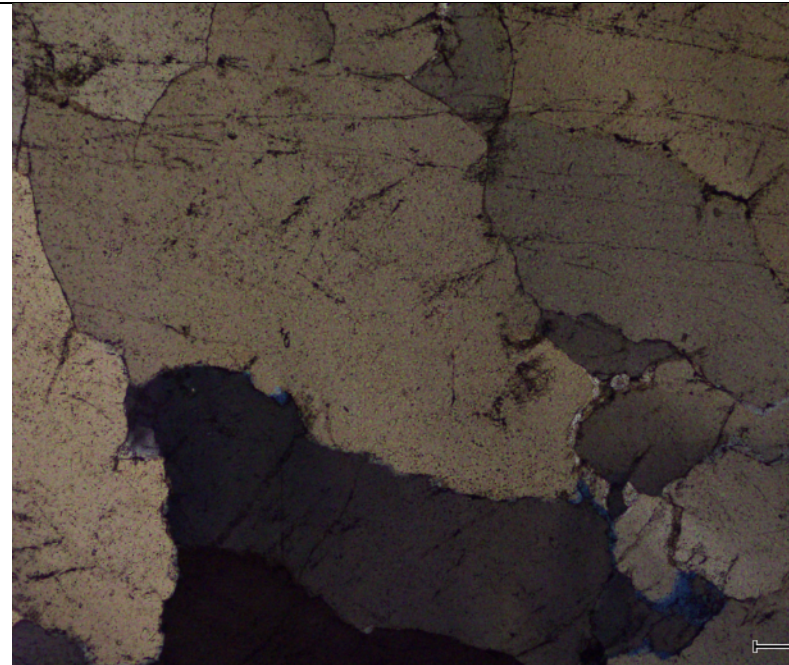
sulphides with coarse grained quartz biotite garnet host rock
 Broken thin section hard to really define relationships
 Chalcopyrite and pyrotite make up most of the slide – massive, garnet – well formed but less pervasive than previous samples
 Clear boundaries between the sulphide stages- Glassy inclusions - Chlorite alteration of biotite
 Staurolite – elongate grains – not fibrous (see image)



Pyrite ? muddy brown wavy extinction – isotropic (see image) Course grained quartz -Limonite fracturing					
MB18	Not chosen for thin section				
Concentrate samples					
Tt40	Tt40a	Not undertaken			
<p>'course grained sample' Course grained mineral within resin matrix Chunks of host rocks and sulphide Strong relief variation within samples – related to groundmass? Dominated with Garnet, quartz, some sulphides with minor micas Issues of light when viewing samples, resin blocks primary light source – can only view samples under certain settings Minerals deep within resin still viewable, can see 'ghost' grain colours deeper within sample</p>					
	Tt40b	Not undertaken			
<p>See TC400a Non uniform focus across sample – will this cause issues on the SEM? Streakiness issues. Some relationships between minerals visible – but mainly minerals are unsorted within matrix – only minor visible intergrowths Significant variations in grain size and shape – well rounded to angular, however fine grains appear less on the sample surface (lost in resin matrix) Some distinguishable features on round – SEM navigation will still be difficult</p>					

TC300	TC300A	Not undertaken				
<p>'fine grained sample' variations in grain size and shape – well rounded to angular – greater uniformity than course grained sample mainly garnet and quartz, with sulphides and minor chalcopyrite less gaps between grains – matrix less prominent no distinguishable features on rounds – will make sem exploration difficult</p>						
	TC300C	Not undertaken				

Pollock Samples				
C58	C58.1	not undertaken	unbroken	
<p>quartz with sulphide inclusions Course grained quartz with highly birefringent inclusions, quartz has room to grow comfortably implying no other significant mineral growth during formation Striations on quartz grains – could be a thin section issue? Some notable grain zonation Chalcopyrite (no pyrotite) darker/ muddier? Than previous samples- rimming by highly birefringent inclusions Limonite staining within fracture spaces 90% quartz – 8% sulphides 2% micas</p>				
C58	C58.2	not undertaken	unbroken	
<p>course grained quartz with sulphide inclusions Nice large rectangle grains of chalcopyrite (candidates for LAICPMS?) Inclusion of quartz within sulphides Highly birefringent zones within quartz – porous swiss cheese texture – fluid inclusions? Limonite stringers Thin section scratches? Micaceous mineral cross cutting features? Notable ablation halos within quartz grains Quartz sulphide mixing zone Course grown and sulphide gapfilling and overprinting Chlorite – gtassy green – not abundant but well formed grains 90% quartz 9% sulphides 1% other</p>				



Appendix B1 – GoldSniffer report

Kanmantoo Au samples and Gold Sniffer analysis

SUMMARY

- *Gold sniffer* analysis was conducted on thin-section billets and hand samples during June 2018 at the South Australian drill core reference library with assistance from G. Gordon (GSSA).
- Multiple Au grains were identified by the *Gold sniffer*.
- Follow up visual investigations were conducted on the Philips XL30 Field Emission Scanning Electron Microscope (FESEM) at the University of Adelaide.
- The Au identified by the *Gold sniffer* analysis could not be verified and were proven to not represent Au in almost all cases
- Identified minerals included: native bismuth/bismuth-bearing sulphide minerals, molybdenum, galena, thorite and monazite.
- Bismuth was the most commonly misidentified mineral during *Gold sniffer* analysis.
- Bismuth-gold intergrowth was identified but results are inconclusive at this time (further work planned).
- *Gold sniffer* ‘Au’ results hosted in quartz were, in all cases, false positives and may be the product of impurities, weathering (iron staining) or refraction.
- However, the sample suite used for this investigation may be under representative of Au abundance at Kanmantoo.
- The results of this short investigation cast doubt about the validity of previous *Gold sniffer* results on weathered core.

SAMPLE SUITE

Gold sniffer analysis was conducted during June 2018 at the South Australian drill core reference library on polished thin section sample MB15, and billets MB03, MB04, MB08, MB15, MB16, MB17, BK18, BK25A, and C58-2. Follow-up SEM sessions with a Philips XL30 Field Emission Scanning Electron Microscope (FESEM) were conducted during June 2018 at Adelaide Microscopy on polished thin section samples MB01, MB01.2, MB03, MB04, MB08, MB08.2, MB12.2, MB15, MB16 and MB17, and billets MB15, MB16, MB17.

‘GOLD SNIFFER’ OBSERVATIONS OF FREE-GOLD

Mineral insights *Gold sniffer* was used to observe locations of native free-gold within the sample suite by analysing the visible light reflection properties of Au. Colour specifications for the reflection algorithm were based on an existing Kanmantoo Au set-up, then refined to inferred Au within the sample suite (based on visible observations), as the visible reflection of Au varies with local composition.

Contact margins between sulphides and other phases produced positive results early into the session, so this was used as a guide for sample traversing.

Au was recognised in samples MB04, MB08, MB15, MB16 and MB17 with most Au identified in contact with sulphides (Figure 1). To summarise, Au was identified within;

- Sulphides (chalcopyrite and pyrrhotite), surrounding but not observed within pyrite.
- At or proximal to contacts between sulphide and micas, garnet and quartz grains.
- Associated with quartz and garnet grain along or near contact margins of sulphide (possible minor rimming of garnet grains).
- Associated with mica (biotite) and chlorite, along or near boundaries between sulphide and quartz phases.

However at the *Gold sniffer* image scale the exact host mineralogy and textural setting of the observed grains was difficult to determine (Figure 2).

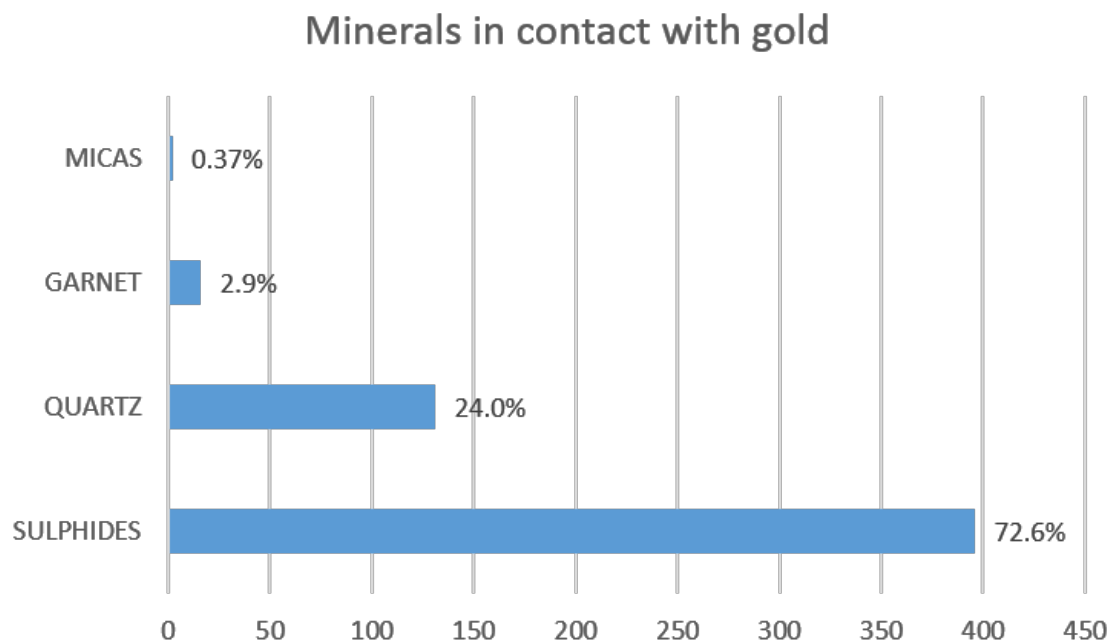


Figure 1 *Gold Sniffer* Au counts within Kanmantoo samples

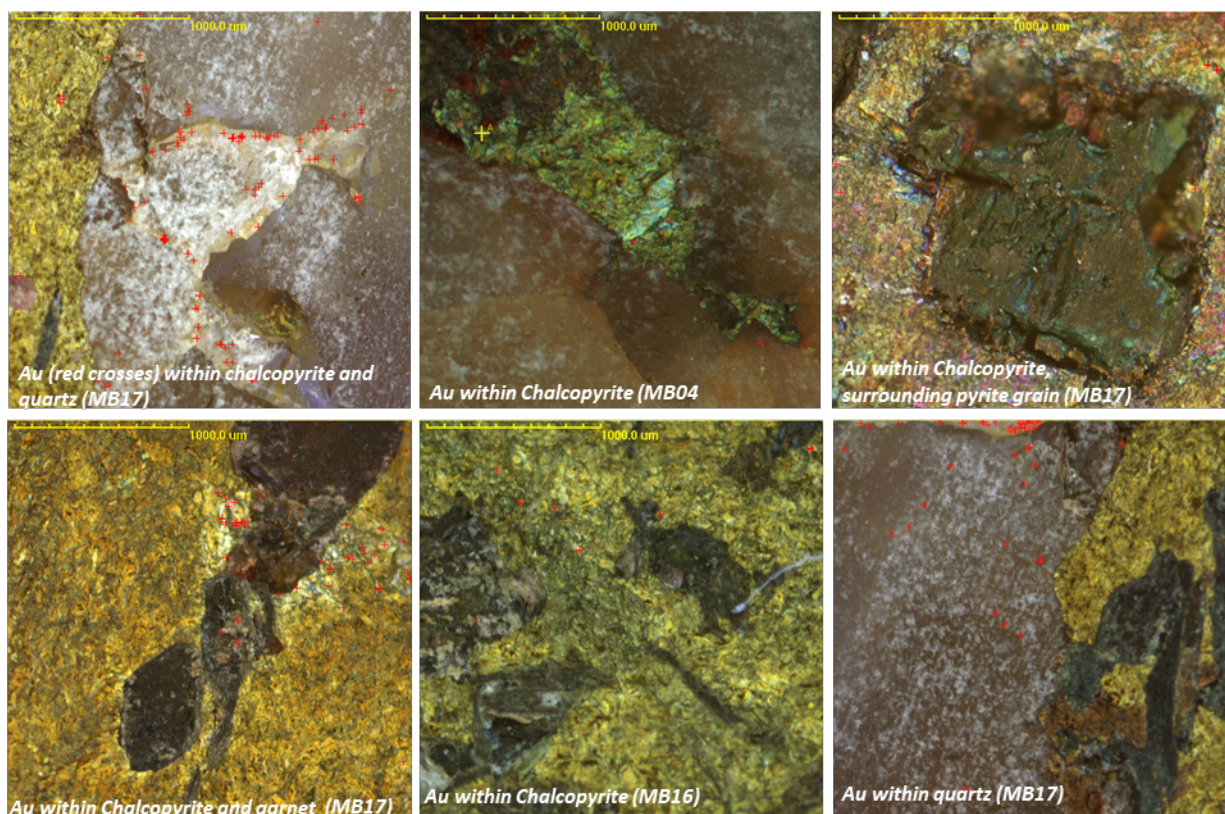


Figure 2, examples of *Gold Sniffer* Au counts (red-crosses) within Kanmantoo samples

Thin section, MB15, a sample with known Au, was also tested despite polished thin sections generally not being appropriate for *Gold Sniffer* analysis. This issue may be resolved in the future with further calibration. *Gold Sniffer* results did not identify the presence of Au in sample MB15.

The positive results of the *Gold Sniffer* investigation could not be considered conclusive until the identified Au localities had been confirmed by other analytical methods.

XL30 FESEM OBSERVATIONS

To confirm the *Gold sniffer* results the analysed samples were cross checked with the Philips XL30 Field Emission Scanning Electron Microscope (FESEM). Locations of suggested Au on billets were compared with the corresponding thin section and the billet itself for MB15, MB16 and MB17. Although the *Gold Sniffer* set-up used during these sessions was refined and recalibrated across multiple samples, SEM analysis was unable to confirm the suggested Au localities (e.g. Figure 3).

The billets MB15, MB16 and MB17 were analysed to resolve the variations between thin sections and billets. It was expected these samples would be more representative of *Gold sniffer* results. However, the analysis of these samples did not yield any further Au results. When analysed with the FESEM, these billet samples produced relatively poor high magnification imagery as the irregular surface and slope of these samples (compared to a thin section) limits effective focussing.

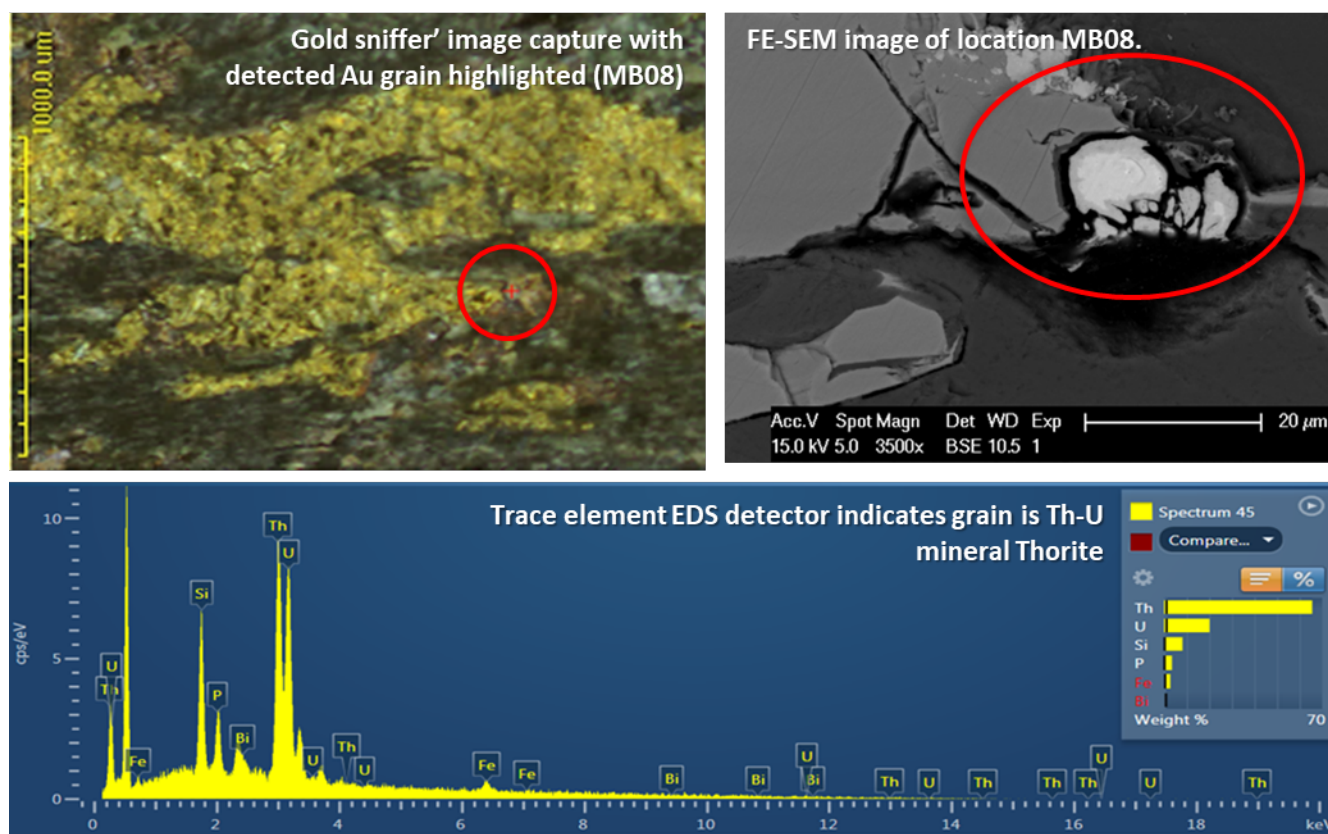


Figure 3, process of validating *Gold sniffer* results using the Philips XL30 FESEM. Top left; billet showing locations of image captures of MB08. Top right; SEM image with detected 'Au' grain highlighted. Bottom; trace element EDS detector results for suggested Au grain indicates Th, U and Si: a response typical of the trace mineral thorite ((Th,U)SiO₄).

The Au recognised in billets during *Gold sniffer* analysis was determined by EDS spectral analysis and visual observations as;

- Native bismuth and/or bismuth-bearing sulphide minerals (Figure 4)
- Molybdenum
- Galena
- Monazite
- Thorium-bearing minerals, e.g. thorite (Figure 3)
- Uranium-bearing minerals
- Trace minerals of unknown composition; mineral grain was too small for analysis and EDS spectral analysis reflective of host composition
- Colour variation within host mineral – not a trace element inclusion
- Unverified: where the compositional variation between billet and thin section was too great to accurately rule out *Gold sniffer* results
- Au (sample MB15)

Secondary electron (SE) detector mode was used to confirm the trace elements detected, as sample surface issues and gaps in the thin section carbon coating appear as similar bright spots using back scatter electron mode (BSE).

On several occasions observed trace minerals were $< 2\mu\text{m}$, attempts to gain accurate reference spectra for these grains were inconclusive, as these spectra were reflective of the surrounding host sulphides. It is suggested these grains are composed of the trace minerals as observed in the larger ($>2\mu\text{m}$) grains, however some of these grains may possibly be (native) free-gold.

Notably, the positive *Gold sniffer* results hosted in quartz were, in all cases, false positives. These false positives appear to be the product of impurities, weathering (iron staining) and possible refraction from fractures within quartz grains.

Bismuth is recognised in all samples, with significant abundances in MB12.2, MB16 and MB17 (Figure 4). Bismuth was the most commonly misidentified mineral during *Gold sniffer* analysis.

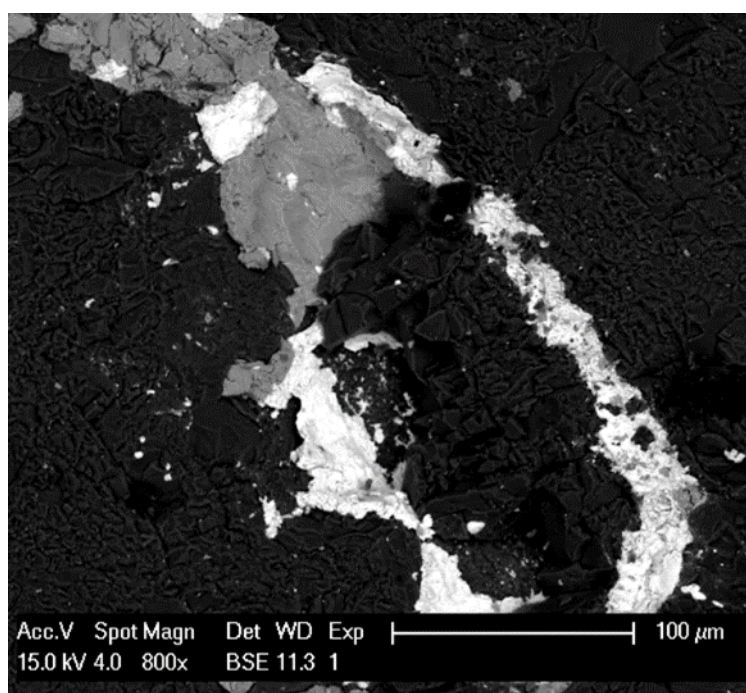


Figure 4, bismuth infill texture surrounding and fracturing quartz grain. *Gold sniffer* identified this ‘bright’ mineral assemblage as Au (billet MB17),

Many bismuth grains were tested with the EDS spectral scanner to test the validity of Bismuth as an Au pathfinder (as suggested by Ciobanu et al. 2005). Spectra for bismuth grains were checked to assess whether Au may be present as minor intergrowths. No Au peaks were recognised in larger grains, however several smaller grains displayed evidence for bismuth-gold intergrowth (Figure 5). At this time, these results are inconclusive as the spot size for the EDS analysis may have detected the Au in minerals surrounding the bismuth grains.

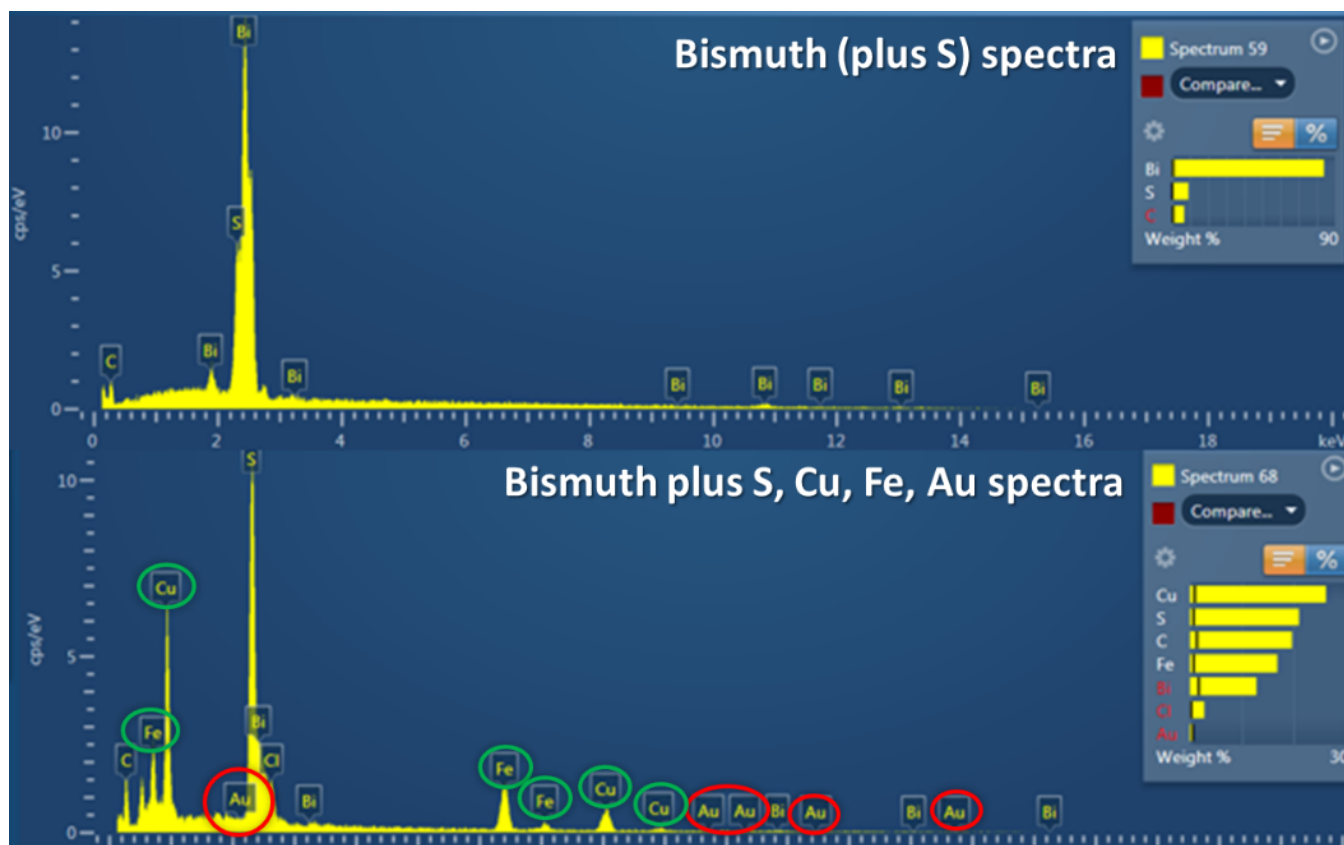


Figure 5, Bi and S spectra (Top) compared to Bi, S, Cu, Fe and Au spectra (Bottom). Because of the small size of the investigated grains, it is possible that the Cu, Fe and S represent analytical ‘scatter’ from the surrounding chalcopyrite. At this time it is not confirmed whether the detected trace levels of Au are associated with the bismuth grain or surrounding chalcopyrite.

XL30 FESEM OBSERVATIONS OF FREE-GOLD

The Au grains found on the FESEM using the *Gold sniffer* testing process for MB15 were the same grains as those previously recognised by the FEI Quanta 600 SEM and higher quality imagery of these grains have been captured as part of this work (Figure 6). Because of the small grain size, accurate reference EDS spectra of nearby Au grains < 2µm could not be captured (Figure 6 B-C). All observed Au in sample MB15 is hosted within chalcopyrite, along or near a contact boundary with quartz.

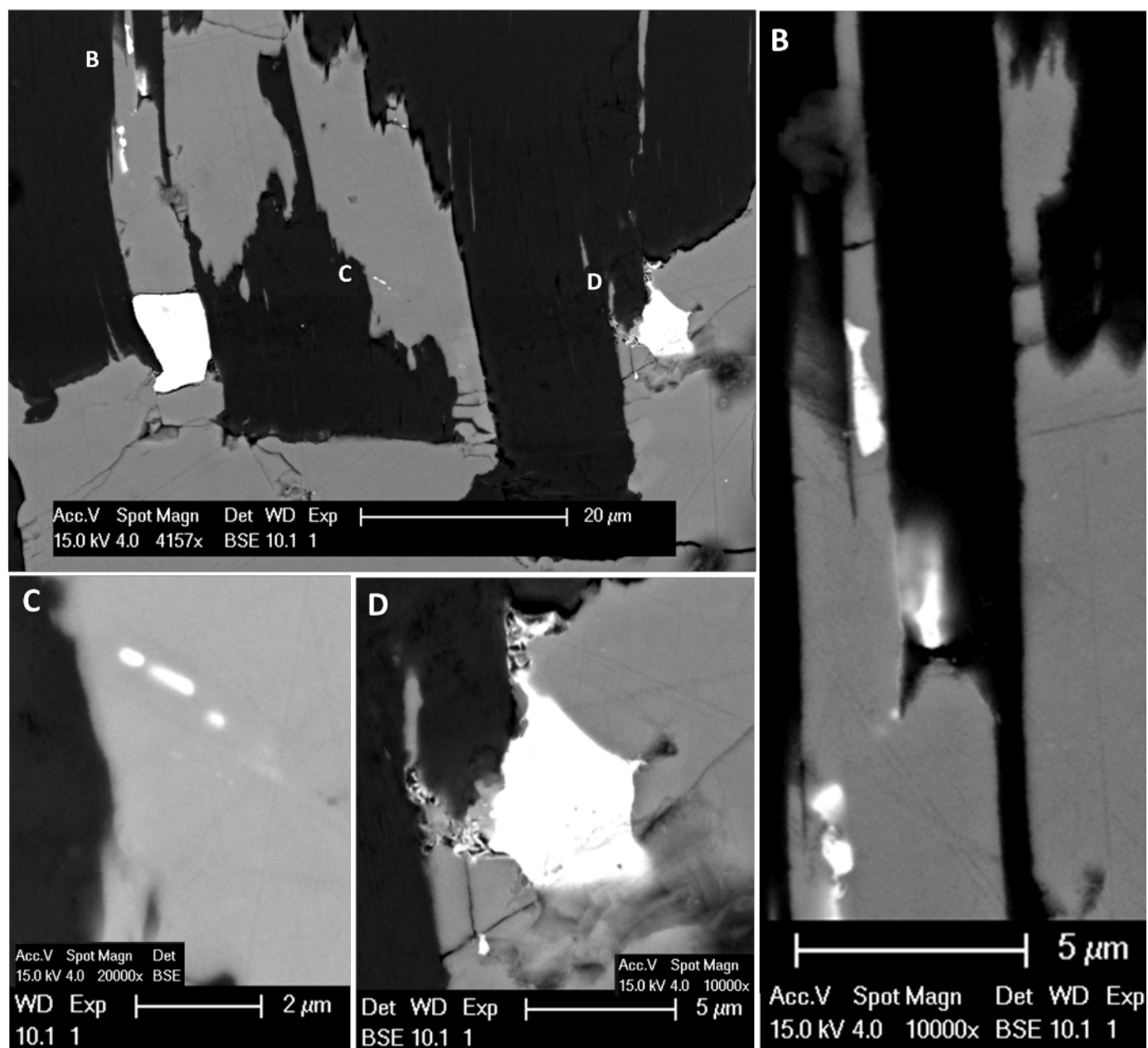


Figure 6, confirmed Au grains from thin sample MB15 (Spitfire). XL30 FESEM was able to capture more detailed images of the smaller Au grains (labelled B, C and D).

CONCLUSIONS and FUTURE WORK

While it is possible that small (<2μm) Au grains were missed during follow-up FESEM observation of samples, it is concluded that the original *Gold sniffer* reference spectra for Au was an inaccurate representation of Au within the sample suite.

However, the current sample suite may be under representative of Au, which makes the collection of representative Au reference spectra difficult for both the *Gold sniffer* and the FESEM.

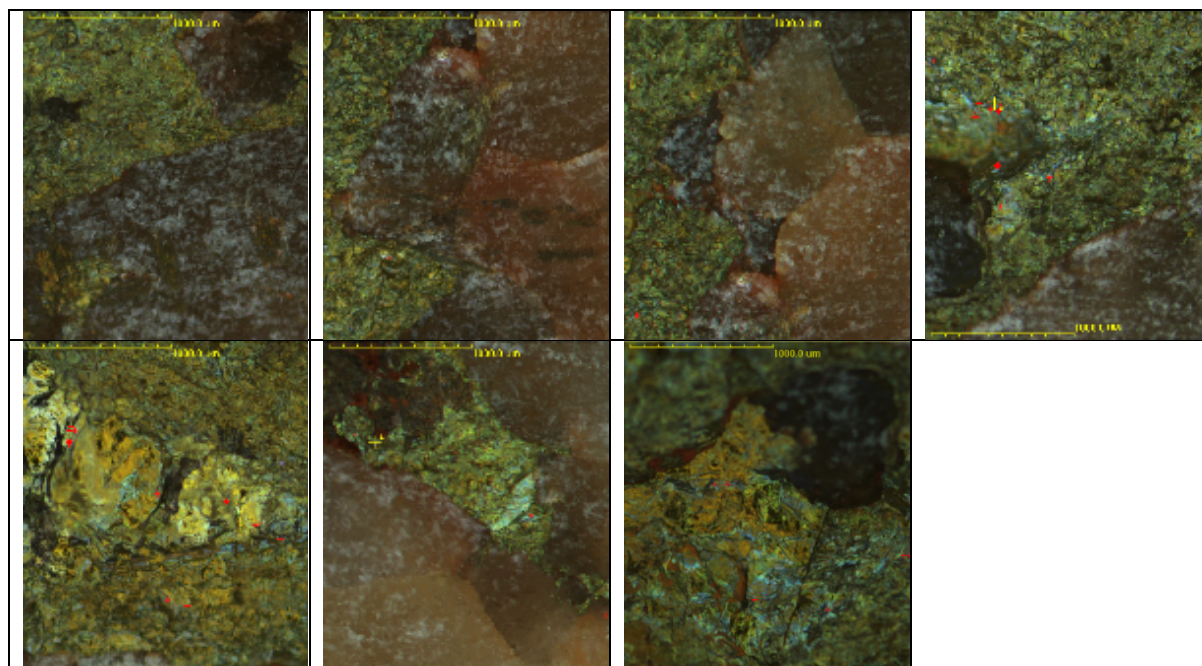
The current sample suite does not appear to contain significant Au. The lack of free-gold within this sample set may be an indicator that Au may exist as *invisible gold* in solid-solution within sulphide minerals such as chalcopyrite or bismuth sulphides.

The possible presence of Au as *invisible gold* has implications for the levels of metamorphism undergone by the ore system. Chang et al (2008) states that increasing metamorphism can promote the movement of *invisible gold* to free-gold during the recrystallization of early *invisible gold* bearing pyrite. Essentially, if the Au was present in marine sediments prior to the metamorphism of the Kanmantoo Group, more free-gold should be expected, as Au would have been liberated from solid-solution during metamorphism.

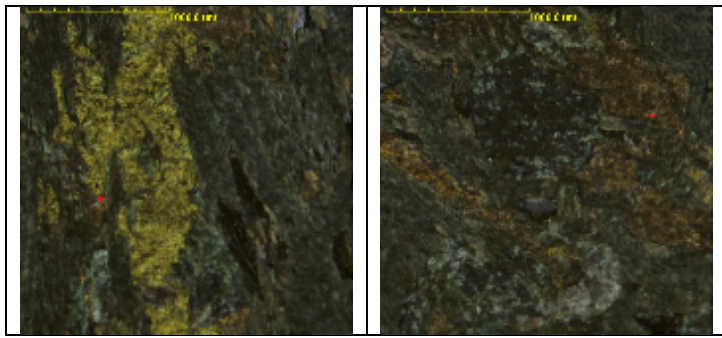
Laser Ablation-ICP-MS time is booked for July and August 2018 and will investigate the trace element composition of Bi and Cu sulphides in the existing sample suite. Additionally, preliminary SEM analysis on recently collected Kanmantoo high-Au concentrate samples will be completed during July so these samples can also undergo LA-ICP-MS analysis.

Appendix B2 – GoldSniffer detected Au locations

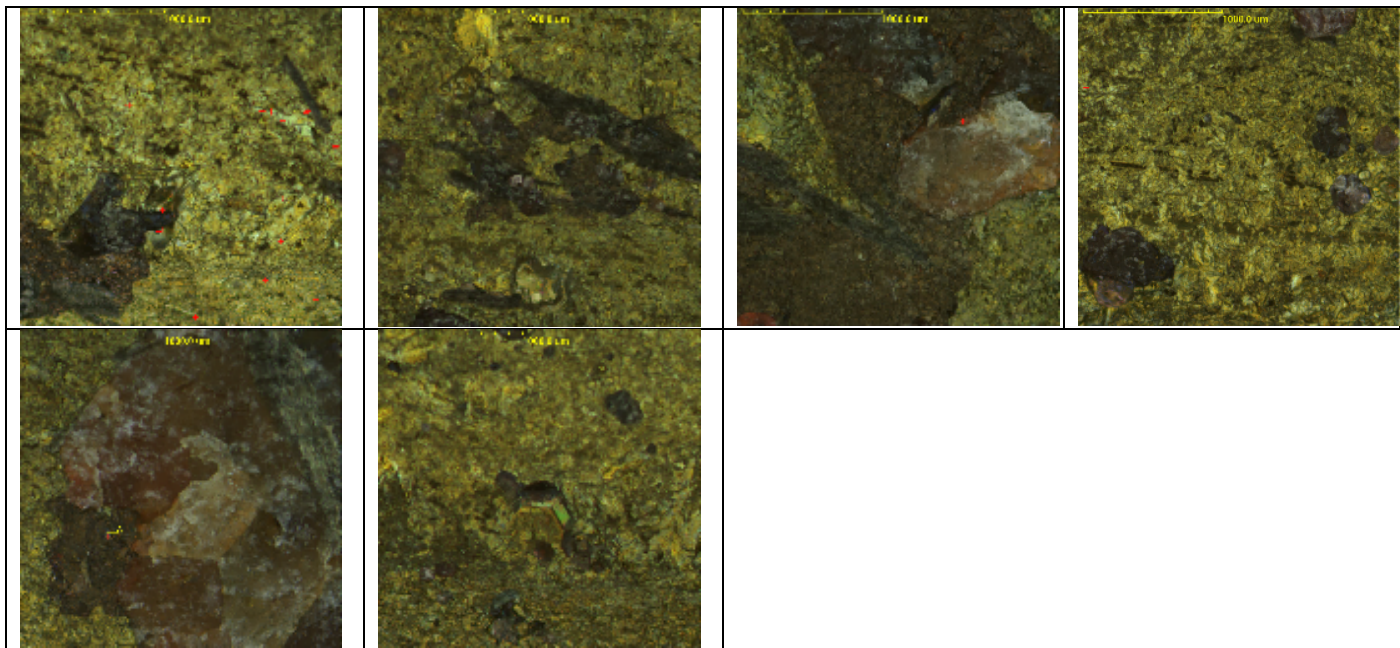
MB04



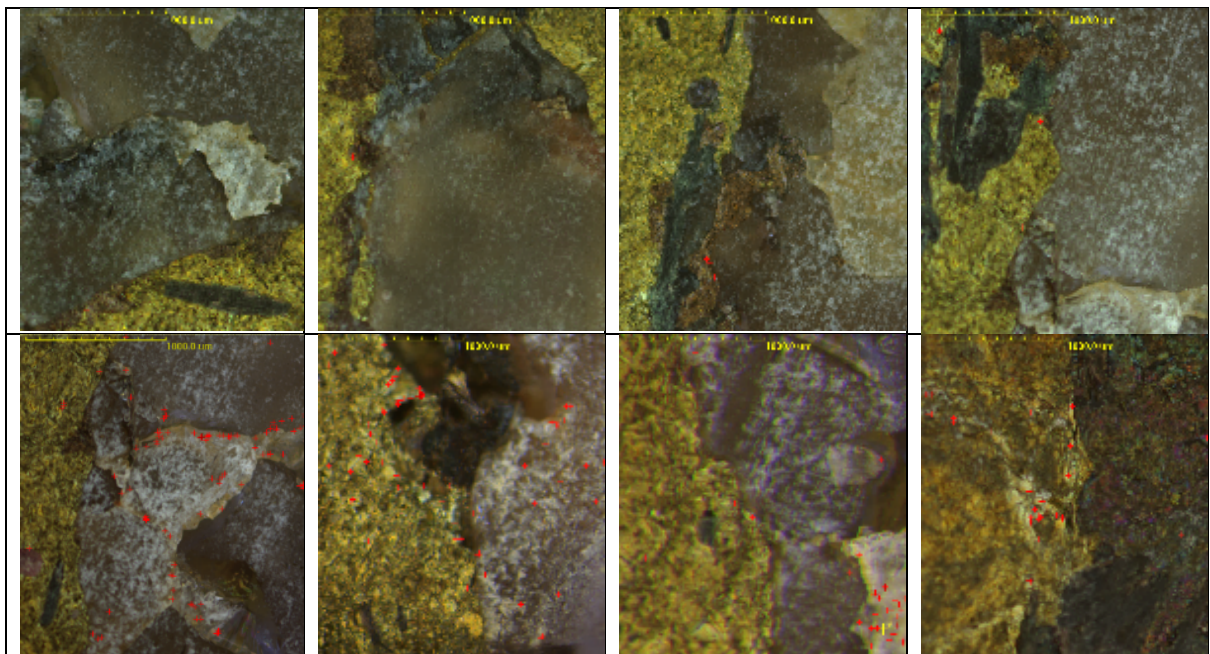
MB08

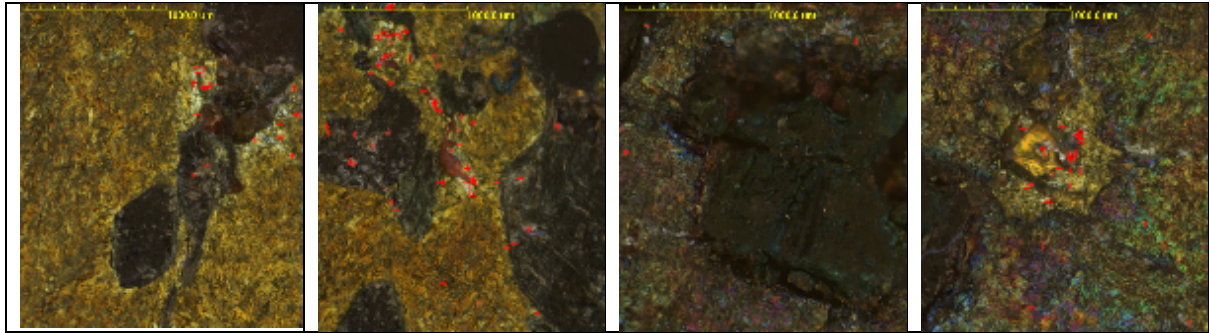


MB15

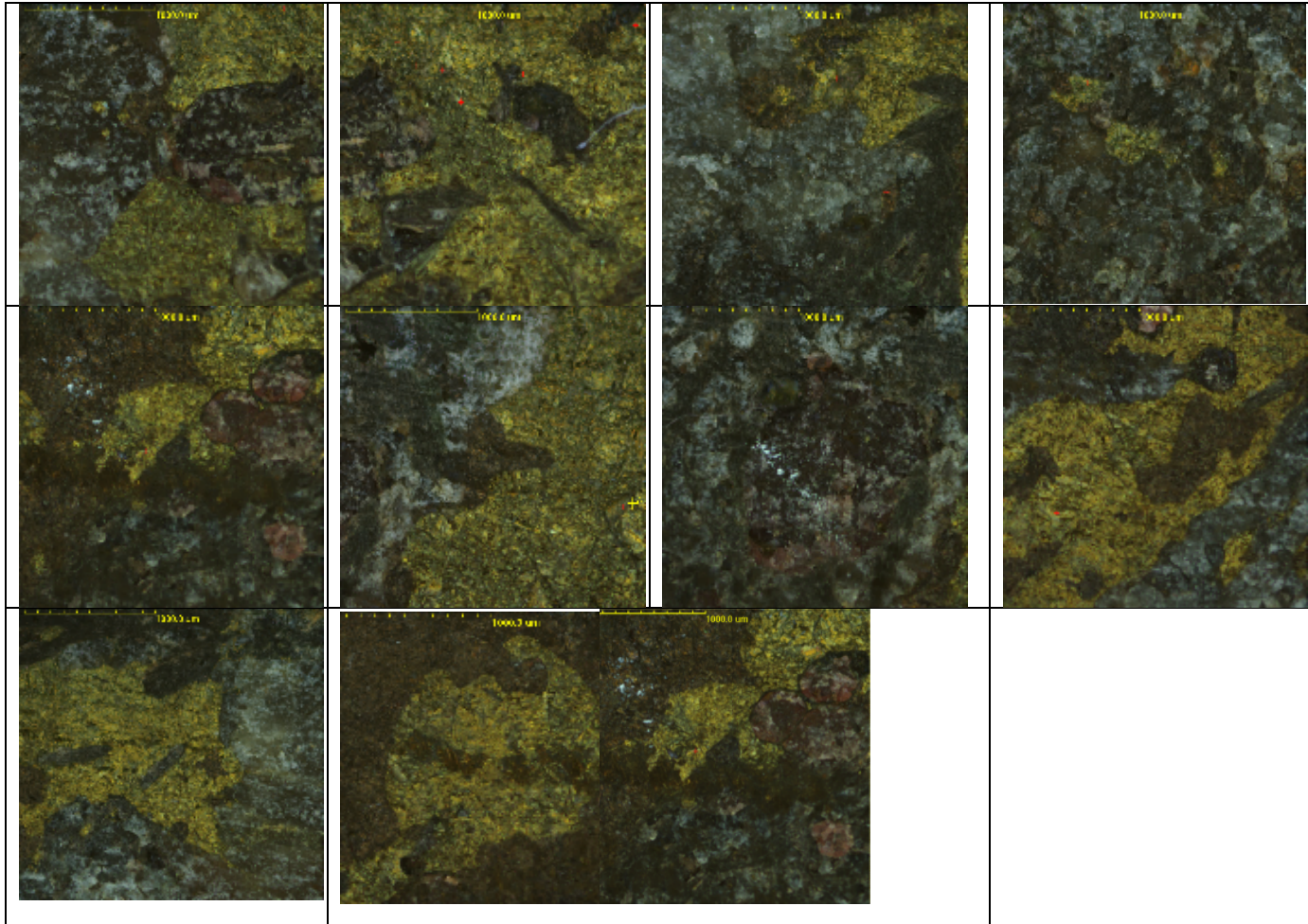


MB17

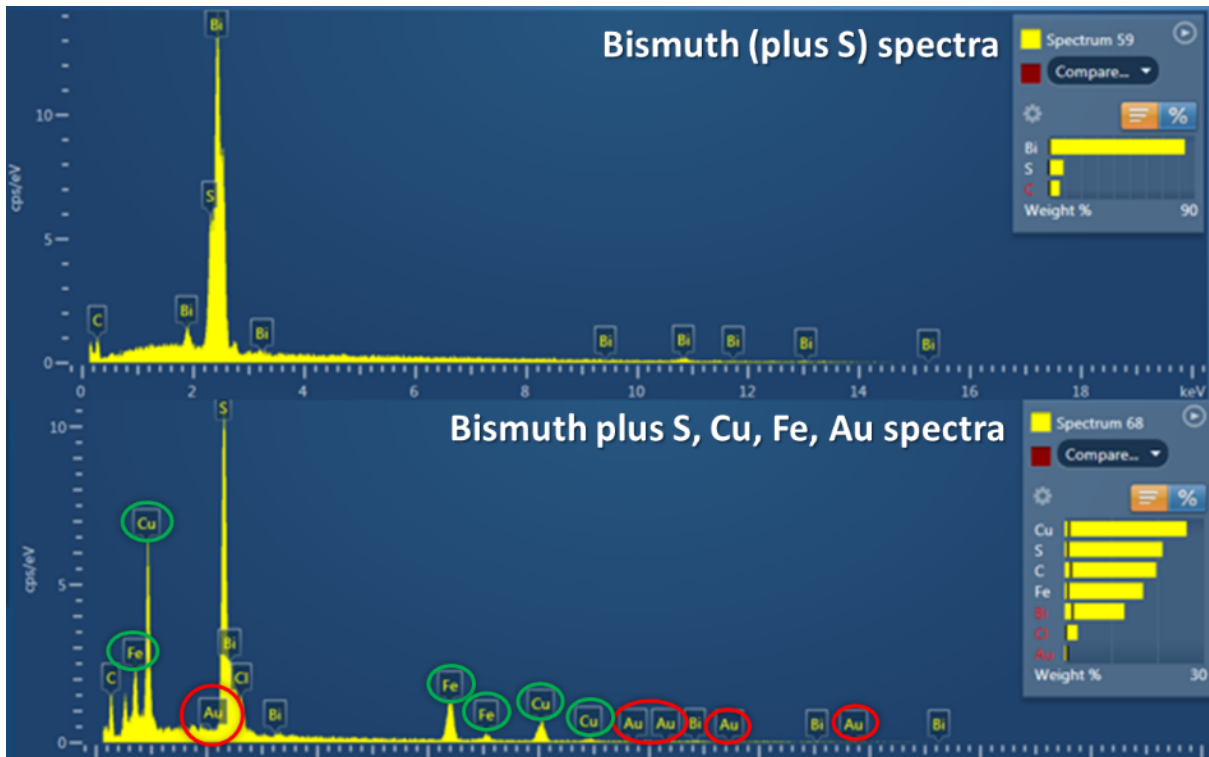




MB16



Appendix C1 - 2 Bi and S spectra (Top) compared to Bi, S, Cu, Fe and Au spectra (Bottom).



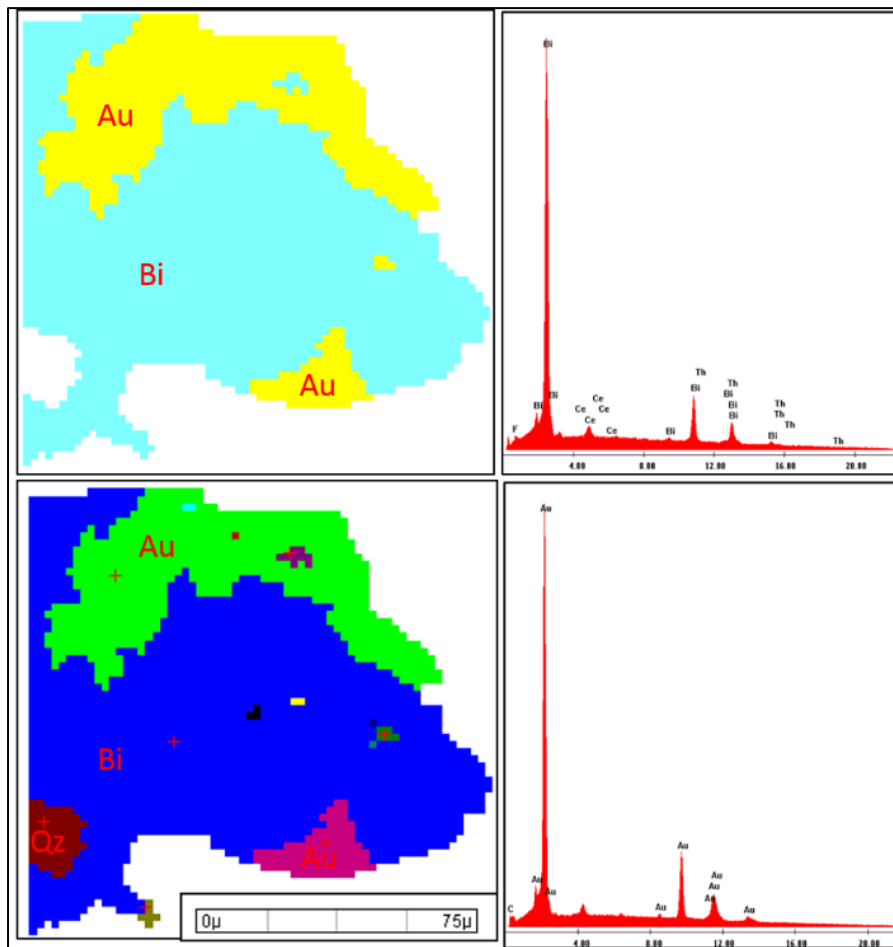
Because of the small size of the investigated grains, it is possible that the Cu, Fe and S represent analytical ‘scatter’ from the surrounding chalcopyrite. At this time it is not confirmed whether the detected trace levels of Au are associated with the bismuth grain or surrounding chalcopyrite.

Appendix C2 - Spectral match analysis, showing similarity of an unknown mineral to existing spectral captures, (edited for clarity)

Mineral	XRay	Score	Mineral List
Mineral	XRay0	100.00	MB_KAN_2
au2	XRay0	99.96	MB_KAN_2
au3	XRay0	99.96	MB_KAN_2
gold standard	XRay0	99.57	MB_KAN_2
goldmb15	XRay0	96.93	MB_KAN_2
Native_Gold	Native_Gold	84.69	MB_KAN_2

Mineral represents Au1 from the concentrate sample suite, au2 and au3 represent gold from the concentrate sample suite, gold standard represents the Au standard within the SEM standard round, goldMB15 represents Au spectral data collected from thin section MB15 and Native_gold is the FEI standard reference for Au spectra.

Appendix C3 - FEI Quanta 600 MLA Scanning Electron Microscope results example

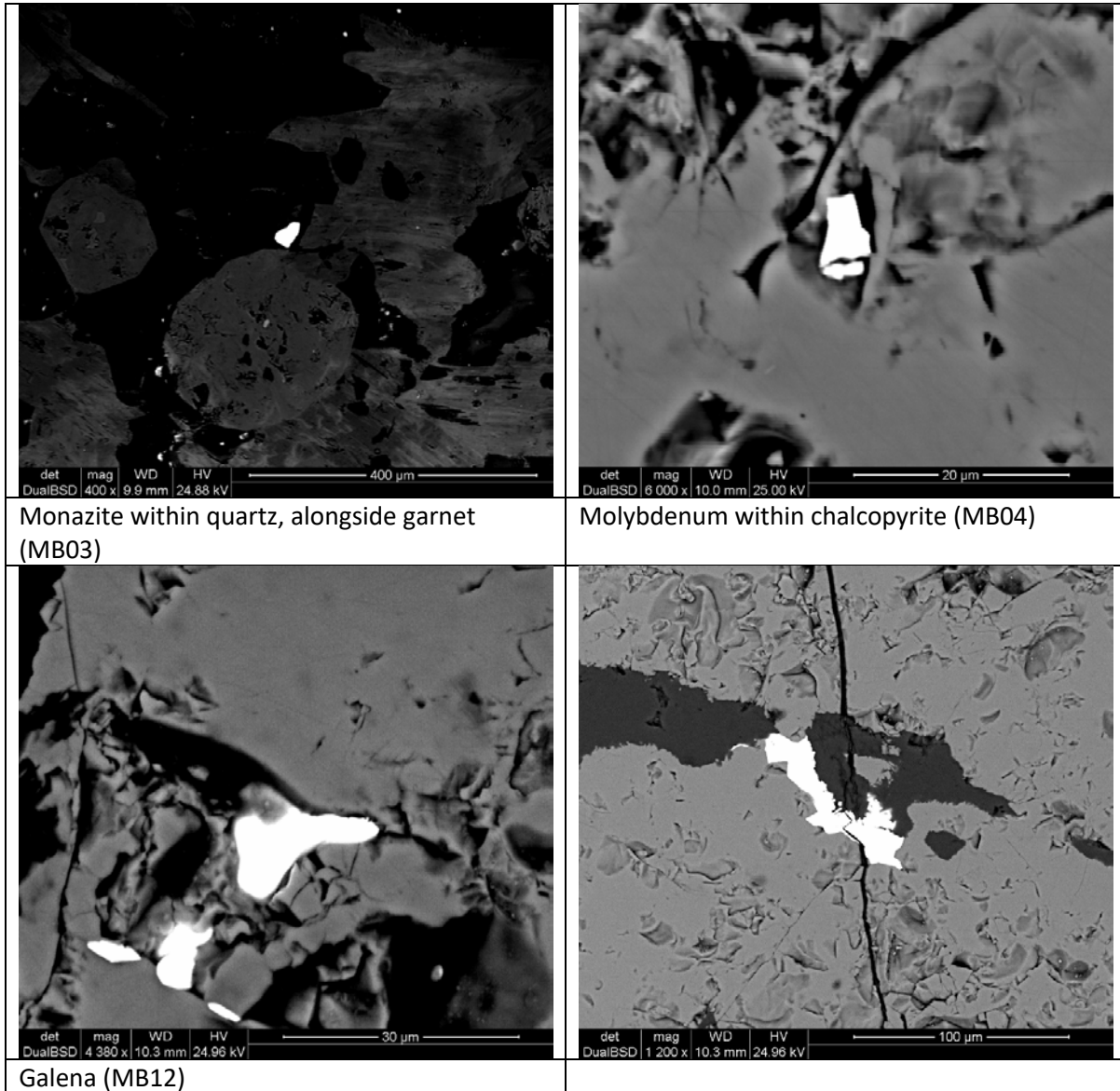


Top & bottom left; classified MLA processing map results, top left showing the result of the classification process, simplified to observe only trace element phases, bottom left showing ‘true’ X-ray results with slight variation of spectral signature within a single mineral grain. Top right; EDS spectral count for Bi phase validating MLA results. Bottom right; EDS spectral count for Au phase validating MLA results.

Appendix D1 - SEM imagery - Bi

<p>det mag WD HV DualBSD 354 x 9.8 mm 24.88 kV</p> <p>400 μm</p>	<p>det mag WD HV DualBSD 1 508 x 9.8 mm 24.88 kV</p> <p>100 μm</p>
<p>Bi within chalcopyrite (MB01.2)</p>	<p>Bi within chalcopyrite (MB03)</p>
<p>det mag WD HV DualBSD 274 x 9.6 mm 24.88 kV</p> <p>500 μm</p>	<p>det mag WD HV DualBSD 573 x 9.6 mm 24.88 kV</p> <p>300 μm</p>
<p>Bi overprinting (MB12)</p>	<p>Bi within garnet (MB12)</p>
<p>Acc.V Spot Magn Det WD Exp 15.0 kV 4.0 650x BSE 11.0 1</p> <p>100 μm</p>	<p>Acc.V Spot Magn Det WD Exp 15.0 kV 4.0 800x BSE 11.3 1</p> <p>100 μm</p>
<p>Bi (MB16)</p>	<p>Bi surrounding quartz grain (MB17)</p>

Appendix D2 - Sem imagery - other trace elements



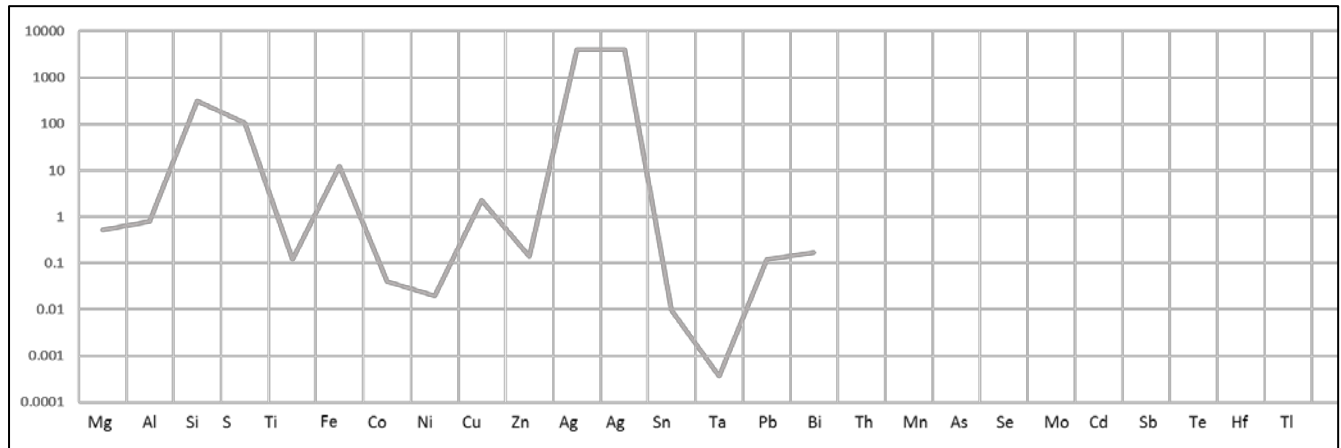
Appendix E1 – Laser data summary

Sulphide geochemistry, classified into different ore lodes, where ‘-’ denotes values below detection limits (no average can be produced). full element suite; Fe, Mg, Al, Si, S, Ti, V, Cr, Mn, Co, Ni, Cu, Zn, As, Se, Mo, Ag, Cd, Sn, Sb, Te, Hf, Ta, W, Au, Hg, Tl, Pb, Bi and Th. Wt% Fe of 30.5% for chalcopyrite, 61% for pyrrhotite, 72% for magnetite and 56.5% for pyrite used for calculations.

Ore lode	Mineral		S Ppm	Cu	Ag	Au	Bi	Co	Ni	As	Zn
West Kavanagh	Chalcopyrite	Mean	434000	371000	159	0.0765	3.38	21.3	41.3	1.11	574
		Std	35400	33800	11.6	0.0384	0.379	4.23	6.94	0.73	109
	Pyrrhotite	Mean	437000	18.1	2.5	0.022	1.72	1560	327	1.13	12.2
		Std	32000	6.07	0.688	0.0195	0.284	101	20.9	0.58	10.3
	Magnetite	Mean	7960	4510	2.13	0.133	17.5	53.9	15.3	0.444	61.1
		Std	1460	1020	0.653	0.118	4.73	5.23	1.71	0.844	19.4
East Kavanagh	Chalcopyrite	Mean	409000	359000	76.1	0.117	8.62	19.2	1	0.99	557
		Std	40000	37800	6.85	0.0669	1.59	8.69	0.578	0.54	121
	Pyrrhotite	Mean	425000	5.07	1.08	0.0875	1.78	1450	180	2.4	10.4
		Std	38900	3.68	0.412	0.0394	0.41	104	14.7	1.8	6.1
	Pyrite	Mean	547000	0.996	0.388	-	0.407	3950	395	-	0.933
		Std	20200	0.694	0.16	-	0.0661	147	12.9	-	0.414
Spitfire	Chalcopyrite	Mean	420000	365000	93.5	0.157	2.89	17.9	31.5	0.785	740
		Std	35300	34800	7.24	0.063	0.38	3.52	6.28	0.47	190
	Pyrrhotite	Mean	446000	2260	2.72	0.062	2.43	1040	206	2.02	32.3
		Std	40200	538	0.758	0.033	0.519	81.8	21.3	1.32	9.11
	Pyrite	Mean	695000	2540	34.8	0.0503	0.903	8.7	17.3	-	318
		Std	76000	648	3.86	0.0343	0.147	1.73	2.87	-	58
Magnetite	Mean	4070	3160	3.84	0.093	11.6	13.1	3.6	-	84.1	
	Std	904	823	0.945	0.0665	4.63	1.16	0.724	-	29.9	
Nugent	Chalcopyrite	Mean	457000	366000	5.02	0.0399	0.475	76.9	43.3	14.4	430
		Std	29100	26100	0.39	0.0112	0.0692	5.38	3.86	1.58	41.9
	Pyrrhotite	Mean	648000	6880	187	1.87	1.16	1390	519	6.5	29.6
		Std	23600	319	6.76	0.098	0.214	61.8	26.2	0.895	2.22
	Pyrite	Mean	603000	4.01	3.21	0.053	1.87	1570	478	-	2.1
		Std	23800	2.41	0.295	0.033	0.763	64.5	21.8	-	0.87
300 g/t Au con.	Chalcopyrite	Mean	337000	92700	24.2	0.127	5.48	780	198	0.342	130
		Std	13800	5650	1.21	0.0184	0.5	23.1	8.14	0.113	15.2
	Pyrrhotite	Mean	511000	197	2.58	0.217	8.09	1690	366	0.33	1.47
		Std	23400	29.1	0.304	0.0573	1.77	65.5	16.7	0.22	0.505
	Magnetite	Mean	267714	56.96	260	21546	66.95	134	54.5	2.7	12.68
		Std	29300	22.6	77.972	5096	22.22	18.61	9.23	3.7	4.9667
40 g/t Au con.	Chalcopyrite	Mean	382000	280000	60.4	0.0993	6.62	438	103	0.27	643
		Std	16500	12400	2.38	0.017	5.27	23.3	9.5	0.129	85.5
	Pyrrhotite	Mean	530000	3.73	0.605	0.0622	2.93	1440	348	-	43.1
		Std	28200	2.45	0.107	0.0383	0.6	49.1	12.7	-	18.4
	Magnetite	Mean	5106.667	1023.233	2.05	0.326	7.7349	18.7422	3.5133	1.89	110.489
		Std	840	161.688	0.385	0.075	1.6239	1.6278	0.6433	0.47	22.1
Pyrrhotite	Mean	606000	23.9	5.38	0.0135	6.08	2320	379	0.743	7.43	
	Std	16200	7.04	0.567	0.00789	4.15	111	24.1	0.207	4.07	
Late intrusives	Chalcopyrite	Mean	442000	363000	54.2	0.0612	7.52	11.8	12.5	0.576	746
		Std	23700	21400	2.8	0.0147	2.36	3.33	2.91	0.203	130
	Pyrrhotite	Mean	606000	23.9	5.38	0.0135	6.08	2320	379	0.743	7.43
		Std	16200	7.04	0.567	0.00789	4.15	111	24.1	0.207	4.07
	Magnetite	Mean	44674	10.1	-	0.025	0.4	14.55	19.86	2.52	18.7
		Std	13546	2.8	-	0.041	0.138	2.454	4.662	1.045	3.08

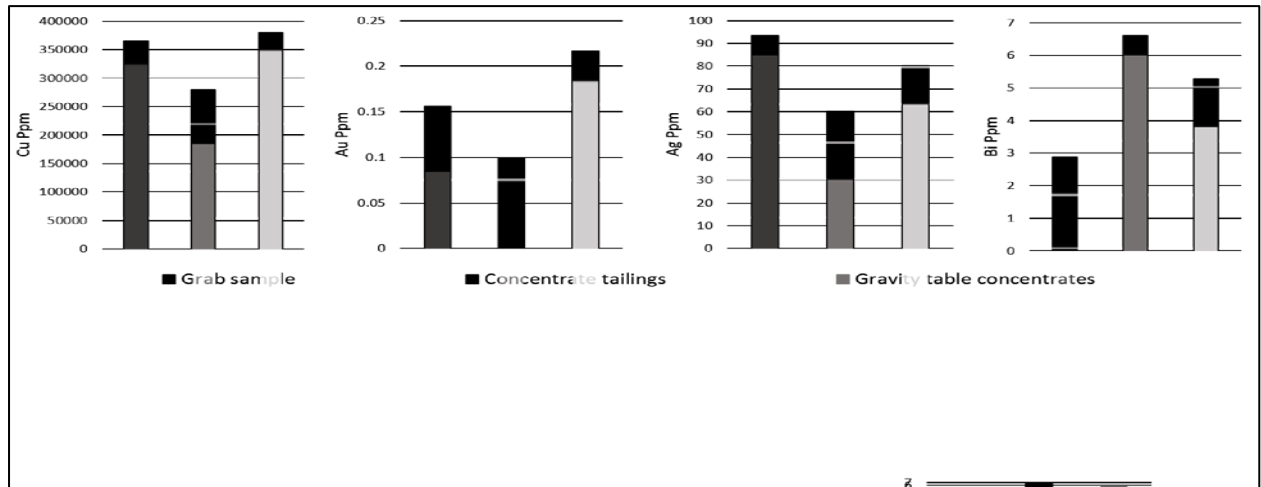
Bismuth geochemistry, classified into different ore lodes, Where ‘-’ denotes values all below the detection limit (no average can be produced). full element suite available in appendix, including; Fe, Mg, Al, Si, S, Ti, V, Cr, Mn, Co, Ni, Cu, Zn, As, Se, Mo, Ag, Cd, Sn, Sb, Te, Hf, Ta, W, Au, Hg, Tl, Pb, Bi and Th. Wt% Bi of 98% used for calculations.

Ore lode		S	Fe	Cu	As	Ag	Te	Au
300 g/t Au con.	Mean	323	28.4	14	0.36	1.06	2.94	0.0916
	Std	103	8.17	1.64	0.477	0.16	1.23	0.0282
West Kavangah	Mean	2550	3810	0.262	-	2.98	6.48	0.0124
	Std	1100	1730	0.224	-	1.54	2.81	0.00745
East Kavangah	Mean	207	2260	1.34	0.311	36	8.4	0.673
	Std	184	1830	1.36	0.305	19.4	5.99	0.381



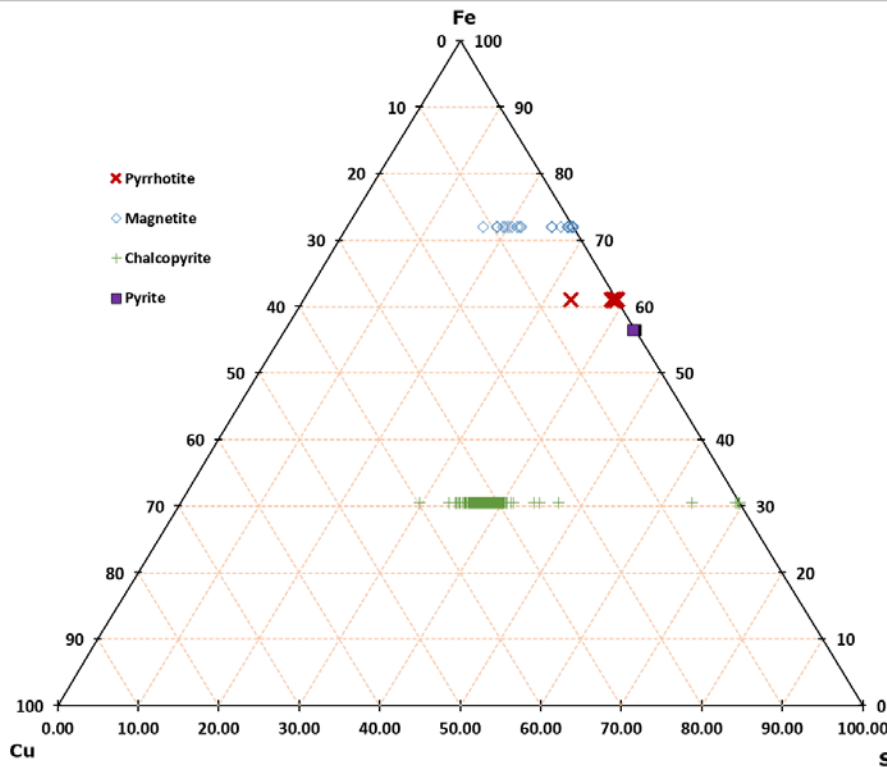
Assay data for 'Free' Au grain found in Spitfire 300 g/t concentrate, with values for quantifiable elements in Ppm, and non-quantifiable elements in CPS. Elements Th, Mn, As, Se, Mo, Cd, Sb, Te, Hf, W and Tl are not detected above confidence levels, Wt% Au of 98% used for calculations, n = 10.

Appendix E2 – Grab to Con LA-ICP-MS data



Chalcopyrite LA-ICP-MS data from the Spitfire ore lode, with variations in Cu, Au, Ag and Bi (in Ppm), showing successful extraction and recovery of Cu, Au and Ag with current metallurgical operating conditions, where Hillgrove Resources successfully recover 90-92% of Chalcopyrite (P Rolley Pers. Comm. 2018).

Appendix 3E - LA-ICP-MS assay result ternary diagrams



Ternary phase diagram for Chalcopyrite, pyrrhotite, pyrite and magnetite, using LA-ICP-MS results from samples MB01.2, MB04, MB08.2, MB12, Mb15 and MB16

Appendix E4- LA-ICP-MS Elemental plots

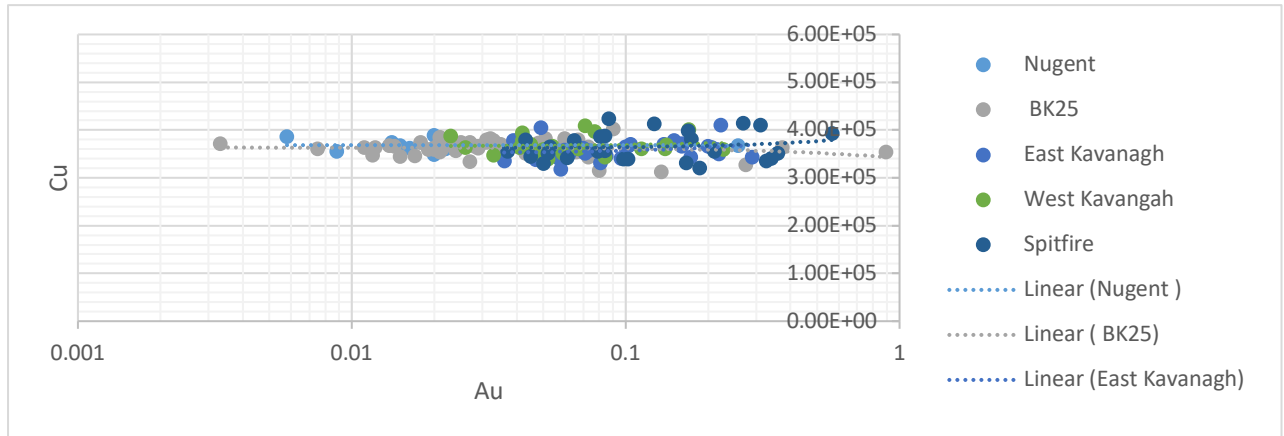


Figure 3 Cu:Au horizontal log plot for Chalcopyrite LA-ICP-MS spot data, demonstrating no significant trend between Cu:Au within Chalcopyrite

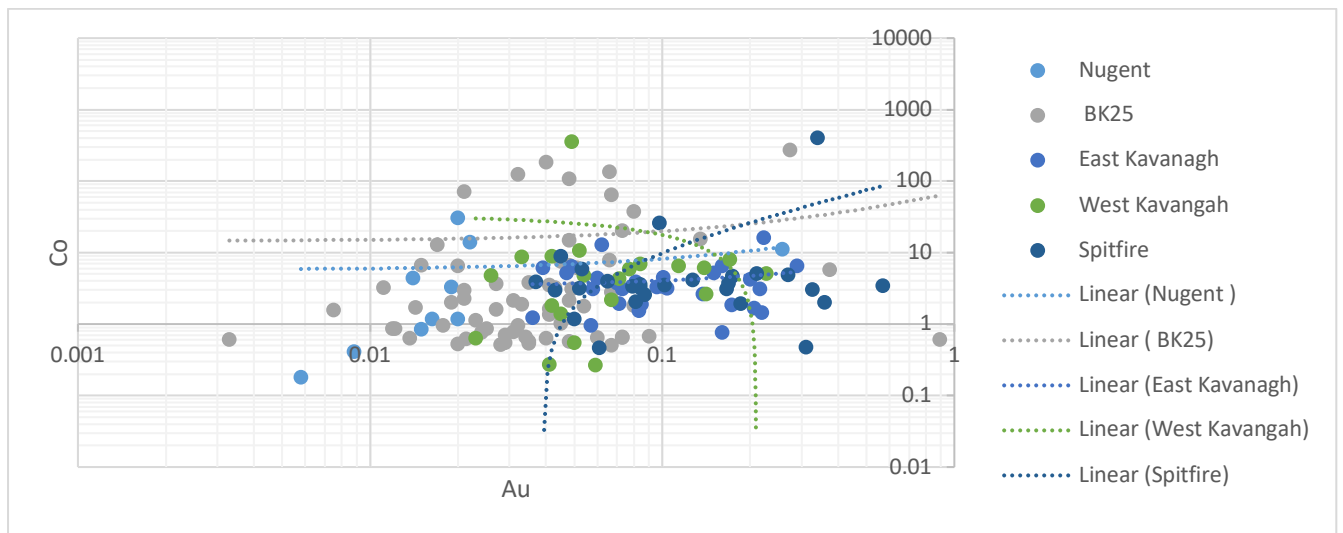


Figure 4 Co:Au log log plot for Chalcopyrite LA-ICP-MS spot data

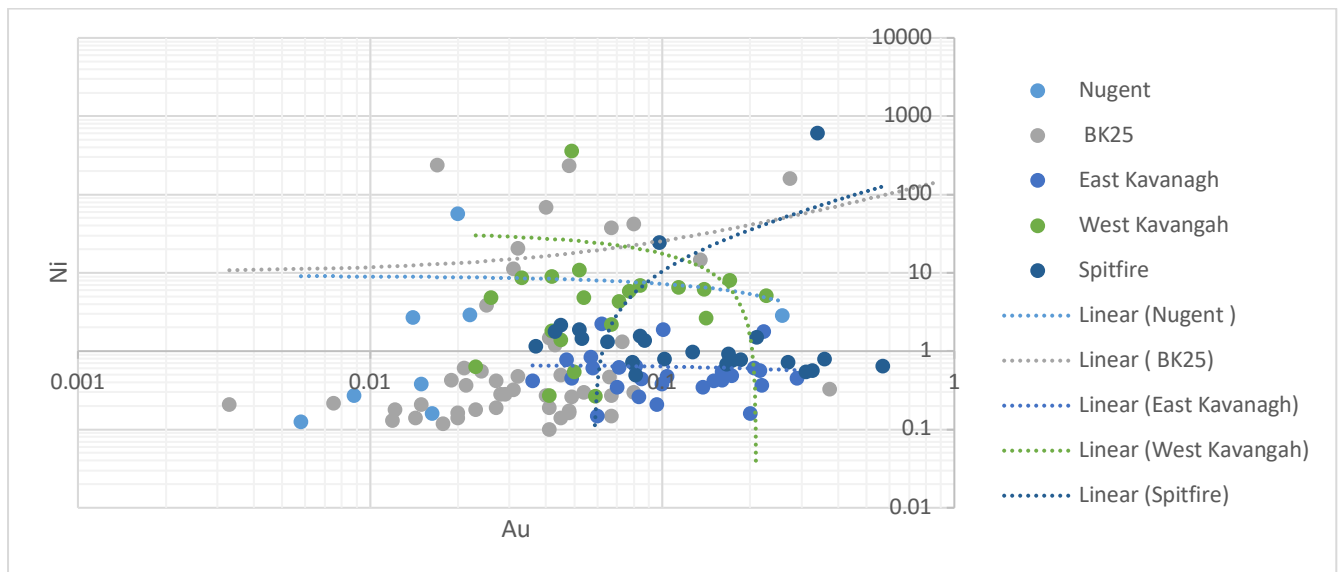


Figure 5 Ni:Au log log plot for chalcopyrite LA-ICP-MS spot data

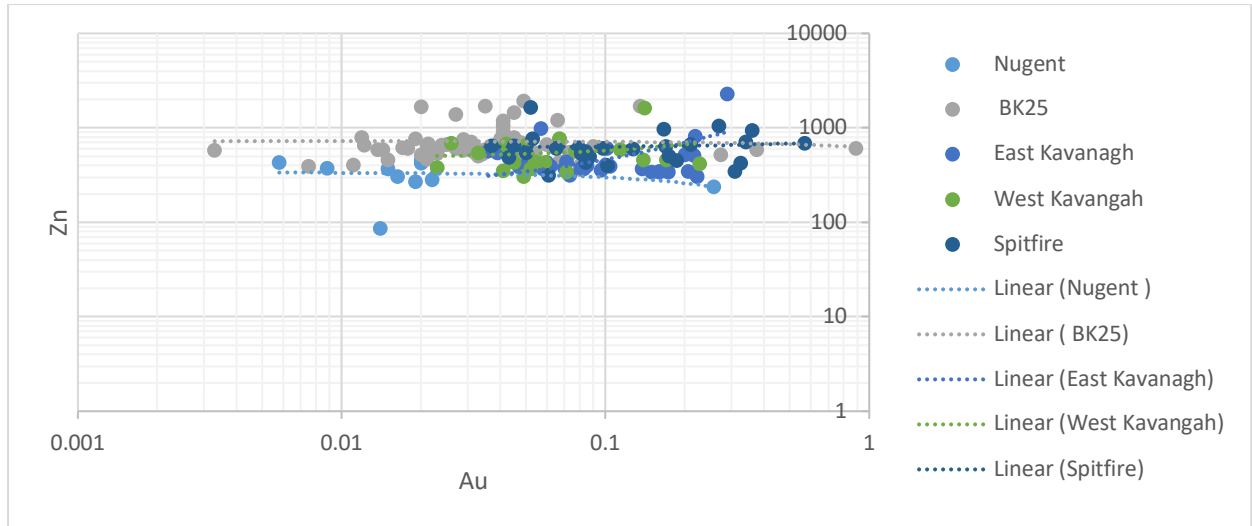


Figure 6 Zn:Au log log plot for chalcopyrite LA-ICP-MS spot data

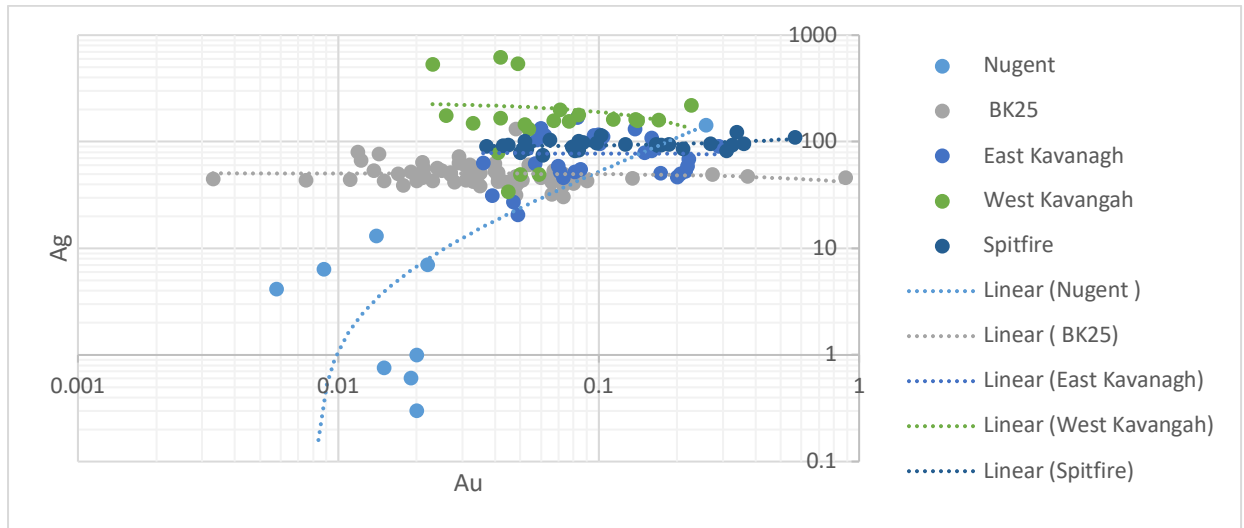


Figure 7 Ag:Au log log plot for chalcopyrite LA-ICP-MS spot data

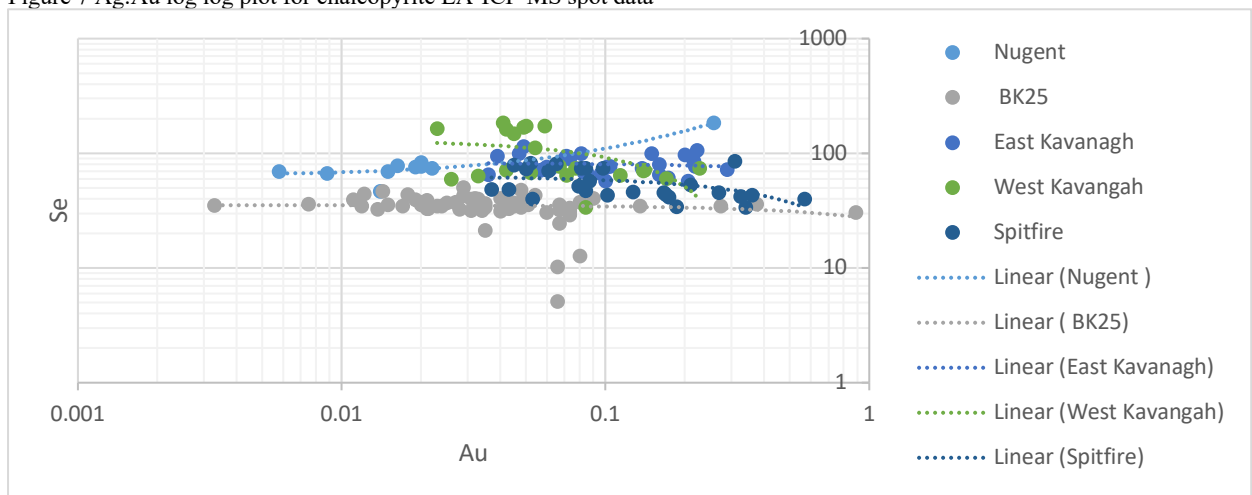


Figure 8 Se:Au log log plot for chalcopyrite LA-ICP-MS spot data

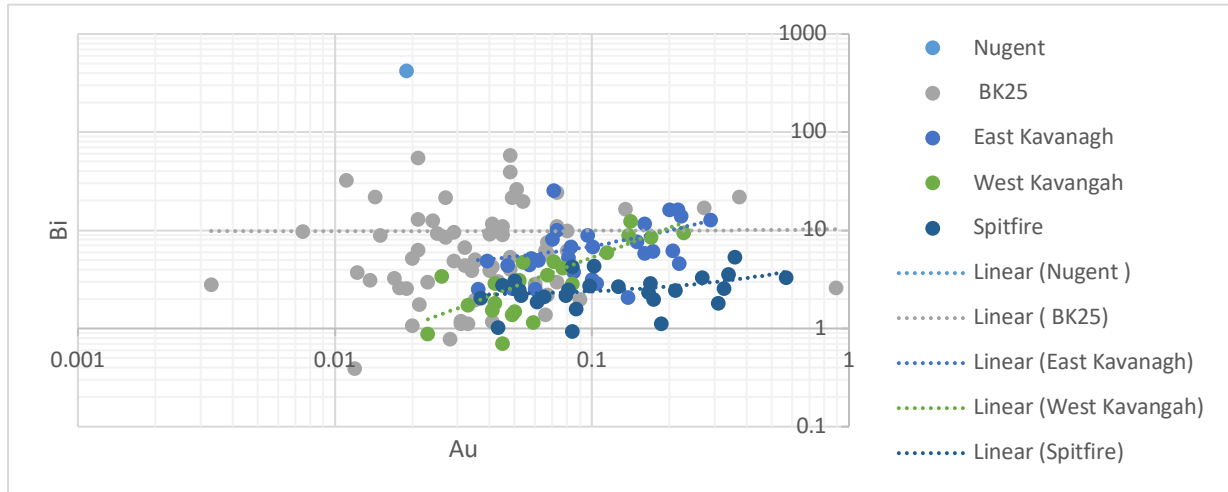


Figure 9 Bi:Au log log plot for chalcopyrite LA-ICP-MS spot data

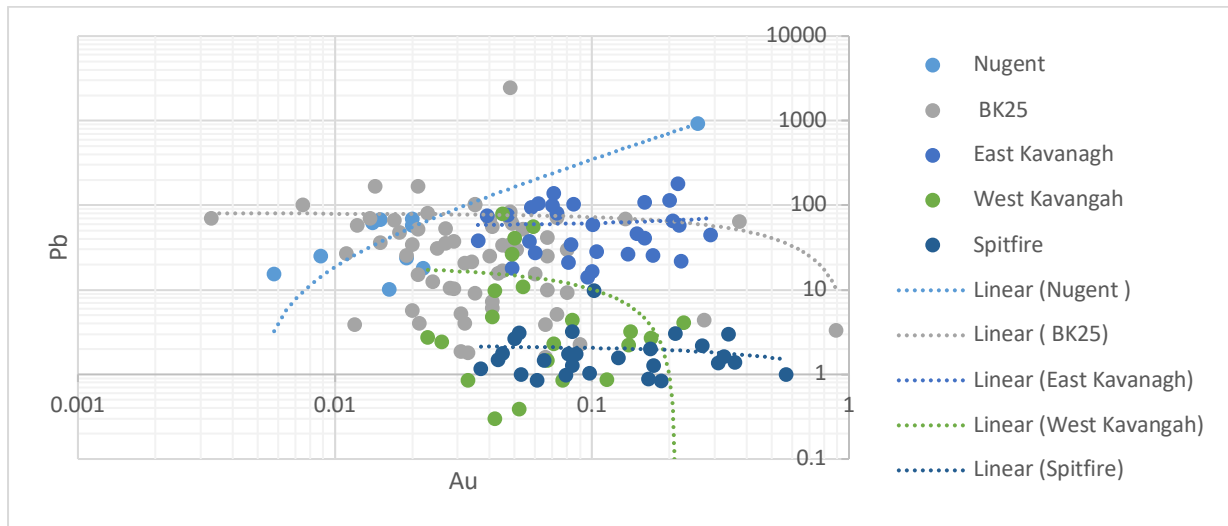


Figure 10 Pb:Au log log plot for chalcopyrite LA-ICP-MS spot data

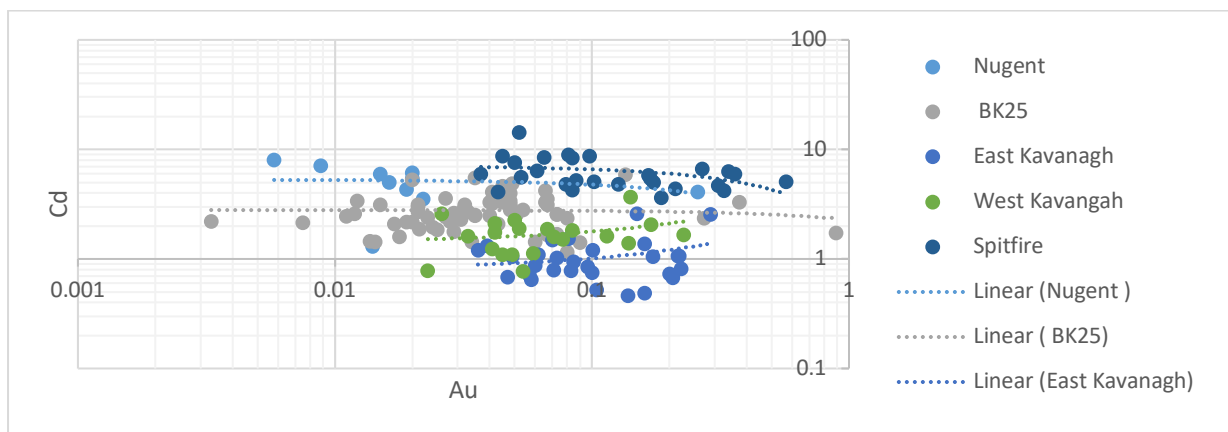


Figure 11 Cd:Au log log plot for chalcopyrite LA-ICP-MS data

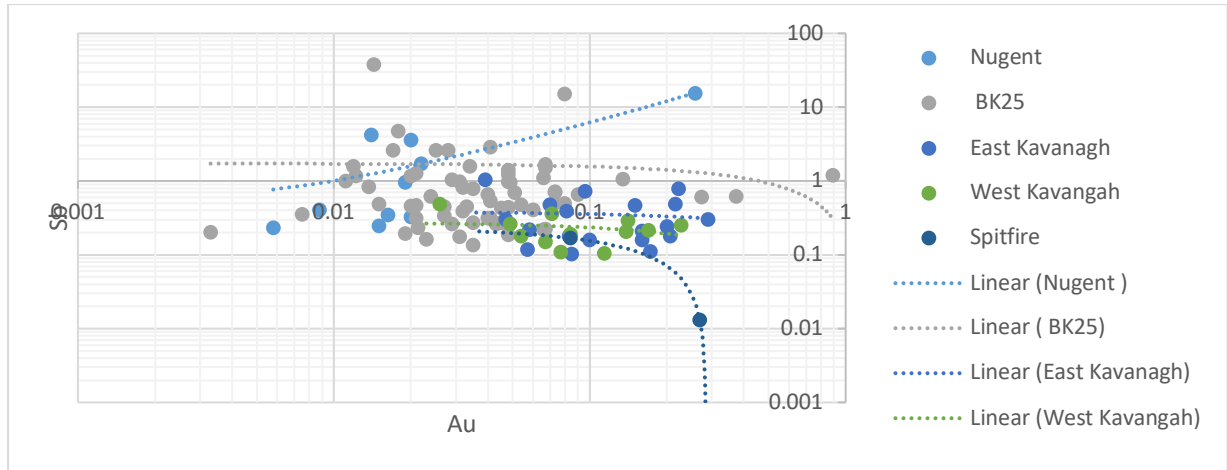


Figure 12 Sb:Au log log plot for chalcopyrite LA-ICP-MS data

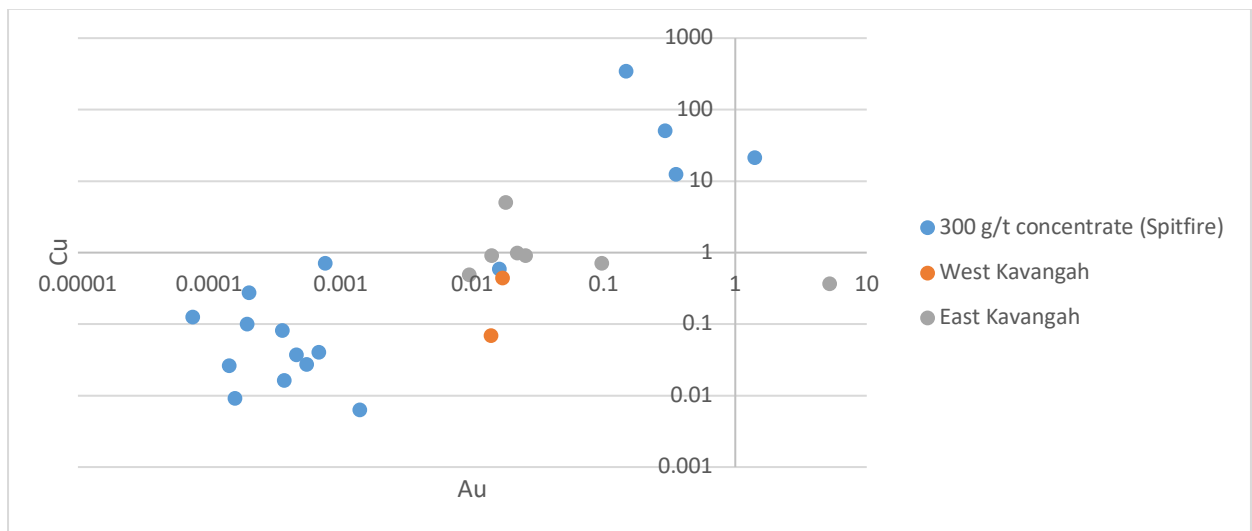


Figure 13 Cu:Au log log plot for Bi LA-ICP-MS data

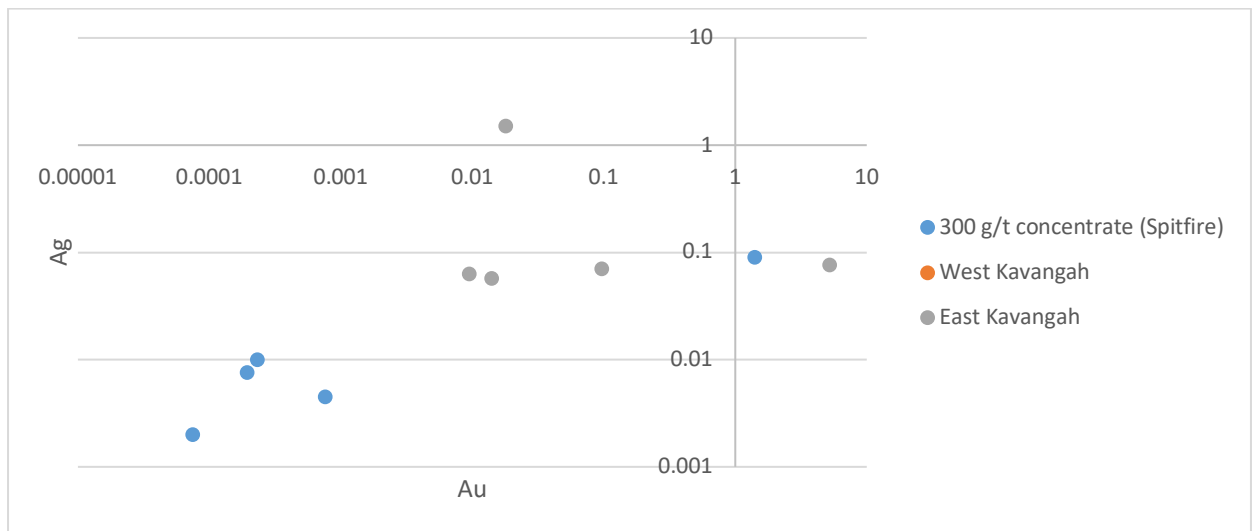


Figure 14 Ag:Au log log plot for Bi LA-ICP-MS

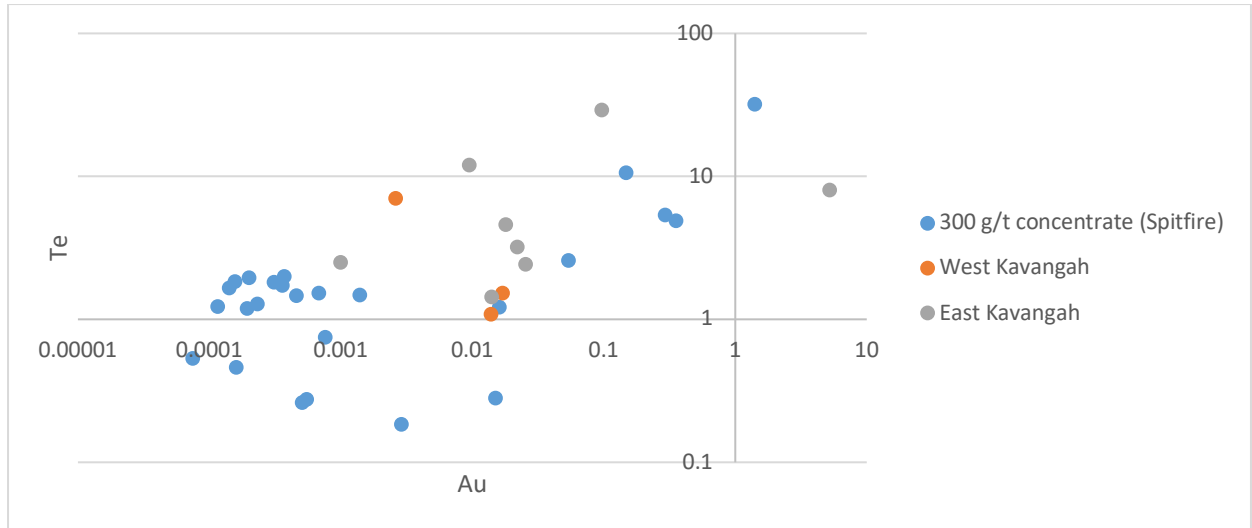


Figure 15 Te:Au log log plot for Bi LA-ICP-MS

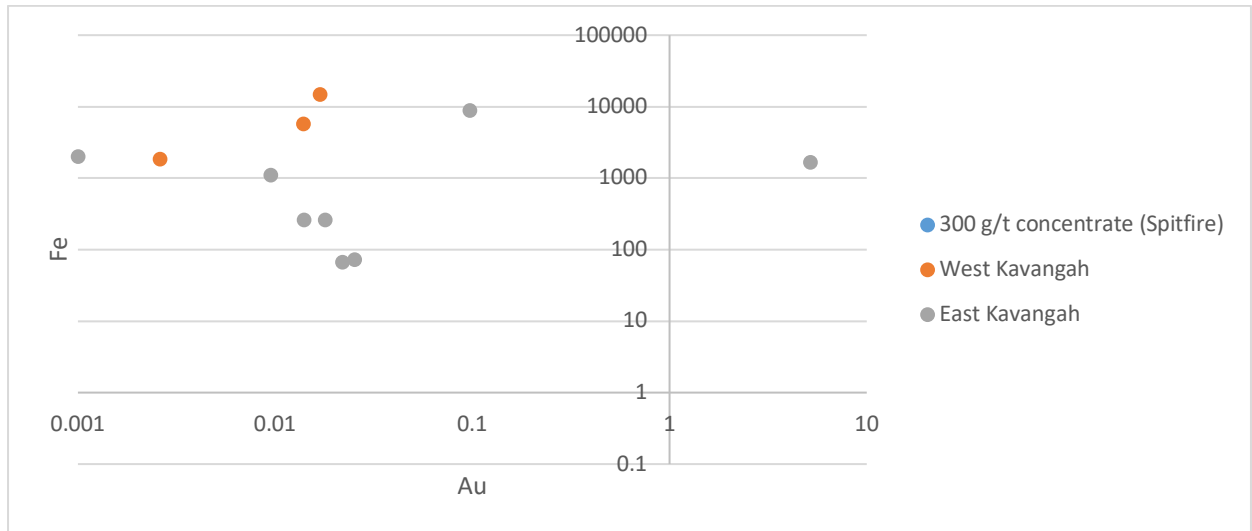


Figure 16 Fe:Au log log plot for Bi LA-ICP-MS

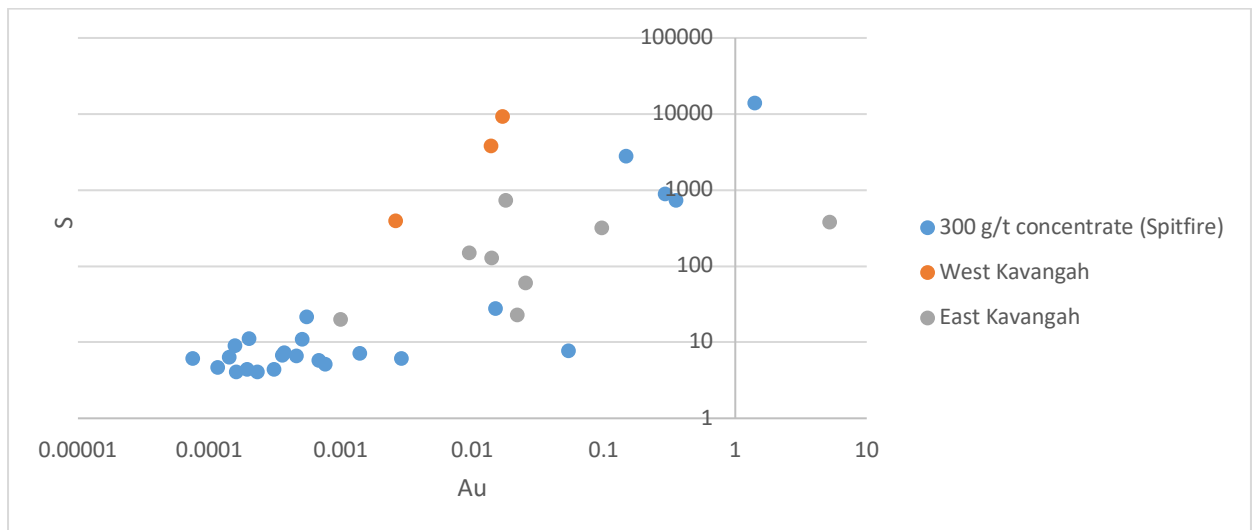
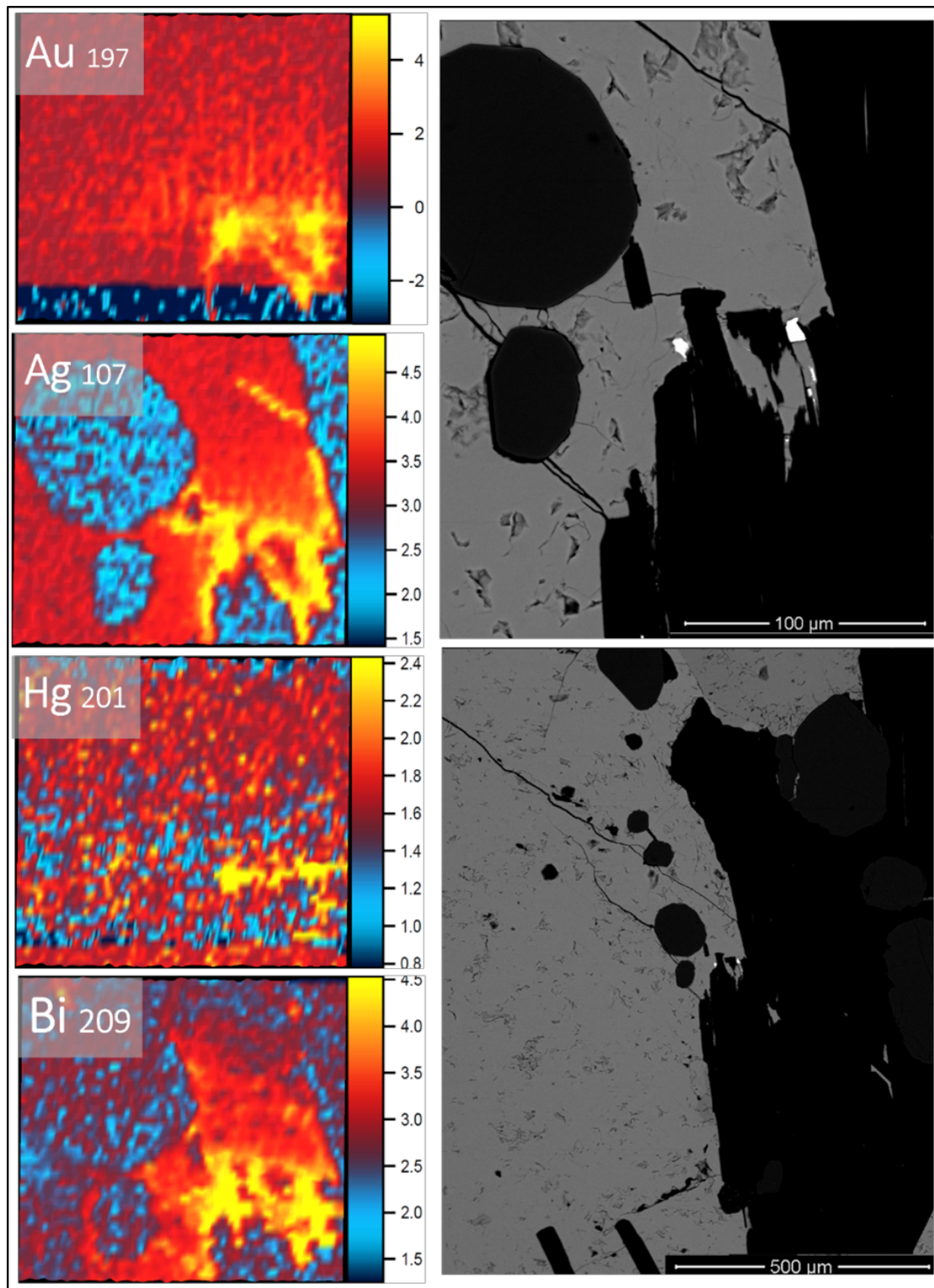


Figure 17 S:Au log log plot for Bi LA-ICP-MS

Appendix E5 – Raster map location



LA-ICP-MS mapping result for Au, Ag, Hg and Bi with a logarithmic scale, where yellow indicates higher relative concentrations (in counts per second)

Appendix F1 - Kanmantoo Assay data December 2014- July 2018

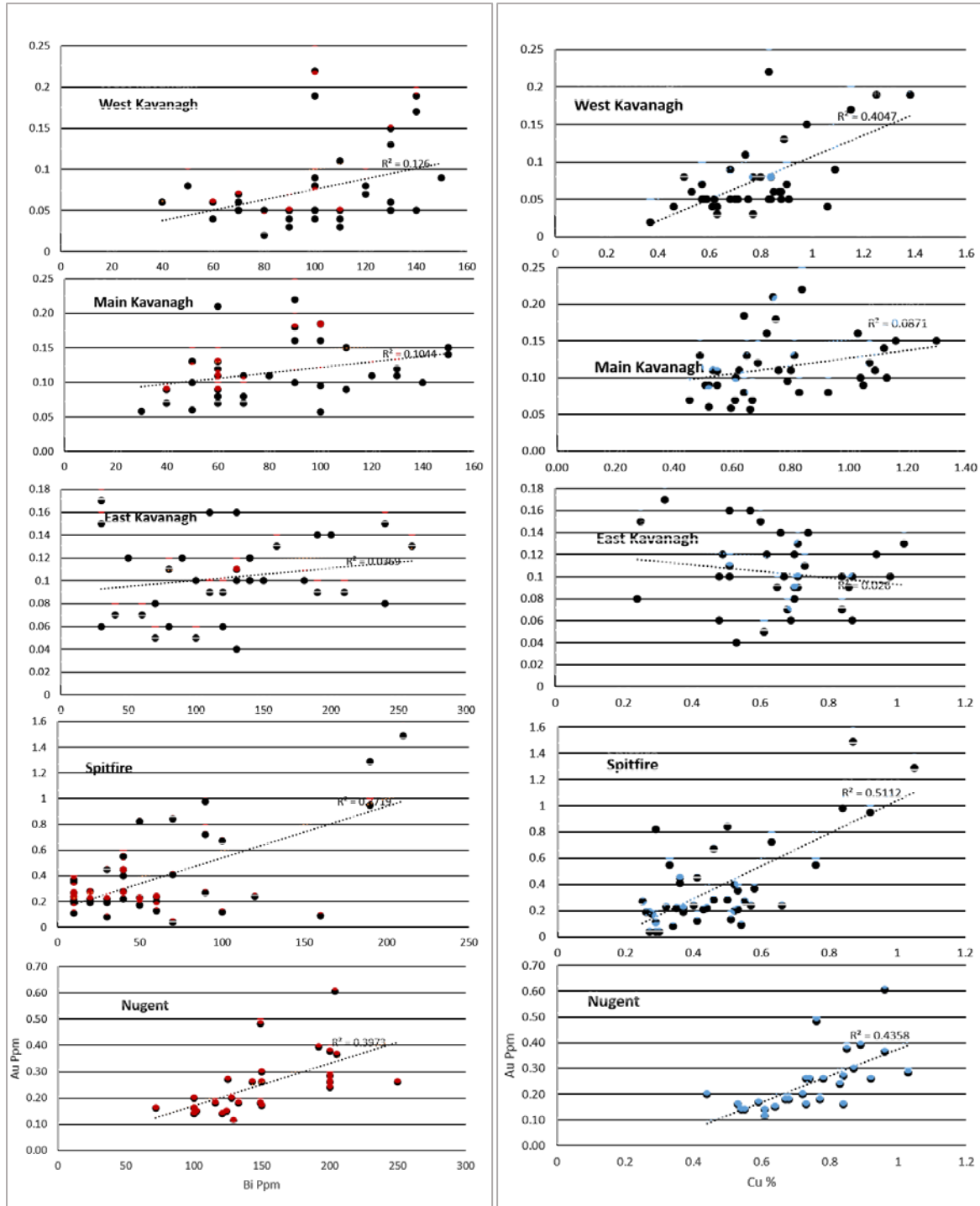


Figure 18 Mill data of average feed grade of 4500-5500 tonnes of ore for each mill processing shift

Appendix G1 – LA-ICP-MS Au

	Output_1_226	Output_1_227	Output_1_228	Output_1_229	Output_1_230	Output_1_231	Output_1_232	Output_1_233	Output_1_234	Output_1_235
Source file	TC300_gold1 - 1.d	TC300_gold1 - 2.d	TC300_gold1 - 3.d	TC300_gold1 - 4.d	TC300_gold1 - 5.d	TC300_gold1 - 6.d	TC300_gold1 - 7.d	TC300_gold1 - 8.d	TC300_gold1 - 9.d	TC300_gold1 - 10.d
DateTime	28/08/2018 (3) 07:09:13.00	28/08/2018 (3) 07:10:31.74	28/08/2018 (3) 07:11:54.60	28/08/2018 (3) 07:13:16.79	28/08/2018 (3) 07:14:43.35	28/08/2018 (3) 07:16:01.77	28/08/2018 (3) 07:17:25.30	28/08/2018 (3) 07:18:48.01	28/08/2018 (3) 07:20:15.15	28/08/2018 (3) 07:21:32.01
Date	28/08/2018 (3)	28/08/2018 (3)	28/08/2018 (3)	28/08/2018 (3)	28/08/2018 (3)	28/08/2018 (3)	28/08/2018 (3)	28/08/2018 (3)	28/08/2018 (3)	28/08/2018 (3)
Time	09:13.0	10:31.7	11:54.6	13:16.8	14:43.3	16:01.8	17:25.3	18:48.0	20:15.1	21:32.0
Duration(s)	24.052	19.201	19.644	25.405	24.962	23.632	25.848	24.075	23.189	24.962
Comments	TC300_gold1 - 1.d	TC300_gold1 - 2.d	TC300_gold1 - 3.d	TC300_gold1 - 4.d	TC300_gold1 - 5.d	TC300_gold1 - 6.d	TC300_gold1 - 7.d	TC300_gold1 - 8.d	TC300_gold1 - 9.d	TC300_gold1 - 10.d
Au197_CPS	4.96E+07	4.34E+07	4.33E+07	3.65E+07	3.61E+07	3.77E+07	3.59E+07	3.65E+07	3.83E+07	3.70E+07
Au197_CPS_Int2SE	3.60E+06	4.80E+06	5.30E+06	4.70E+06	4.10E+06	5.20E+06	4.90E+06	5.10E+06	5.50E+06	5.00E+06
Mg_ppm_m24	0.63	0	0.012	0.014	0.01	-0.004	-0.003	-0.017	0.41	0.003
Mg_ppm_m24_Int2SE	0.29	0.015	0.018	0.029	0.02	0.022	0.019	0.016	0.19	0.019
Al_ppm_m27	0.94	0.008	-0.011	0.002	0.016	-0.032	0.006	-0.033	0.65	0.042
Al_ppm_m27_Int2SE	0.21	0.036	0.031	0.026	0.036	0.045	0.039	0.023	0.33	0.035
Si29_CPS	1080	-20	230	90	-230	-100	180	60	210	-20
Si29_CPS_Int2SE	560	290	280	290	280	320	280	360	270	460
S_ppm_m34	158	51	90	28	48	12	42	88	83	38
S_ppm_m34_Int2SE	60	67	53	63	55	71	53	62	65	48
Ti_ppm_m49	0.098	0.079	0.041	0.065	0.126	0.066	0.02	0.048	0.132	0.061
Ti_ppm_m49_Int2SE	0.042	0.049	0.033	0.041	0.063	0.041	0.024	0.032	0.068	0.043
V51_CPS	41	11	16	26	18	15	-2.96941	17	25	12
V51_CPS_Int2SE	21	12	13	13	12	12	0.00017	12	14	10
Cr53_CPS	18	10	13	18	26	20	17	18	48	13
Cr53_CPS_Int2SE	14	14	15	14	15	15	13	14	27	13
Mn_ppm_m55	0.016	-0.013	0.022	0.004	-0.002	0.009	0.002	-0.008	0.003	-0.022
Mn_ppm_m55_Int2SE	0.02	0.03	0.022	0.026	0.022	0.026	0.024	0.031	0.023	0.022
Fe_ppm_m57	23.1	-0.52	0.09	0.28	0.06	-0.23	0.35	-0.11	1.1	-0.01
Fe_ppm_m57_Int2SE	6	0.37	0.47	0.63	0.65	0.59	0.65	0.75	1.1	0.42
Co_ppm_m59	0.0408	0.0021	-0.0008	0.0017	-0.0008	-0.0001	0.0034	0.0012	0.0001	0.0027
Co_ppm_m59_Int2SE	0.0086	0.0025	0.0013	0.0026	0.0014	0.0022	0.0027	0.0022	0.0016	0.0024
Ni_ppm_m60	0.02	0.01	-0.0047	0.004	-0.003	0.002	0.013	-0.0095	0.003	0.01

Ni_ppm_m60_Int2SE	0.013	0.011	0.0084	0.012	0.011	0.013	0.014	0.0093	0.012	0.015
Cu_ppm_m65	9.4	2.34	2.5	2.06	0.99	1.77	2.29	2.22	2.32	2.24
Cu_ppm_m65_Int2SE	1.6	0.2	0.28	0.22	0.27	0.24	0.27	0.25	0.26	0.21
Zn_ppm_m66	0.138	0.038	0.046	-0.01	-0.058	0.071	0.049	0.051	0.101	0.025
Zn_ppm_m66_Int2SE	0.056	0.069	0.071	0.078	0.073	0.083	0.069	0.073	0.097	0.068
As_ppm_m75	-0.011	0	0.001	0.013	0.023	0.027	-0.012	0.003	-0.011	0.006
As_ppm_m75_Int2SE	0.017	0.031	0.028	0.039	0.031	0.03	0.039	0.035	0.029	0.04
Se_ppm_m77	0.25	0.11	0.02	0.07	0.13	0.34	0.13	0.24	0.26	-0.04
Se_ppm_m77_Int2SE	0.18	0.21	0.21	0.27	0.18	0.22	0.23	0.27	0.21	0.19
Mo_ppm_m95	0.0005	0.002	0.0014	-3.2E-05	0.0006	-3.2E-05	0.0025	-3.2E-05	0.0011	0.0013
Mo_ppm_m95_Int2SE	0.0011	0.0023	0.0019	4.6E-06	0.0013	5.7E-06	0.003	5.3E-06	0.0016	0.0019
Ag_ppm_m107	5780	3610	3555	3879	4880	3808	3703	3752	3658	3808
Ag_ppm_m107_Int2SE	370	55	60	49	180	39	47	65	47	72
Ag_ppm_m109	5660	3593	3527	3862	4890	3794	3705	3704	3645	3823
Ag_ppm_m109_Int2SE	280	57	68	33	190	40	45	28	42	75
Cd_ppm_m111	0.0033	0.0059	-4.6E-05	-6E-05	-5.5E-05	0.0021	-6.2E-05	0.0052	0.0068	-0.00006
Cd_ppm_m111_Int2SE	0.0046	0.0067	6.1E-06	8.8E-06	7.3E-06	0.0044	0.000011	0.0075	0.0078	0.000012
Sn_ppm_m118	0.0099	-0.0027	0.0098	-0.0039	0.0007	0.0062	0.0097	0.0072	0.0068	0.0018
Sn_ppm_m118_Int2SE	0.0061	0.0048	0.0073	0.0069	0.0067	0.0093	0.0081	0.0066	0.0058	0.0064
Sb_ppm_m121	0.0065	0.0082	0.0052	0.0005	0.0028	0.004	-0.0014	-0.0005	0.001	-0.0034
Sb_ppm_m121_Int2SE	0.0053	0.0059	0.0064	0.0056	0.0067	0.0063	0.0057	0.0055	0.0075	0.0064
Te_ppm_m125	0.044	0.014	0.047	0.062	0.048	0.001	0.056	0.025	0.017	0.044
Te_ppm_m125_Int2SE	0.033	0.019	0.038	0.036	0.035	0.014	0.04	0.026	0.024	0.045
Hf_ppm_m178	-1.34E-07	-1.50E-07	-1.49E-07	-2.01E-07	-1.74E-07	0.0008	0.00027	-1.88E-07	-1.76E-07	-2.09E-07
Hf_ppm_m178_Int2SE	1.50E-08	1.80E-08	1.90E-08	3.00E-08	1.90E-08	0.0011	0.00054	2.70E-08	2.70E-08	3.90E-08
Ta_ppm_m181	-1.93E-07	-2.17E-07	-2.35E-07	-2.88E-07	-2.72E-07	-3.00E-07	-3.22E-07	-3.10E-07	-2.63E-07	0.00036
Ta_ppm_m181_Int2SE	2.20E-08	2.50E-08	3.20E-08	4.30E-08	3.50E-08	5.30E-08	5.40E-08	5.10E-08	4.00E-08	0.00035
W_ppm_m182	0.00024	-5.7E-06	-5.6E-06	0.00063	0.00046	0.0019	0.00019	0.00036	-7E-06	0.00063

W_ppm_m182_Int2SE	0.00049	6.4E-07	8.2E-07	0.00073	0.00093	0.0017	0.0004	0.00074	1.3E-06	0.00072
Hg201_CPS	1.14E+04	14440	14630	14230	1.80E+04	14160	14670	14070	15040	13950
Hg201_CPS_Int2SE	1.00E+03	510	540	720	1.00E+03	760	710	550	790	740
Tl_ppm_m205	0	0.0018	0.0014	0.0017	0.0017	-0.0003	0.0007	-0.0016	-0.0012	-0.0001
Tl_ppm_m205_Int2SE	0.0011	0.0013	0.0015	0.0017	0.0018	0.0013	0.0016	0.0014	0.0011	0.0011
Pb_ppm_m208	0.23	0.0018	-0.0005	-0.0011	-0.0012	0.0016	0.002	0.0023	0.0079	0.0028
Pb_ppm_m208_Int2SE	0.038	0.0021	0.0015	0.0016	0.0013	0.0019	0.002	0.0022	0.0041	0.0021
Bi_ppm_m209	1.18	0.0073	0.0059	0.0037	0.094	0.014	0.0207	0.023	0.0261	-0.0052
Bi_ppm_m209_Int2SE	0.17	0.002	0.0022	0.0019	0.024	0.0039	0.0034	0.0052	0.0067	0.004
Th_ppm_m232	0.000045	0.00031	0.000045	0.00006	-1.6E-06	0.0001	0.00023	-1.7E-06	0.0001	0.00005
Th_ppm_m232_Int2SE	0.000092	0.00035	0.000092	0.00012	2.1E-07	0.00014	0.00024	2.9E-07	0.00014	0.00011
ExtraMetadata	FILENAME: TC300_gold1 - 1.csv	FILENAME: TC300_gold1 - 2.csv	FILENAME: TC300_gold1 - 3.csv	FILENAME: TC300_gold1 - 4.csv	FILENAME: TC300_gold1 - 5.csv	FILENAME: TC300_gold1 - 6.csv	FILENAME: TC300_gold1 - 7.csv	FILENAME: TC300_gold1 - 8.csv	FILENAME: TC300_gold1 - 9.csv	FILENAME: TC300_gold1 - 10.csv
Au197_CPS_LOD	0	0	0	0	0	0	0	0	0	0
Mg_ppm_m24_LOD	0.028541	0.032329	0.031042	0.036267	0.044505	0.035396	0.078945	0.041484	0.040073	0.032081
Al_ppm_m27_LOD	0.13802	0.057578	0.063908	0.31647	0.065619	0.060323	0.061842	0.059938	0.058851	0.062607
Si29_CPS_LOD	0	0	0	0	0	0	0	0	0	0
S_ppm_m34_LOD	53.449	94.494	65.173	66.294	82.91	67.898	63.291	84.435	59.028	72.492
Ti_ppm_m49_LOD	0.083341	0.085384	0.18825	0.095902	0.087028	0.10879	0.10528	0.10233	0.063813	0.066056
V51_CPS_LOD	0	0	0	0	0	0	0	0	0	0
Cr53_CPS_LOD	0	0	0	0	0	0	0	0	0	0
Mn_ppm_m55_LOD	0.041243	0.045971	0.040556	0.034644	0.051689	0.047616	0.052658	0.048302	0.054382	0.047517
Fe_ppm_m57_LOD	0.78453	11.892	1.0213	0.80267	1.1464	0.98522	0.91882	0.87574	0.89918	0.91462
Co_ppm_m59_LOD	0.004467	0.004426	0.003167	0.003059	0.003911	0.003362	0.003567	0.00425	0.004051	0.003221
Ni_ppm_m60_LOD	0.016747	0.022935	0.022585	0.021566	0.023611	0.023736	0.021813	0.026139	0.021158	0.021272
Cu_ppm_m65_LOD	12.599	0.17436	1.4698	3.9455	2.5764	0.15639	0.23748	0.1642	0.17133	0.18491
Zn_ppm_m66_LOD	0.088211	0.098883	0.095933	0.1281	0.12022	0.13058	0.14465	0.12304	0.11954	0.15927
As_ppm_m75_LOD	0.055185	0.059996	0.057429	0.078054	0.069439	0.076358	0.073448	0.073155	0.071706	0.064525

Se_ppm_m77_LOD	0.26043	0.40327	0.35299	0.36826	0.43392	0.36438	0.34535	0.32799	0.34322	0.35125
Mo_ppm_m95_LOD	0.006635	0.004073	0.005601	0.014685	0.007091	0.004408	0.005578	0.006258	0.006425	0.007521
Ag_ppm_m107_LOD	0.022764	0.031714	0.19371	0.25236	0.036093	0.080676	0.03279	0.030381	0.216	0.034289
Ag_ppm_m109_LOD	0.025993	0.028839	0.02429	0.034645	0.030124	0.042514	0.03033	0.5485	0.28993	0.077214
Cd_ppm_m111_LOD	0.017484	0	0.026698	0.015588	0.018368	0.028025	0.018229	0.019767	0.021223	0.022897
Sn_ppm_m118_LOD	0.027438	0.011364	0.009495	0.012105	0.014403	0.017781	0.016763	0.010534	0.011845	0.011065
Sb_ppm_m121_LOD	0.009014	0.010824	0.011356	0.014141	0.012193	0.013258	0.011016	0.00902	0.011739	0.011895
Te_ppm_m125_LOD	0.074036	0.084571	0.063331	0.07314	0.075547	0.076185	0.079491	0.068796	0.081498	0.10075
Hf_ppm_m178_LOD	0.001356	0	0	0	0.002564	0.001745	0.003637	0.001783	0.002316	0.0025
Ta_ppm_m181_LOD	0.000648	0.001192	0.00055	0	0.000881	0.0006	0.000626	0.001044	0	0
W_ppm_m182_LOD	0.00147	0.001257	0.002908	0.002685	0.002774	0.002316	0	0.002714	0.001817	0.00238
Hg201_CPS_LOD	0	0	0	0	0	0	0	0	0	0
Tl_ppm_m205_LOD	0.002677	0.00213	0.002452	0.002477	0.003017	0.002187	0.002563	0.003153	0.002106	0.002656
Pb_ppm_m208_LOD	0.003249	0.003222	0.002648	0.00424	0.003855	0.003137	0.003582	0.003527	0.003495	0.004604
Bi_ppm_m209_LOD	0.00204	0.001825	0.001957	0.001603	0.002168	0.001955	0.001954	0.001552	0.001795	0.001527
Th_ppm_m232_LOD	0.000282	0.000338	0.00024	0.000516	0.000591	0.001353	0.000384	0.000579	0.000645	0.000651